UNIVERSITY OF OSLO
Department of Physics
Centre for Physics of Geological Processes

Thesis for the degree Master of Science:

Mineral reactions and structural evolution of deformation zones transecting the layered sequence of the Leka Ophiolite Complex (LOC)

Kerstin Drivdal

June 14, 2013

This page intentionally left blank

Takkeord

Flere personer har hjulpet til underveis i arbeidet med denne masteroppgaven. Først og fremst min veileder Håkon O. Austrheim som fikk meg gjennom dette. Hans entusiasme for fagfeltet, tålmodighet og kontinuerlige støtte har vært avgjørende. Takk, Håkon!

Jeg er også takknemlig for den rettledningen jeg har fått av min med-veileder Torgeir B. Andersen, som satte meg i gang med kartlegging av forkastninger i felt og ga verdifulle kommentarer i sluttfasen av prosjektet.

Jeg vil også takke følgene personer:

- Milena Farajewicz, Krakow, for hjelp og selskap i sagerommet sommer 2011.
- PhD studentene Kjetil Thøgersen og Jørgen Trømborg, PGP, for å være gode rollemodeller og for å ha latt meg bruke MATlab programmet sitt for plotting av klinopyroksen.
- Muriel Erambert, Geologisk Institutt, UiO, for opplæring på micro proben og for hjelp med micro probe analyser.
- Salah Akhavan, Geologisk Institutt, UiO, for å ha laget flotte tynnslip til meg og for sent i prosjektet, ha ordnet 5 ekstra tynnslip raskt.
- Berit Østeby for å ha lest gjennom deler av manuskriptet og gitt kommentarer på det språklige.
- Min bror Arild for å ha lest gjennom deler av manuskriptet og gitt kommentarer på det språklige.

Sist, men ikke minst, vil jeg takke master studentene på PGP: Céline, Derya, Hedda, Håvard, Kristin, Liene og Petter for deres generøsitet.

Tusen takk!

Kerstin Drivdal

Abstract

Serpentinization and chemical alteration of the oceanic lithosphere are fundamental to understanding processes observed at Mid-oceanic ridges. The process that alters the oceanic lithosphere can be studied in exposed ophiolite complexes. The Leka Ophiolite Complex (LOC), Nord-Trøndelag, is considered to be a part of the Uppermost Allochthon that was thrusted up on Baltica during the Caledonian Orogeny. This makes the LOC, which is a unique cross-section through the oceanic crust and underlying mantle, an excellent place to study the coupling between deformation, hydration and transport of elements, reflected in changes in mineralogy and textures. Detailed mapping and petrography of an area in the layered sequence south of the Kvaløya farm, west-side of Leka, has been undertaken and revealed a primary structure defined by alternating layers of dunite with thin chromite layers, clinopyroxenites, chromite-rich clinopyroxenites and wehrlite. A NE-SW trending penetrative foliation is defined by serpentine veins and serpentine filled anastomosing microshear zones. The area is transected by a dense set of NE-SW to EW deformation zones, some with a dextral movement of several meters. The NE-SW to EW trending deformation zones include breccias and shear zones with elongated lenses representing ductily deformed fragments from the brecciation process. These deformation zones function as conduits for fluids and facilitate transport of mobilized elements. Ca derived from serpentinization of primary clinopyroxene is transported along such deformation zones and result in formation of secondary diopsidic pyroxene in bands parallel to the deformation zones. A range of complex structures and textures formed during interaction between deformation and reactions is described from these deformation zones and their closest wall rock. These involve replacement of the primary minerals with secondary minerals as follows: Olivine $\rightarrow$ Clinopyroxene, Orthopyroxene(?) $\rightarrow$ Clinopyroxene + Olivine, Chromite $\rightarrow$ Chlorite, Clinopyroxene $\rightarrow$ Serpentine. Serpentine filled extensional veins with fibrous growth of olivine suggest that olivine like clinopyroxene was both consumed and formed during the alteration. The composition of olivine range from Fo94 in the dunite to Fo85 in the clinopyroxenite. A slight increase in Fo content of secondary olivine (Fo93-94) compared to primary olivine (Fo92-93) is measured in the dunite. Both primary and secondary clinopyroxene are diopsidic with cpx1 containing a higher content of Al_2O_3 (up to 2.6 wt%). It is suggested that the described deformation and hydration occurred when the LOC was still part of the oceanic lithosphere.

Contents

Chapter 1

Introduction

1.1 Preface

The work presented in this thesis was performed at the Center for Geological Processes Physics (PGP), Department of Physics, University of Oslo, during the period between July 2012 and May 2013.

The work included a field excursion to Leka, Nord-Trøndelag, in summer of 2011 and two weeks of field work during the summer of 2012. The excursion of 2011 was led by Prof. Håkon Austrheim. Two of the days during fieldwork in 2012 were under the guidance of Prof. Torgeir B. Andersen and Prof. Håkon Austrheim.

This study investigates a part of the layered cumulate section of the Leka Ophiolite Complex (LOC), situated in the Steinstind block south of Kvaløya Farms (Figure 2.1). The main focus is on the role of serpentinization and the feedback between serpentinization and deformation including transport of elements in fluids.

This thesis starts with the listing of some important aspects of serpentinization and continues with an introduction to the ophiolite concept. Within this context the regional geology is outlined and some previous work at Leka is presented.

Field and petrographical observations will be described and discussed in light of relevant previous work. Mineralogical relationships are integrated with micro- and macrostructural observations by use of optical microscopy and electron microprobe analysis (EMPA).

1.2 Background - The Importance of Serpentinization

More than 3% of the Earth's surface is assumed to consist of serpentinite and serpentinized peridotite (Guillot and Hattori, 2013). The extent of serpentinization and the role it plays on several arenas make serpentinization of oceanic lithosphere one of the most important geological process.

Some of these important aspects regarding serpentinization (and deserpentinization) are listed below:

Seismicity
Serpentine is a mechanically weak mineral that lubricates converging plates at plate boundaries during aseismic creep (Guillot and Hattori, 2013). Thus rheological changes due to dehydration of serpentine might have implications for seismicity of subducting slabs, e.g. , by localization of strain (Hirth and Guillot, 2013). The same authors suggest that earthquakes may nucleate via thermally induced viscous flow instabilities, and that the mentioned strain localization may provide the required initial strain localization for nucleation of earthquakes.

The geochemical cyclus
Decciacation of the fluid as hydration proceed results in a fluid enriched in mobile elements that eventually are incorporated in the crystal structure of serpentine. Serpentinites formed in different tectonic environment will incorporate various fluid-mobile elements distinctive to that particular environment. Sea water is transported from the hydrosphere through hydrogeological circulation at the ocean floor proximal to spreading centers and further to subduction zones. Expulsion of pore fluid from sediments in subduction zones may induce partial melting in the overlying mantle-wedge and incorporate fluid-mobile elements into the mantle (Evans et al., 2013; Guillot and Hattori, 2013).

Ore deposits on shore (e.g. Nickel)
Serpentinized and partly weathered harzburgitic ophiolites give rise to the worlds largest Ni-deposits. (Butt and Cluzel, 2013).

CO_2 Sequestration
Industrial mineral carbonation may be illustrated by the reaction of olivine or serpentine with CO_2 to form magnesite + quartz $\pm H_2O$. Similar carbonation reactions occur naturally during serpentinization, hydrothermal alteration and weathering of serpentinite. An estimated 300 million tonnes of CO_2 are globally sequestered by continental weathering each year ((Power et al., 2013) and references therein).

Geophysical properties
Serpentinization of mantle rocks reduces rock density from $\sim 3.3 g/cm^3$ to $\sim 2.7 g/cm^3$ which may lead to a volume increase of 20-40%. The degree of magnetization increases, while seismic velocities and gravitational signatures are reduced. Another result is an elevated topography as the rocks become lighter. Mechanically the volume increase leads to fracturing that opens new volumes of the rock to fluids and hydration(several authors,e.g. ,Früh-Green (2005); Iyer et al. (2008b); Jamtveit et al. (2009); O'Hanley (1992))

Origin of life
The serpentinization of olivine and pyroxene may be described by the general reaction

olivine + pyroxene + H_2O $\longrightarrow$ serpentine±brucite±magnetite + H_2 (McCollom and Seewald, 2013).
Formation of magnetite leads to a reducing environment (ferrous iron, Fe^{2+}, in olivine forms ferric iron, Fe^{3+}, in magnetite) as well as hydrogen gas (H_2), and provides a basis for the production of methane (CH_4) and hydrogen sulphide (H_2S). Such gases are discharged from deep-sea hydrothermal systems through sea floor vents and are important sources of energy for microbial communities (Bach and Früh-Green, 2010; Früh-Green, 2005; Früh-Green et al., 2004).

1.3 The Ophiolite Concept

Introduction

The term *"ophiolites"* was first used by the French mineralogist Alexandre Brongniart about serpentinite mélanges. He later incorporated ultramafic rocks, gabbro, diabase, and volcanic rocks (Dilek and Furnes, 2011).

Steinmann (1927) recognized a relationship between the suite of peridotite (serpentinite), gabbro and diabase spilite, and the occurrence of deep sea sediments. He interpreted the suite to have formed at the ocean floor as a consequence of magmatic differentiation. He observed that the gabbro and diabase intruded the serpentine peridotite, which would imply that these rocks had to be younger than the peridotite (Dilek, 2003; Dilek and Furnes, 2011). Steinmann's discovery was in conflict with the later " layer-cake" Penrose-type ophiolite definition, which promoted the view of the oceanic crust as a uniform unit. However, Steinmann's observation has been supported by recent studies of, e.g. , Ligurian ophiolites (Dilek, 2003).

From the early 70's to mid 80's researchers realized that ophiolites were widely different in terms of petrochemical characteristics and tectonic evolution. Geochemical studies have provided the basis for reconsidering earlier conceptions of ophiolites. An increasing number of ophiolites are traced back to a magmatic origin associated with subduction zones (Dilek and Furnes, 2009). The Penrose model is still regarded to be applicable for crust formation at fast-spreading ridges (Bach and Früh-Green, 2010).

Definition of Ophiolites

The earliest seismic surveys supported a uniform interpretation of the oceanic crustal structure, with few lateral variations. Combined with studies of, e.g. , the Troodos ophiolite (Cyprus) and the Semail Ophiolite (Oman), the theory of the oceanic crust as a "layer-cake" structure (Figure 1.2) was supported, and, again, provided the basis for the Penrose ophiolite definition in 1972 (Dilek, 2003) .

The Penrose definition did not contain any statements about the emplacement mechanisms nor did it define ophiolites based upon their tectonic setting at formation. This led to a long lasting debate that divided geoscientists into those who supported an "arc" model and those who supported a "ridge" model, (Dilek, 2003).

Systematic petrologic and geochemical investigations of ophiolites around the world in the '80's and '90's demonstrated the vital significance of subduction derived fluids, as well as the melting history, for the development of ophiolitic magmas. The most widely accepted tectonic setting for formation of ophiolites was forearc, arc and backarc embryonic settings in supra-subduction zones (Dilek and Furnes, 2011).

Dilek and Furnes (2011) define an ophiolite

> *as an allochthonous fragment of upper mantle and oceanic crustal rocks that is tectonically displaced from its primary igneous origin of formation as a result of plate convergence.*

A column of such an ophiolite, should contain from bottom to top: peridotites, ultramafic to felsic crustal intrusions and volcanic rocks, that can be geochronologically and petrochemically genetically related. Some of these units may be missing in incomplete ophiolites (Dilek and Furnes, 2011).

Dilek and Furnes (2011) and references therein divide ophiolites into two major units, *subduction unrelated ocean crust* which include Continental Margin(CM) Ophiolites, Mid-Ocean Ridge(MOR) and Plume-type(P), and *subduction related ocean crust*, which include Suprasubduction-Zone(SSZ) Ophiolites and Volcanic-Arc(VA) Ophiolites.

The LOC is regarded as a SSZ-type. A short description of a SSZ-ophiolite is given below.

The *Suprasubduction-Zone Ophiolite*, (SSZ type), is formed when an initial subduction is followed by a fast slab-rollback resulting in extension and seafloor spreading. In the beginning of the subduction phase, magma is first produced as a result of decompression melting of deep and fertile lherzolitic mantle, which provides the early crust units with MORB-like compositions. Initially fluids containing components derived from the subducting slab, have little impact on the melting trend. As the process continues, the melting phases are all the more impacted by both slab dehydration and related mantle metasomatism. Repeated melting of the hydrated mantle leaves a greatly depleted, olivine and orthopyroxene rich source behind. Such melting columns produce island-arc tholeiite magma forming lavas that overlie the early crustal units. Accordingly, SSZ ophiolites will show a characteristic, sequential progression from MORB to island-arc tholeiite to boninitic igneous activity (Dilek and Furnes, 2011).

The Complete Ophiolite Suite

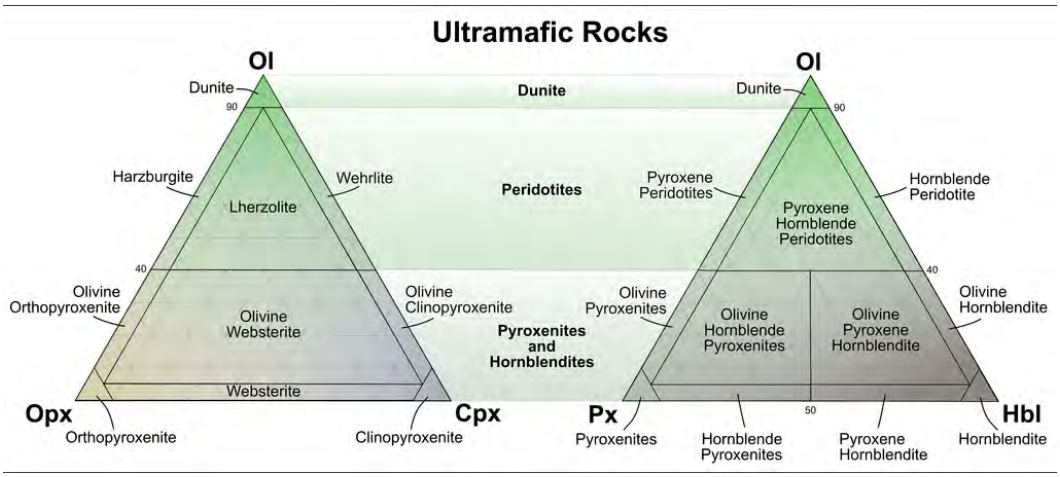

Figure 1.1: IUGS classification of Ultramafic Rocks. The nomenclature for coarse-grained ultramafic rocks is based on the modal (i.e. volume %) proportions of olivine, clinopyroxene and orthopyroxene present. Figure collected from *http://www.mindat.org/photo-471844.html* (mineral and locality database Mindat.org, 2013).

Figure 1.1 displays the IUGS classification of ultramafic rocks, which is divided into peridotites and pyroxenites. The classification is based on the dominant mineralogy, i.e. olivine, orthopyroxene or clinopyroxene. Subordinate minerals like plagioclase and

oxides (magnetite, ilmenite, and chrome spinel) may be present. Primary minerals can be replaced by hornblende and serpentine during hydration events (Winter, 2009). Not all ophiolites contain all sequences in the idealized ophiolite suite, as explained previously in subsection 1.3. A complete ophiolite pseudosection can be described as follows below:

The harzburgites make up the lowermost part of the pseudosection (Figure 1.2). These formed at the bottom of magma chambers beneath mid-ocean ridges or in back-arc basins above subduction zones. They are intruded by sheets of gabbros and dunites. Such intrusions are believed to be remains of a magma feeding system (Gill, 2010), that got clogged by crystallizing magma as the oceanic crust and upper mantle moved away from the spreading center.

The mantle harzburgite is overlain by layered crustal cumulates dominated by dunites with chromitite bands and pods. This section forms the base of the oceanic crust. The dunites are intruded by gabbro sills and interstitial plagioclase and clinopyroxene that percolate through the dunite. The dunites are overlain by layered gabbros intruded by sheets of wehrlite (Gill, 2010).

The sheeted dike complex above the gabbros is a relic of the magma plumbing system that fed the pillow basalts erupting on the ocean floor. On top of the magmatic ophiolite suite is an association of sediments.

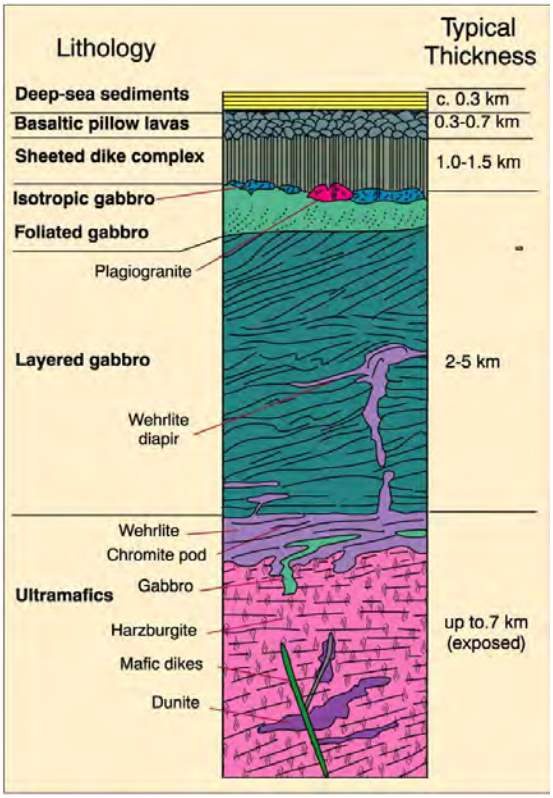

Figure 1.2: Ideal ophiolite pseudosection as defined by "the Penrose ophiolite model". This figure is based on the Semail ophiolite in Oman after Boudier and Nicolas (1985) and taken from *Principles of Igneous and Metamorphic Petrology* by (Winter, 2009).

1.4 Regional Geology of North-central Norway

1.4.1 Tectonostratigraphy

The Scandinavian Caledonides extend roughly 1800 km southwards from ca.71°N to 59°N latitude and are up to ca. 300 km wide (Roberts and Gee, 1985). The closure of the Iapetus Ocean, which terminated in late Middle Silurian (∼430 Ma), was followed by a continent-continent collision between Laurentia and Baltica, leading to the formation of the Scandinavian Caledonides. During the Iapetus closure and the continent-continent collision a variety of nappes were thrusted southeastwards and stacked upon the Precambrian crystalline basement of Baltica and its sedimentary cover. The Vendian (Ediacaran) to early Ordovician sediments acted as a décollement surface, allowing the thrust sheets to propagate into the foreland SE of Oslo.

Age and provenance studies have assigned different affinities and thus different structural settings to the various nappes and rock units. Roberts and Gee (1985) divided the nappes and rock units into four allochthons. The techtonostratigraphic subunits of the different allochthons vary depending on geographical location, while the division into allochthons relies on lithological, magmatic and geochemical criteria.

The summary below is based on Roberts (2003); Roberts and Gee (1985); Stephens et al. (1985) and Roberts et al. (2007). The allochthons are, in the structurally highest and most traveled descending order:

- The Lower Allochthon - contains platform and shelf successions indigenous to the Baltoscandian passive continental margin.
- The Middle Allochthon - contains continental rise accumulations, which in most traditional models are thought to be indigenous to the Baltoscandian passive continental margin.
- The Upper Allochthon - the lower levels contains continental rise accumulations interpreted to have formed in the continent-ocean transition (COT) zone of Baltica, while the upper levels contain suspect terranes, including ophiolites formed in the ancient, exotic Iapetus Ocean. The upper levels show indication of a Laurentian affinity.
- The Uppermost Allochthon - contains carbonate shelf, slope/rise accumulations interpreted to have formed in a continental margin setting, and evolved arc assemblages. The units are of Laurentian affinity or derived from unknown microcontinents.

The Leka ophiolite is commonly assigned to the Uppermost Allochthon. The Uppermost Allochthon extends almost continuously over more than 700 km covering large parts of north-central Norway (Roberts et al., 2007). It comprises two nappe complexes with the Helgeland Nappe Complex overlying the structurally lower Rödingsfjället Nappe Complex (Barnes et al., 2007) (Figure 1.4). The Uppermost Allochthon has been placed outboard of the pre-orogen margin of Baltica by several authors, e.g. , Roberts and Gee (1985); Stephens et al. (1985). They thus ascribe the Uppermost Allochthon to a Laurentian origin (Roberts and Gee, 1985; Roberts et al., 2007; Stephens et al., 1985).

Yoshinobu et al. (2002), hypothesized that the nappes in the Helgeland Nappe Complex

consist of continental fragments and arc sequences originally formed outboard of Laurentia. These segments were amalgamated during collision with Laurentia. Accordingly, the Leka ophiolite was formed above the Ordovician east-dipping subduction zone and were, together with the composite nappes in the Helgeland Nappe Complex, imbricated on to the Laurentian continent (Figure 1.3). After collision, the subducting slab changed polarity and the Helgeland Nappe Complex including the Leka ophiolite was finally emplaced upon the Baltoscandian platform where it remained after the subsequent Pangean breakup.

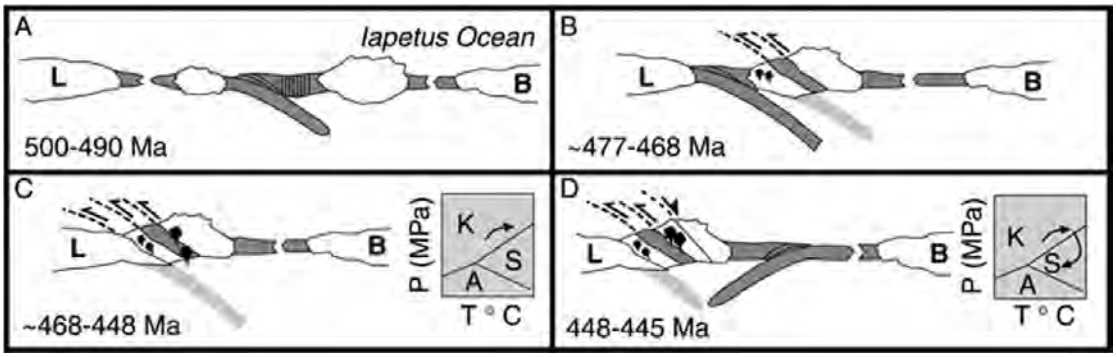

Figure 1.3: The schematic illustration shows a proposed Ordovician evolution of the Helgeland nappe complex within the Uppermost Allochthon. **(A)**: Continental slivers proximal to Laurentia (L) and formation of the SSZ Leka ophiolite above east-dipping subducting slab. **(B)**: Collision of continental fragments and preservation of ophiolites. **(C)**: Continued amalgamation of Uppermost Allochthon with Laurentia and loading of lower nappes prior to 448 Ma during Taconic orogenesis. **(D)**: Exhumation of Helgeland nappe complex ca. 447 Ma, followed closely by initiation of west-dipping subduction and eventual closure of Iapetus during Scandian phase of Caledonide orogeny. B = Baltica. Text and figure modified from Yoshinobu et al. (2002) .

Five nappes have been identified in the Helgeland Nappe Complex. These are in structurally descending order; Upper Nappe, Middle Nappe, Lower Nappe, the Sauren-Torghatten Nappe and the Horta Nappe (Barnes et al., 2007; Roberts et al., 2007) (Figure 1.4a). Barnes et al. (2007) indicate that two additional rock units, the Leka ophiolite and the Horta archipelago with the Hortavær igneous complex, may be possible separate nappe units that can be assigned to the Helgeland Nappe Complex. Structurally Barnes et al. (2007), place the Leka ophiolitic basement between the Sauren-Torghatten Nappe and the suggested Horta Nappe.

The overlaying sedimentary units of the Leka Ophiolite Complex, the Skei Group, are interpreted to have been unconformably deposited during the Ordovician in a continental fluvial to shallow-marine environment (Sturt et al., 1985). Dating of zircons in metasandstones of the Skei Group yields Proterozoic and Archean ages. Comparable zircons from metasandstones of the Lower Nappe suggest that metasandstones from the Skei Group derived from uncovered parts of Lower Nappe rocks (Barnes et al., 2007). This indicates active tectonism at the time of deposition and that the structurally higher unit (the Leka ophiolite) at the time of deposition, was located topographically lower than the structurally lower Lower Nappe (Barnes et al., 2007; Sturt et al., 1985). The Skei Group is structurally assigned to the Sauren-Torghatten Nappe (Barnes et al., 2007) (Figure 1.4).

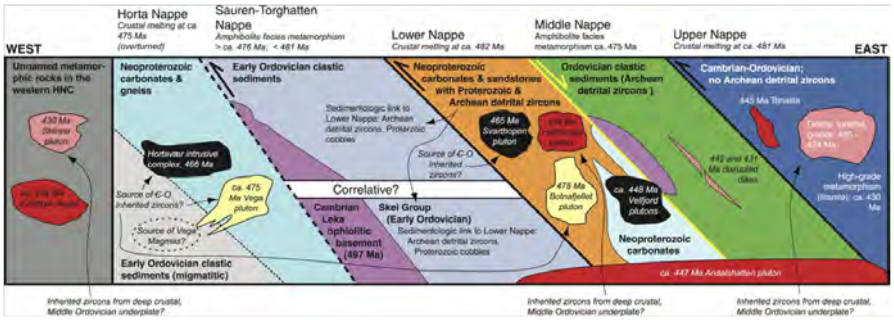

(a)

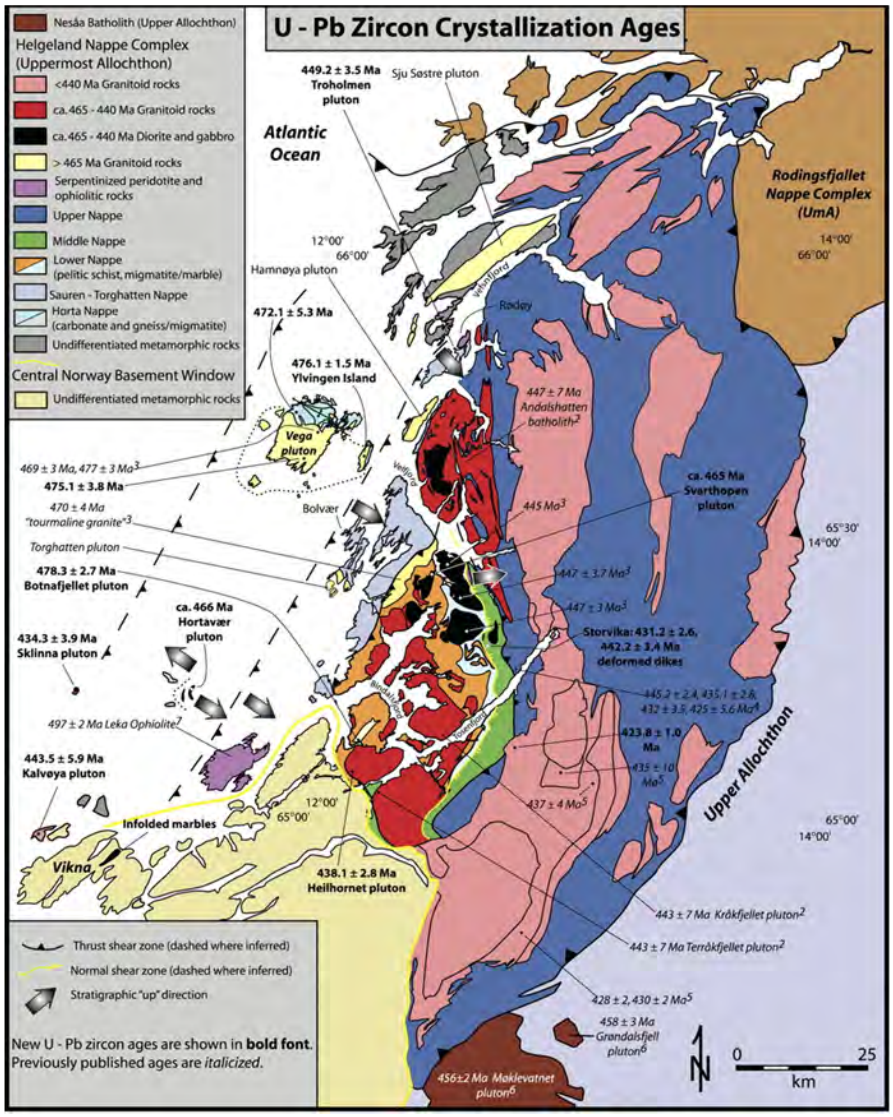

(b)

Figure 1.4: (1.4a): Schematic cross section of the Helgeland Nappe Complex nappes and plutons at the beginning of Scandian thrusting (ca. 430 Ma). Colors correspond to lithologies illustrated in the regional geological map below. (1.4b): Regional geological map showing the position of the Helgeland Nappe Complex in north-Central Norway. Figures from Barnes et al. (2007).

1.4.2 General Geology of Leka

It was Prestvik, 1974, who first recognized the rock association at Leka as an ophiolite suite (Furnes et al., 1988). Since then most of the work at the Leka Ophiolite Complex (LOC), with a few exceptions, has focused on tectonic and magmatic relationships. This work has resulted in a relatively good overview of a plausible formation and emplacement history.

The LOC is well exposed and restricted to the islands of Leka, Madsøya and some of the surrounding islets. The structural and stratigraphic relationship to the mainland rocks is inferred to be tectonic (Furnes et al., 1988; Titus et al., 2002).

Titus et al. (2002) interpret the LOC to be a down-faulted block that was preserved in a pull-apart structure related to activation of an orogen-parallel strike-slip system during postorogenic extension. At a number of islets (Solsemøyene) south-west of Leka, a tectonic contact between sheared serpentinite of the LOC and the underlying Solsemøyene Group metasediments (deposition $>$ 526 Ma) has been observed (Furnes et al., 1988). Additionally, gravity modeling of the LOC indicates that the complex is bounded by steep walls that extend to a depth of $\sim$7 km (Titus et al., 2002).

Two fault sets, a larger NE-SW trending fault set and a smaller, discontinuous NW-SE trending fault set, were identified by Titus et al. (2002). Evidence suggested that the larger NE-SW oriented fault set, which also comprises the bounding faults, is tensional faults with a sinistral movement. An additional N-S to NNW-SSE compressional component was identified at some of the NE-SW trending faults (Titus et al., 2002).

The LOC fits well with the idealized ophiolite section. A thorough pseudostratigraphy was described by Furnes et al. (1988); the LOC represent a unique cross-section through the oceanic crust and underlying mantle. From bottom to top, a harzburgite complex with minor dunite and lherzolite make up the 500 m - 1,5 km lowermost part of the ophiolitic column. This unit is overlain by ultramafic cumulates, which transcend into gabbroic cumulates overlain by vari-textured meta gabbros. Dike swarms and pillow lavas constitute the upper part of the pseudosection.

Dating by Dunning and Pedersen (1988), was done by single zircon U/Pb geochronology and yielded a the magmatic age of the mafic and ultramafic units of the LOC of 497$\pm$2 Ma. Rocks associated with the LOC also showed a supra-subduction zone geochemical affinity.

A possible development history of the LOC was deduced from geochemical data showing transitions from MORB to island arc tholeiites (IAT) affinities. Thus Furnes et al. (1988) concluded that the LOC was formed over a subduction zone in a back-arc basin, which classifies the LOC a SSZ-type ophiolite.

1.5 Previous Work

Reaction-assisted fracturing during serpentinization and some geochemical consequences of serpentinization

In two subsequent studies of ultramafic rocks at Leka, Iyer et al, 2008a, 2008b, looked into the reaction-assisted, self-reinforcing process of hierarchical fracturing during serpentinization (Iyer et al., 2008b), and some geochemical consequences of serpentinization of oceanic lithosphere (Iyer et al., 2008a).

Hierarchical fracturing of orthopyroxene dikes
Hydration reactions may change the petrophysical properties of a rock, i.e. , volume, rheology, density/gravity, magnetic properties and seismic velocities (Austrheim and Prestvik, 2008; Bach et al., 2006). However, hydration reactions may potentially influence the local stress field in the rock Iyer et al. (2008a,b); Jamtveit et al. (2009); Plümper et al. (2012b); Røyne et al. (2008) as well. According to Iyer et al. (2008b), who studied fracture pattern of orthopyroxene dikes, is the effect of hydration negligible in the case of the orthopyroxene dikes. The hydration of olivine in the surrounding dunites, on the other hand, has a major impact on the local stress field and thus on the initiation of the first fracture generation (in the dikes) (Iyer et al., 2008a,b; Jamtveit et al., 2009; Plümper et al., 2012b; Røyne et al., 2008).

These fractures display the same or almost the same orientation. If the hydration is persistent, the first generation of fractures will determine the orientation of the next fracture generation, which, in the case of hierarchical fracturing, would be perpendicular/subperpendicular to the previous. Such a hierarchical process will self-accelerate and produce new reaction surfaces and fluid pathways as long as water (and reaction minerals are) is available, resulting in steadily smaller domains separated by fractures (Jamtveit et al., 2009; Røyne et al., 2008).

The replacement of orthopyroxene and olivine (forsterite) by serpentine takes place under different conditions. Hydration of orthopyroxene takes place at higher temperatures ($\sim$500-600° C at 1-10 *kbar*) than forsterite ($\sim$375-470° C at 1-10 *kbar*). This implies that hydration of the orthopyroxene dikes temporally took place before hydration of the dunites, and as temperature decreased into the reaction interval of dunites, the orthopyroxene dikes had stopped reacting (Iyer et al., 2008b).

The volume increase that would follow $\sim$60% serpentinization of the dunites, was estimated to be $\sim$25% (Iyer et al., 2008a), implying that once the surrounding dunite started to expand, the dikes would be subjected to compressional stresses normal to the dunite-dike contact. No free boundaries would lead to 'squeezing' and subsequent hierarchical fracturing of the dikes (Iyer et al., 2008a,b).

Some geochemical consequences of serpentinization
Iyer et al. (2008a) divided the hydration history deduced from the modeling of phase relations, into five successive stages. Each is characterized by certain temperature intervals reflecting either a continental ($30°C$) or an oceanic ($70°C$) geotherm. If the serpentinization process was modeled to be sequential with pulses of low and high fluid flux that affected discrete domains, the reactions would mobilize Ca, Si, Mn, Fe, and Na, resulting in the excess of different elements in fluids. These would, at different times, be redistributed both within a given lithology, but also to various lithologies through shear

and deformation zones. For instance, the mobilization and transport of Ca would result in the formation of rodingites, as reported in the field by Austrheim and Prestvik (2008).

Observed chemical and textural relationships from the Leka ophiolite associated with serpentinization provide arguments to support that alteration took place while the LOC was still a part of the oceanic lithosphere (Austrheim and Prestvik, 2008; Iyer et al., 2008a). One possible exception is the late antigorite formation, which post-dates the formation of mesh-texture in olivine. The late antigorite formation might be due to either increased temperatures during regional Caledonian metamorphism or an excess of silica in fluids (Iyer et al., 2008a).

Rodingitization and serpentinization

Austrheim and Prestvik (2008) studied the relationship between serpentinization and rodingitization based on a locality at the LOC. This locality differs from reported localities elsewhere, by its location in the transition zone of the layered ultramafic cumulates and plagioclase-rich layers of gabbro and anorthosite.The observed rodingite locality is part of a meta-somatic column where rodingite layers are replaced by a clinozoisite-rich zone followed by a LILE enriched anorthosite zone along strike. The rodingite layers are transected by fractures also transecting plagioclase-rich layers.

The ultramafic parts of LOC are differently serpentinized, which, together with observed structures, relates rodingitization to the Ca-releasing processes of serpentinization and chloritization of clinopyroxene. Such structures, e.g. , protomylonite bands, fractures transecting layers, and shear- and breccia zones, provide vessels for mobilized Ca and other elements in the fluid phase. Grossular garnets observed along many of these fractures and in shear zones corroborate the suggestion that these fractures acted as channel pathways for enriched fluids.

The serpentinization of clinopyroxene is assumed to be the primary source of CaO, but several replacement textures (and mineral analyses) revealed that secondary processes must have taken place. A balanced Gresens analysis was performed to determine the quantities of elements that were required to form rodingite and those that were in excess. Assuming constant volume, ∼20g of CaO, ∼3,5 g of SiO_2 and ∼5 g of FeO were added, while ∼10,5 g Al_2O_3, almost all Na_2O and all K_2O were removed per 100 g protolith (the adjacent plagioclase-rich layer).

Six possible Ca-releasing (R1-R3) and Ca-consuming (R4-R6) reactions were outlined, where the first four are hydration reactions leading to supersaturation of the fluid. These are:

R1: cpx → srp

R2: cpx → chl

R3: cpx → amph

R4: cpx1 → cpx2

R5: opx → cpx - two stages, an intermediate chlorite-stage may occur before cpx saturation level is reached.

R6: ol → cpx

Observations and analyses demonstrate that the formation of rodingite is a likely result of fluid-rock interaction between different lithologies and multiple fluid pulses, during which the fluids constantly evolved in composition.

The strongly hydrated rocks at Leka are associated with hydration of the ocean floor, thus Austrheim and Prestvik (2008) suggest that rodingitization at Leka is related to hydrothermal processes at the spreading center over which it was formed.

Chapter 2

Field observations

2.1 Introduction

The Leka ophiolite was visited in summer of 2011 and 2012. The purpose of the first visit was to get an impression of the LOC in general and to locate a suitable place to study the relationship between deformation and serpentinization in detail. It was decided to investigate shear zones in dunites belonging to the layered cumulate section south of Kvaløya farms (Figure 2.1). Eight drill core samples from deformation/breccia zones at outcrop A (Figure 2.3) were acquired.

During the second visit additional six drill cores were sampled from deformation/breccia zones at outcrop B (Figure 2.3).

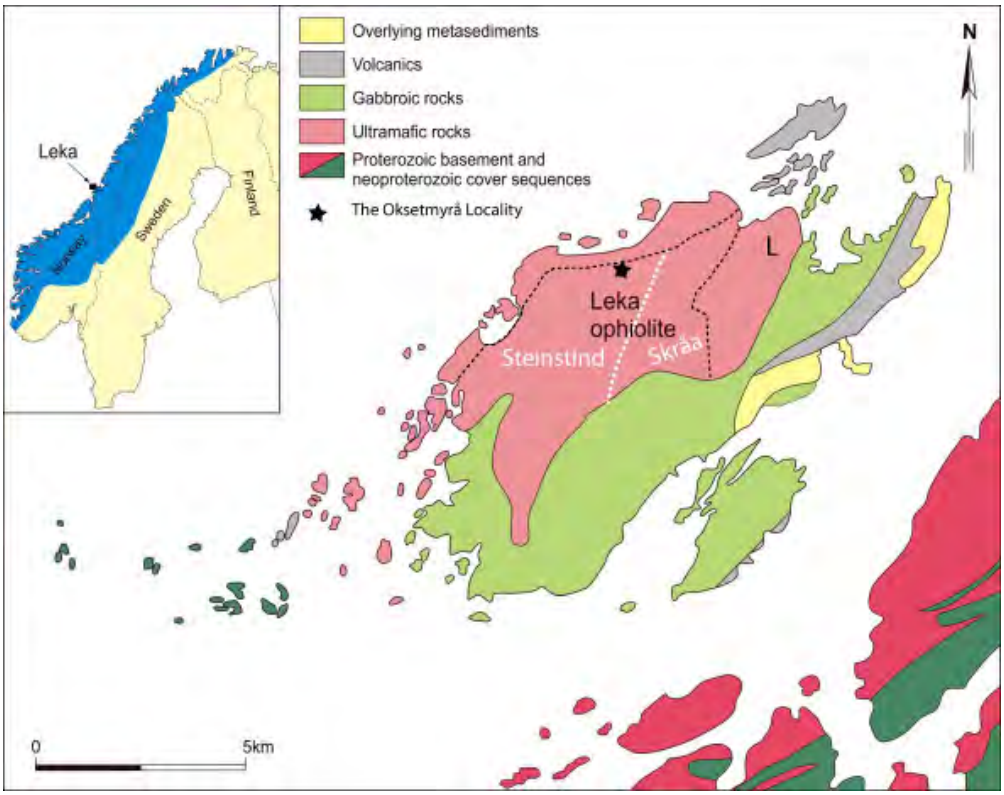

Figure 2.1: Geological map of the island of Leka. Black star indicate the location of investigated outcrops at Oksetmyrå. L = Lauvhatten. Modified from Austrheim and Prestvik (2008).

2.2 The Oksetmyrå Locality

The Oksetmyrå locality is situated in the layered cumulate section southwest of the harzburgites at Lauvhatten, in the Steinstind block (Figure 2.1). Two adjacent outcrops north of Ørneredet have been mapped in detail (Figure 2.3). The rocks in the mapped area are predominantly peridotites, but with layers of pyroxenite. The variation in composition is visualized by layers of different weathering colors spanning from yellow to gray (Figure 2.2) reflecting dunite and chromite-rich clinopyroxenite respectively. The alternation of the lithologies described below represents a primary (now altered) banding formed by a magmatic process.

(a) Photo direction SW towards Ørneredet, (Ø), seen from outcrop A.

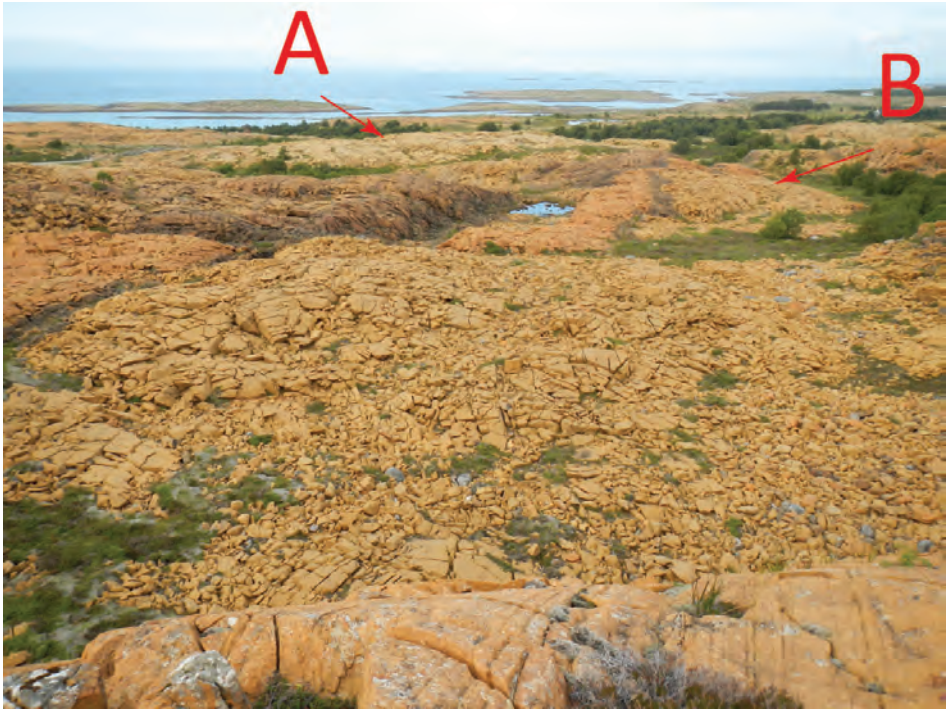

(b) Photo direction NE towards Oksetmyrå.

Figure 2.2: Overview over the field area. (a): Almost all of outcrop A consists of dunite. In contrast we see that the rocks in the background display different colors at their weathered surface, reflecting rhythmic units of peridotites and pyroxenites. (b): Same area as (a) seen from another angle. Different units can be distinguished on the basis of their surface color (section 2.2.1). Note the intense fragmentation of the dunites in the foreground, where frost wedging has contributed to the surficial fracturing.

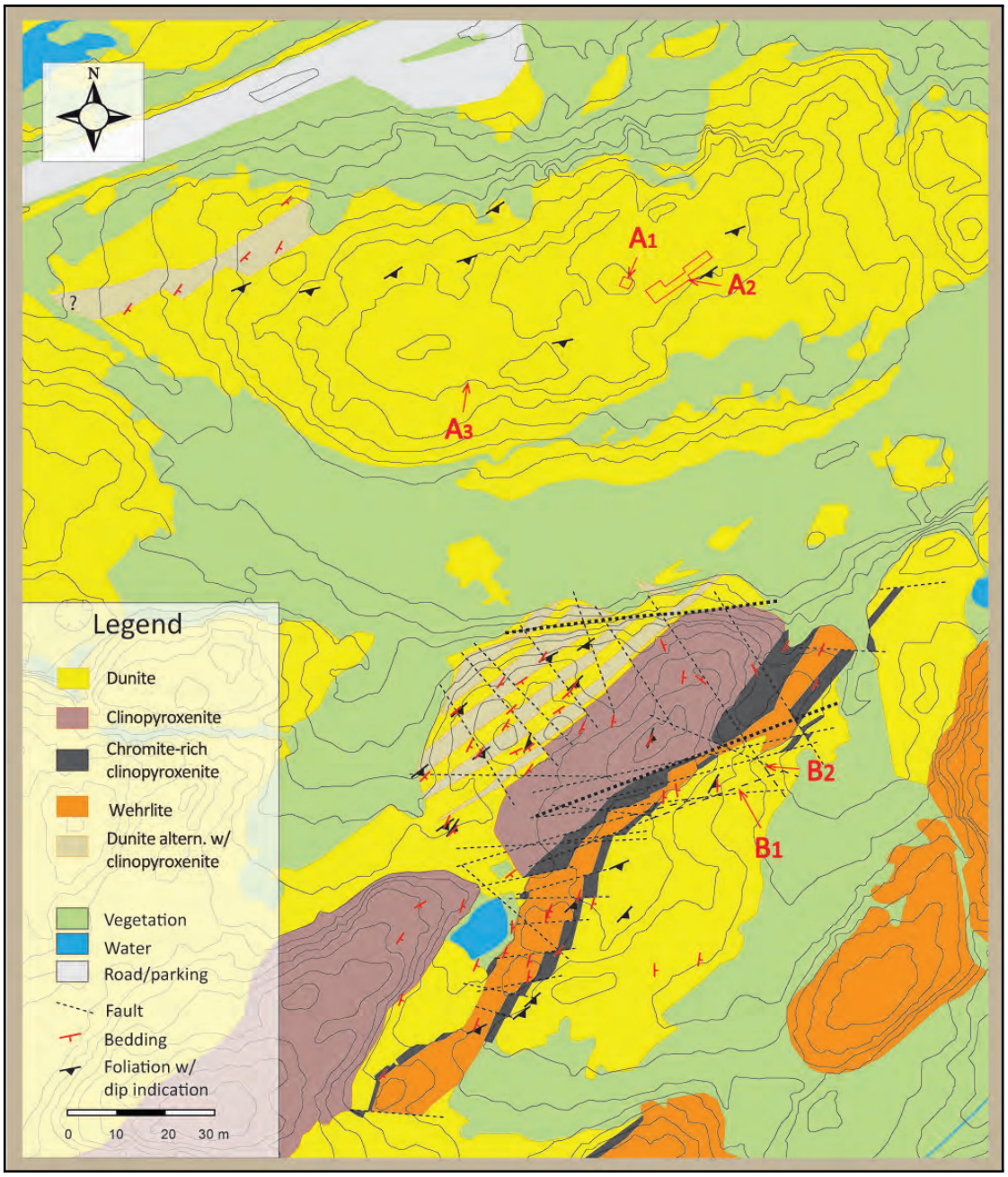

Figure 2.3: The detailed map shows the two adjacent outcrops, named A and B, at Oksetmyrå. Subscripts 1, 2 and 3 refer to subsites described and mapped in this chapter. The color coding of the mapped lithologies is chosen to fit the color impression of the weathered surface, which again reflect the constituent minerals present and the mass ratio between them. The dominant minerals are olivine, clinopyroxene and serpentine. The following five ultramafic lithologies were mapped: dunites(1), clinopyroxenite(2), clinopyroxenite with chromite(3), wehrlite(4) and a unit of alternating dunite and clinopyroxenite(5). The number in brackets refers to the number assigned to the various lithologies presented on the next pages.

2.2.1 The layered sequence at Oksetmyrå

The rhythmic layers at Oksetmyrå dip steeply and strike in a northern direction. The layering is defined by alternating layers of dunites, clinopyroxenite, clinopyroxenite with chromite, wehrlite and a unit where dunite and clinopyroxenite alternate on cm scale. The composition of ultramafic rocks can be visualized in a classification diagram as shown below (Figure 2.4), where the green area indicates the rocks at Oksetmyrå.

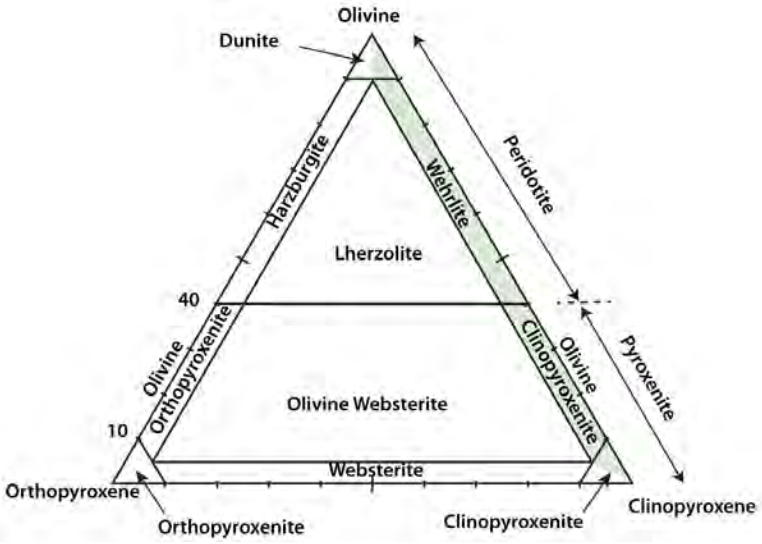

Figure 2.4: Ultra mafic diagram with lithologies from Oksetmyrå marked with green.

The differences can be described as follows:

1. The **dunites**, which display a typical yellow weathered color, are cut by intersecting fractures and occasionally make up block fields. Still, the dunites at outcrop A give a more massive impression compared to the other units. It is in the dunites that we find deformation zones with and without breccia, and mylonite zones (subsection 2.2.5). The dunites have locally developed a penetrative foliation defined by planes of a lighter material. Examples of penetrative foliation are displayed in Figures 2.13 and 2.14.

2. The **clinopyroxenite** consists of alternating gray and red weathered layers which provide a murky appearance to this unit (Figure 2.5c and 2.5f). It contains variable amounts of olivine and has locally developed a small scale banding. The clinopyroxenite constitutes the topographically highest area at outcrop B. These layers are less fragmented compared to other units.

3. **Chromite-rich clinopyroxenites** are darker in color compared to the clinopyroxene layer described above. This is partly due to a lower olivine content and partly due to a higher chromite content. The unit consists of two distinct layers that both show increasing deformation towards a major fault trending 070N (Figure 2.17) where the layers partly deform into a fault rock (Figure 2.18). The width of the segments vary from less than 0.5 meter to ∼9 meter. These layers are intensely fractured (Figure 2.6).

The chromite-rich clinopyroxenite layers border the wehrlite (described below) on two sides along the strike. The widest of the two chromite-rich layers also borders the reddish gray clinopyroxenite unit mentioned above. Close to and at the large 070N fault displayed in Figure 2.17, the layers get considerably thinned and deformed.

4. **Wehrlite** weathers with yellow-orange to orange colors. Orange-weathered layers dominate, but alternate with more olivine rich layers (5-20 cm wide). The latter layers display a yellow-orange weathering color and have a negative relief compared to the orange-weathered layers (Figure 2.5e). In addition they have a more finely grained texture than the former.

   The wehrlite is less fragmented than other units at outcrop B, except where it forms a narrow "strait", (Figure 2.6b), between two chromite-rich clinopyroxene layers near one of the main faults. This is demonstrated in Figure 2.6b and 2.17 which show how the wehrlite layer follows the ridge between two chromite-rich clinopyroxene layers (Figure 2.5b and 2.5e). This rock also occurs as a schistose fault rock (Figure 2.18).

5. In the unit of **alternating dunite and clinopyroxenite layers**, the dunite layers are thicker than the clinopyroxene layers (Figure 2.5a and 2.5d). The clinopyroxenite layers vary from 1 cm to a few tens of cm in width. Detailed mapping of these layers is not possible at the chosen map scale and this variation has therefore been assigned the color light gray on the map (Figure 2.3). The clinopyroxene layers display a light gray to green color and contain larger grain sizes of clinopyroxene mixed with fewer and smaller sized olivine grains. Green diopside crystals have been observed locally (Figure 2.13c) as well as slumpfolds (Figure 2.7).

Outcrop A is dominated by dunite with local layers of clinopyroxenite (layer 1 and 5). At outcrop B all five lithologies are present (Figure 2.2 and 2.3).

(a) Dunites and clinopyroxenites(5),

(b) Wehrlite(4)

(c) Clinopyroxenites(2)

(d) Dunites and clinopyroxenites(5)

(e) Wehrlite(4)

(f) Clinopyroxenites(2)

Figure 2.5: Dunites alternating with layers of clinopyroxenites or wehrlites of variable thicknesses. (a) from outcrop A and (d) from outcrop B: Examples of small scale alternations of dunite and clinopyroxenite(5). (b) and (c): Wehrlite(4) at outcrop B. This unit has likely layers of varying dunitic to pyroxene ratios as the layers weathers with colors from orange to more yellowish at the surface. The yellow-orange layers have negative relief compared to the orange layers. (c) and (f): Examples of clinopyroxenite alternating with layers of a slightly more peridotitic composition at outcrop B. The numbers in brackets refer to the unit numbers on the previous pages.

(a) Fractured clinopyroxenite(3)

(b) View towards SW.

(c) Chromite-rich clinopyroxenite(3) make up a block field. View towards NE.

Figure 2.6: The chromite-rich clinopyroxenites are less serpentinized and more brittle compared to other layers. (a): Some fractures extend into the adjacent units, like the dunite in the foreground and the wehrlite in the background. Frost wedging has contributed to the surficial fracturing. (b): The wehrlite is less fragmented than other units at outcrop B except where it forms a narrow "strait" between two chromite-rich clinopyroxene layers near the main 070N-fault. (c): Wedge shaped segment of chromite-rich clinopyroxene viewed towards the large fault.

Slumpfolds

Figure 2.7: Slump folds of layers most likely of diopside at Outcrop B. These layers cut through the dunitic rocks. Fracturing often takes place along the boundary between the weaker layer of clinopyroxenite and the dunite. As can be seen from the photo on the right, the cleavage did not develop as an axial planar cleavage indicating that cleavage formation post-dates the folding.

Slumping of deposited cumulates occurs in the transition between the downward slope of the magma chamber and the chamber floor where convection currents are deflected (Gill, 2010) (Figure 2.8). Slumpfolds are thus common structures in layered igneous rocks, and have been observed e.g. at the Karmøy ophiolite (Sturt et al., 1979). At Leka, within the unit of small scale alterations of dunites and clinopyroxenites(5) we find a few thin and folded cumulate layers adjacent to thin straight layers of clinopyroxenite, in the dunite. Their textures are similar, but their structure differs. The straight layers show an axial planar cleavage, while the cleavage in the folded cumulate layer displays a penetrative cleavage oblique to the folding indicating that cleavage formation post-dates the folding. The slumpfolds have a greenish tinge and a positive relief as illustrated in Figure 2.7.

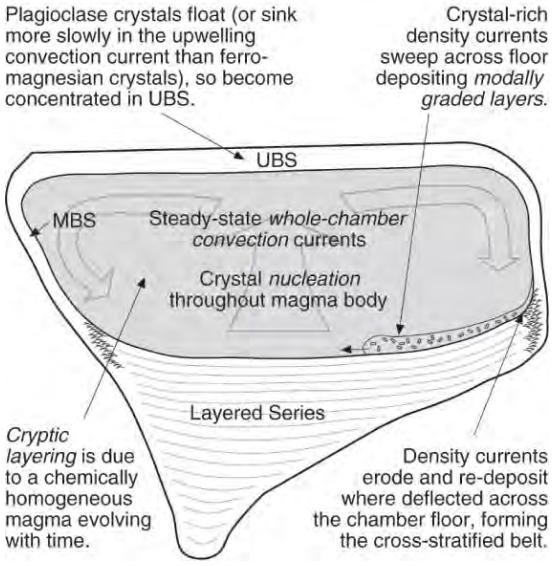

Figure 2.8: Carton of a Skærgaard-type magma chamber. MBS - Marginal Border Series. From Gill (2010).

Cross-bedded magmatic layering in wehrlite

Figure 2.9: Rock fragment of wehrlite with cross-bedded layering adjacent to chromite-rich clinopyroxenite.

Well developed magmatic layering is prominent at outcrop B. Figure 2.9 displays an example of layering and cross-stratification in wehrlite adjacent to a rigid layer of chromite-rich clinopyroxenite. The layers display the same variation in orange and yellow-orange weathering colors as other wehrlites at outcrop B.

According to one hypothesis, cross-stratified layers may form at the boundary between the Marginal Border Series (MBS) and the Layered Series (Figure 2.8) due to erosion and re-deposition caused by deflecting density currents (Gill, 2010).

(a) Chromite sheetfold

(b) Dipping chromite bands

(c) Fan-like chromite

Figure 2.10: Dunites with cumulate chromite layers at outcrop B. Primary bands of clinopyroxene, have a greenish tinge and display a coarser grain size than the black chromite. At this site the clinopyroxene layers are mostly parallel with the chromite layers. (a): Sheetfolds, folded layers of chromite and layers of clinopyroxene. The inner short axis of the chromite sheet fold below the book, is 2 cm. Strike and dip of the clinopyroxene band adjacent to the sheetfold was measured to 336/72. (b): The chromite layers appear as intense recurrent black layers in the yellow-weathered dunite. (c): Chromite layers converge at the surface displaying a fan like shape, a shape likely related to the sheetfold.

2.2.2 Chromite Bands

A distinctive feature in the dunite is the primary chromite layers. The chromite layers show secondary features such as faulting/displacement at the mm to cm scale as shown in Figure 2.11. At outcrop A the chromite layers are displaced to a higher degree than at outcrop B and their orientation usually vary between 040N and 050N, and dips between 50 and 60. At outcrop B larger fractures cause interruption in the chromite layer but individual layers can still be followed up to 5-10 meters or more. Chromite layers also get dragged into deformation zones where they disintegrate, contributing to the chaotic appearance of these zones. The chromite grains at B are more densely packed giving the bands a black color. As shown in Figure 2.10b they come in groups of two - three recurrent layers. Layers may converge at horizontal faces and display sheetfolds on vertical faces (Figure 2.10).

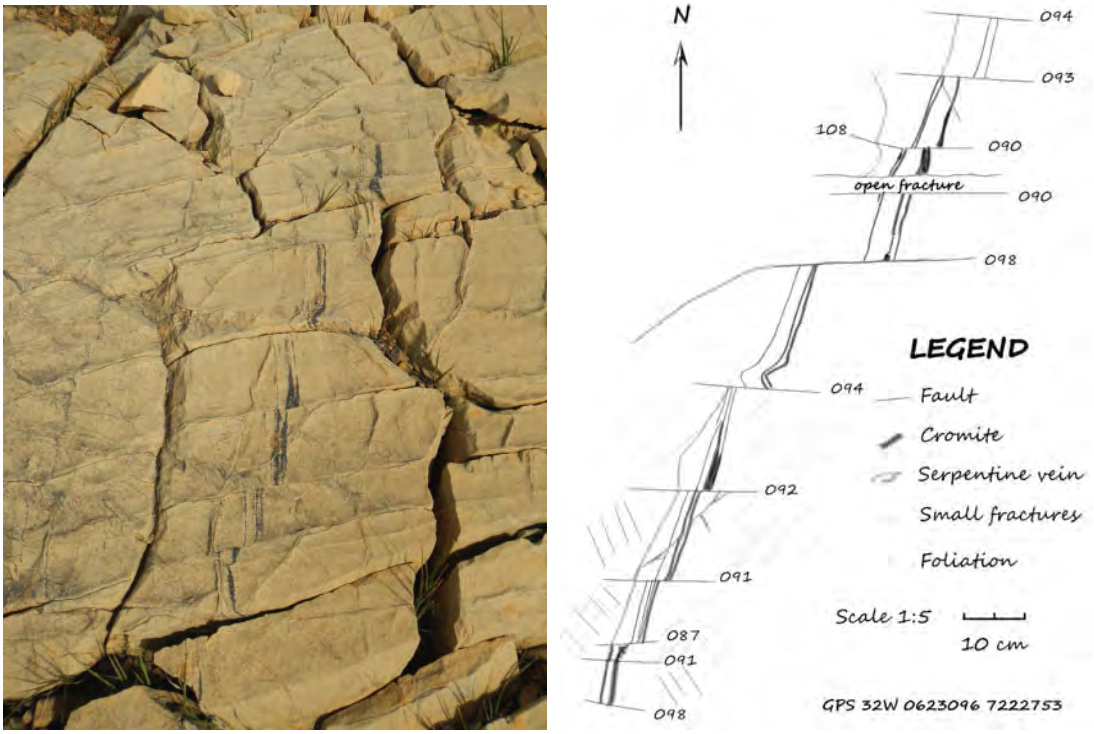

Figure 2.11: Example of faulting of chromite at outcrop A. The sketch shows faulting of chromite shown in the photo. Total displacement of chromite bands over the sketched area is approximately 45 cm. The measured directions of the different segments of the chromite bands vary from 003 to 027N.

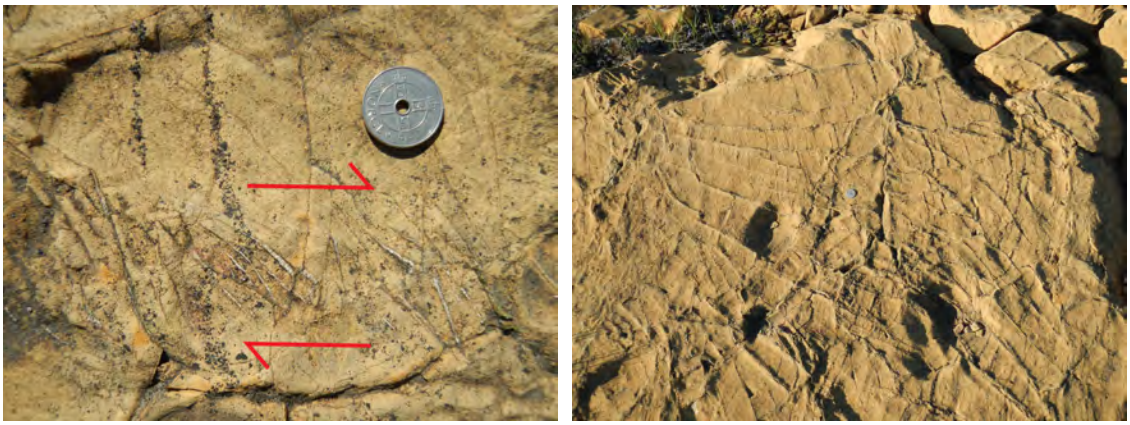

(a) **(b)**

Figure 2.12: (a): En échelon serpentine veins and off-set chromite layers. Diameter of coin is 2,1 cm. Outcrop A. (b): Localization of serpentine veins in a fault network. Outcrop B.

2.2.3 Penetrative Foliation and Serpentine Veins

A NE-SW to EW foliation is transected by EW to NE-SW trending shear- and fault zones.

In the dunite the foliation appears as tiny interrupted lines consisting of a brighter material at the surface. A cut face, through sample LEKD0712, perpendicular to the penetrative foliation, reveal a fine and systematic serpentine vein network (Figure 2.14b). The vein network coincides with the foliation as it appears at the surface where it forms tiny troughs, less than 0,5 mm across. In some troughs black transversal fractures resembling cooling contraction fractures, shorter than the cross-section of the trough ($<$ 0,5 mm) and even thinner ($<$ 0,1 mm), can be observed with a magnifying glass (to small to be photographed in the field).

Over relatively larger areas, compared to the size of the investigated outcrops, the foliation disappear completely at the surface and reappear only across small patches of 0.5 to 1 m^2. The main trend, $\sim$ 045N to 055N, is consistent across the investigated outcrops (Figure 2.3 and 2.13b).

The dunites at outcrop B are more serpentinized than the dunites at A. As seen in Figure 2.14b serpentine occurs as tiny networking veins as well as larger more localized serpentine veins (Figure 2.12b). Between veins, thin fractures predominantly orientated perpendicular to the veins are observed. These are small fault networks (Figure 2.12).

(a) Penetrative foliation.

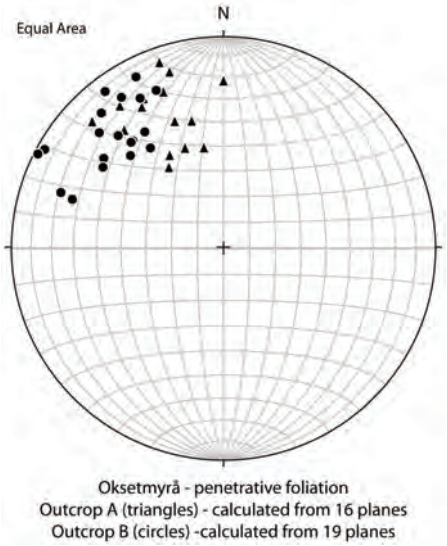

(b) Poles to foliation planes. Main trend is NE to SW.

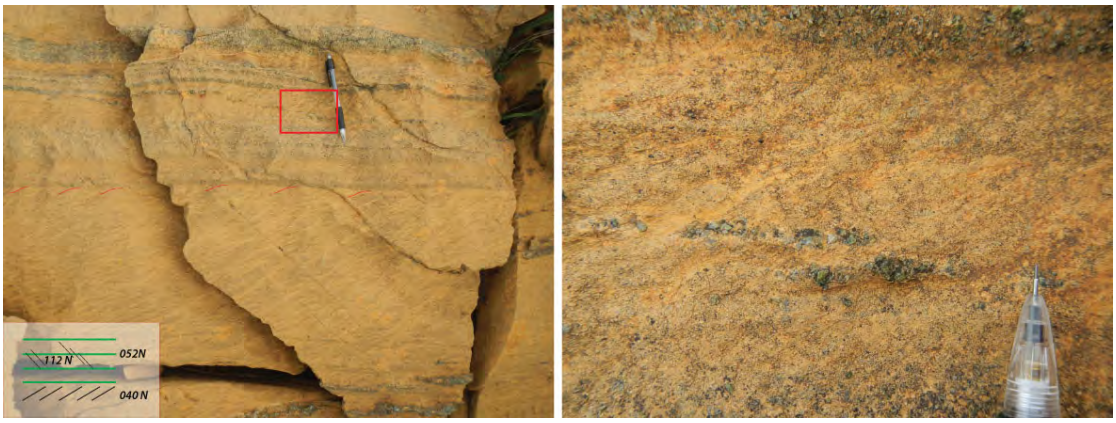

(c) Penetrative foliation and diopside crystals, outcrop B. Outlined box is enlarged right.

(d) Penetrative foliation extending into clinopyroxenite layers.

(e) Serpentine veins in pyroxenite.

Figure 2.13: (a): Short white dashed lines indicate foliation direction. A mylonite zone is indicated by a dashed red line put slightly to the right of the zone outcrop A. (b): The stereonet shows poles to foliation planes measured at both outcrops. Triangles for outcrop A and circles for outcrop B. (c): Well developed foliation in dunite. The foliation is drawn into the clinopyroxene layer. Larger green diopside crystals are visible in photo right. (d): The foliation in the dunite fades into the pyroxene layers. (e): Serpentine veins mark a fracture cleavage in pyroxenite. (c, d, e from outcrop B).

(a)

(b) Regular network of serpentine veins.

Figure 2.14: (a): Alteration zones around a central fracture and penetrative foliation in dunite at outcrop A. The gray lines (red arrows) that define the boundary between the alteration zones and the host rock interrupt the penetrative foliation, which continues in the host rock at the opposite side. The foliation is not restricted by the orange-weathered patches (example outlined by dashed black rim). A selection of foliation planes are marked with dashed white lines. (b): The hand specimen, (LEKD0712, outcrop B), is cut perpendicular to the foliation. The foliation is defined by an anastomosing network of thin serpentine veins. Note that the weathering zone forms wedges in the upper part of the photo.

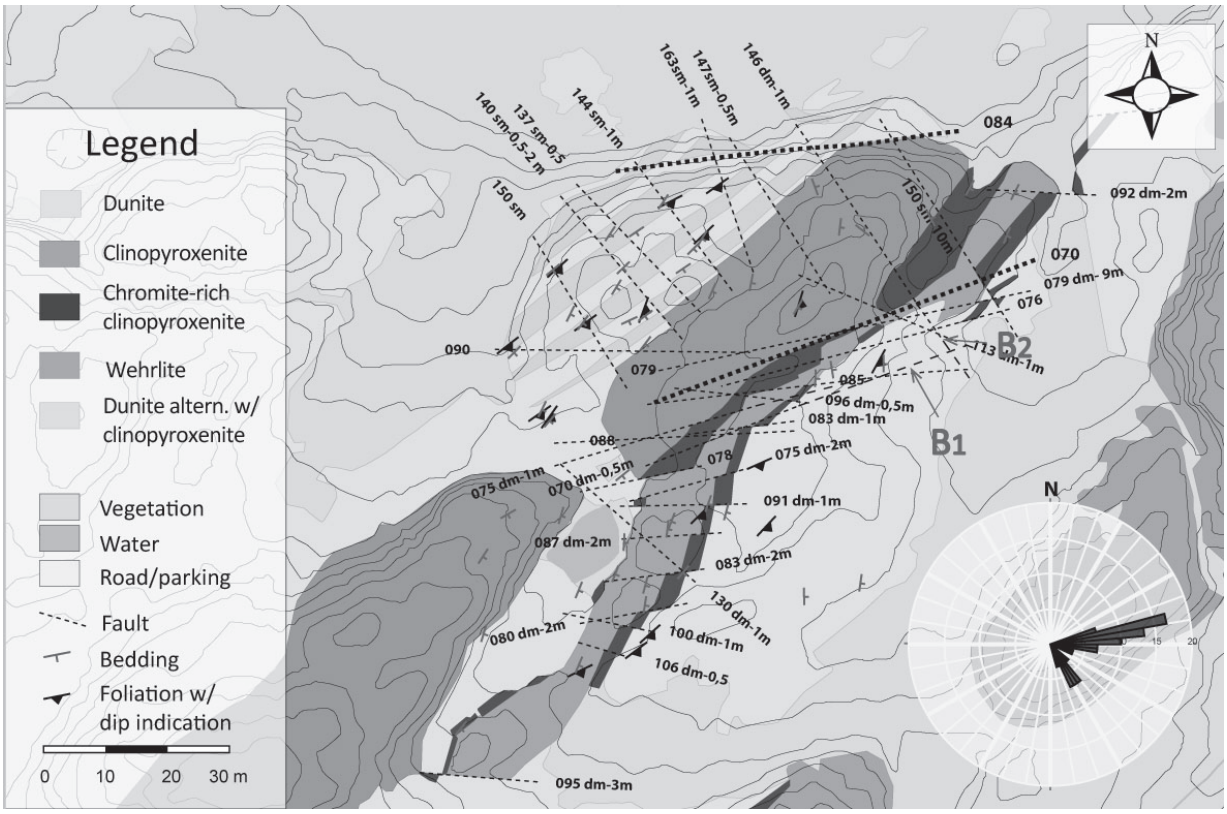

Figure 2.15: Detail of map shown in Figure 2.3 with fault directions at outcrop B at Oksetmyrå. sm - sinistral movement, dm - dextral movement. Number followed by, m, approximates displacement in meter. Inset in the lower right corner shows rose diagram (equal area) of measured fault directions. (Parameters: n = 30, bin size: 5%, value of perimeter: 20%)

2.2.4 Faults Zones

Faults

There are two sets of larger shear/fault zones at outcrop B showing displacement at a scale of tens of centimeters to meters. Two prominent faults marked with bolder dashed lines on the map in Figure 2.3 and Figure 2.15, both belonging to the NEE-SWW fault systems, dominate the outcrop. One of them, a larger fault, aligns 070N across the middle of outcrop B, clearly displacing fragmented chromite-rich clinopyroxenite layers. The trend was approximated by taking the compass bearing in the two opposite fault directions. The other prominent fault, which strikes 084N or E-W, bounds the outcrop towards the vegetation at the northside of the outcrop. Strong magnetism observed along this fault is attributed to the presence of magnetite.

Most of the smaller sinistral faults intersect the 070N and 084N faults at high angles. Due to intense fracturing which turns the dunites into a block field at several places, any continuation of these faults is difficult to record.

The total dextral movement of the thinner of the two chromite-rich clinopyroxenite layers across a distance of ~ 60 meter was estimated to 9 meter. It has to be noted that the individual segments of the layer are thinned and stretched and that they have rotated to varying degrees.

Ductile deformation in connection to the 070N fault is apparent through the development of shear bands (S-C structures) in the fault rock, which also contains larger unfoliated clasts of clinopyroxenite derived from the adjacent chromite-rich clinopyroxenite layers (Figure 2.18). Clast long-axes up to 150 mm were measured (Figure 2.18d).

In addition to the larger shear/fault zones there are innumerable small faults displacing chromite and other layers at the millimeter to centimeter scale, e.g. , as shown in Figure 2.11 and 2.12.

The aerial photograph (Figure 2.16) show that outcrop A and B are separated by a fault. The displacement vertically and/or horizontally can not be determined.

Fractures
The outcrops by Oksetmyrå are transected by fractures in scales ranging from mm to tens of meters. Larger fractures at outcrop A, as shown on photo (Figure 2.20) and on map (Figure 2.24), trend NNE-SSW and are intersected by (sub)perpendicular smaller fractures. The largest fracture system is (sub)parallel to the primary layering.

Titus et al. (2002) investigated fault populations from aerial photographs (lineaments) and in the field and found that larger faults are predominantly oriented NE-SE, while smaller faults generally are oriented NW-SE.

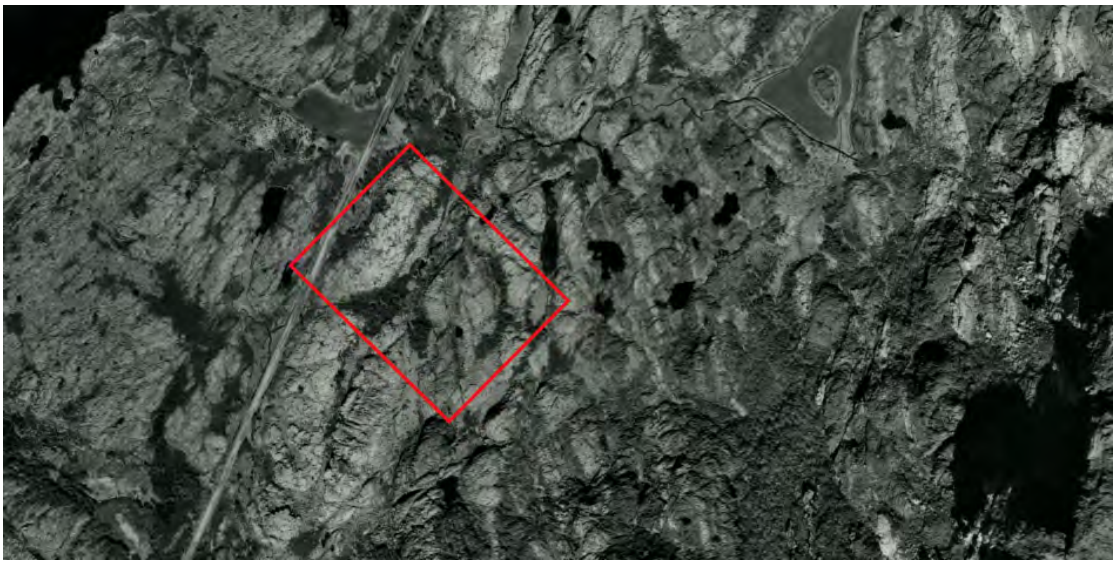

Figure 2.16: Arial photograph from Blom Norkart mapping, scale 1:10000, date:06.05.04.

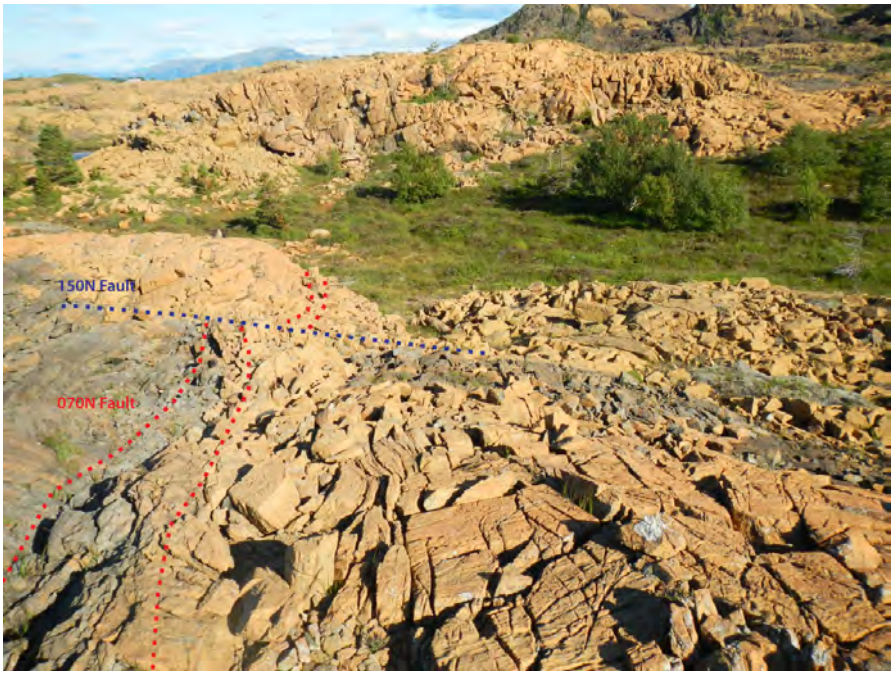

(a)

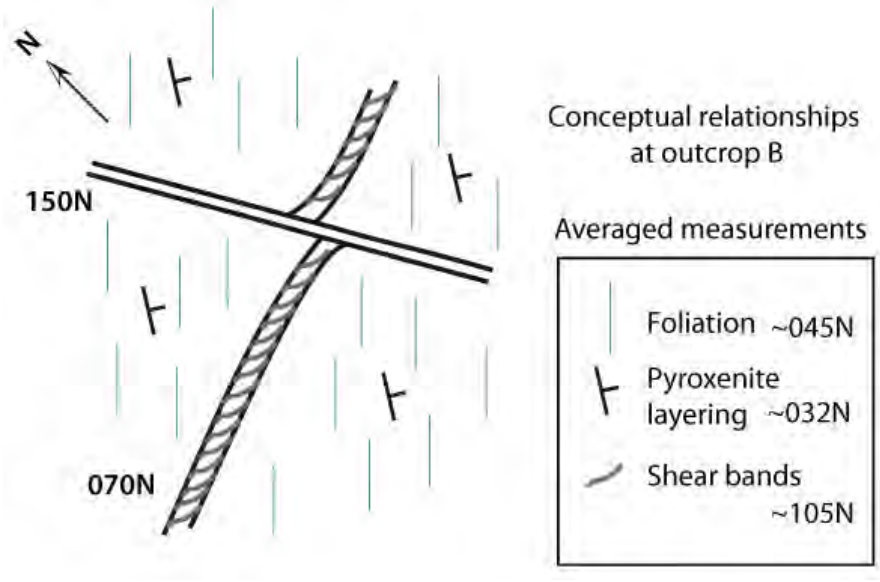

(b)

Figure 2.17: (a): The clinopyroxenite to the right (dashed red lines) is a part of a larger shear/fault zone system at outcrop B. In the front wehrlite is bounded by chromite-rich clinopyroxenite. A 150N trending fault displacing the clinopyroxenite with up to 10 meters. The 070N fault deflects into the 150N fault. Shear sense of the 070N fault is sinistral. (b): Conceptual relationship between faults, penetrative foliation and clinopyroxenite layering at outcrop B. The foliation is averaged over 19 measurements, while the clinopyroxenite layers are averaged over 20 measurements.

(a) Schistose fault rock.

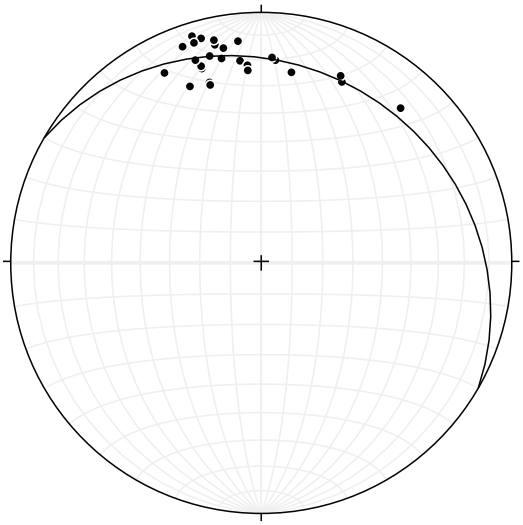

(b) Poles to fault planes

(c) Shear bands in fault rock.

(d) Clasts in fault rock

Figure 2.18: Outcrop B. (a): Wehrlite fault zone. This fault zone is a continuation (to the SW) of the fault zone displayed in Figure 2.17. Sinistral faults transect this 070N trending fault at high angles. (b): Poles were calculated from 27 planes, i.e. , 27 measurements over 30 meters along the large 070N trending fault. This fault zone was measured at approximately 1 m intervals where possible. Strike and dip of best fit great circle: 300/22. (c): Shear bands reveal left lateral shear sense. (d) : S-tectonite. Shear bands deflect around clinopyroxenite clasts of different sizes.

2.2.5 Deformation Zones in Dunites

This subsection gives a general description of deformation zones in dunite, including detailed maps over selected drill core sampling sites (Figure 2.21 and 2.24). The map in Figure 2.24 represents a continous deformation zone.

In this thesis, I have chosen to divide the deformation zones into three main types, but the zones overlap and display varying degrees of similar structures:

- Mylonites and larger damage zones
- Matrix or clast supported deformation/breccia zones
- Small-scale (network of) fractures with alteration zones

Mylonites and damage zones

Mylonite zones consist of fine to ultra fine olivine grains with sharp boundaries to the host rock (Figure 2.19). They can be traced several tens of meters (Figure 2.19a). Locally, they converge into damage zones (Figure 2.20) where the boundaries become transitional, and the mylonites often disintegrate and mix with the host rock. The mylonites display various shades of gray depending on grain size distribution.

(a) **(b)**

Figure 2.19: (a): This mylonitic zone strikes 300N, dips steeply (88) and can easily be traced for about 30 meters. This zone is the darkest of the observed zones probably caused by a high content of fine grained chromite and very fine grained olivine. (b): Location of drill core LEKD1111 at subsite A3 before drilling.

Figure 2.20a shows a larger damage zone where mylonite zones merge into a broader chaotic zone. These damage zones contain spaced (1-2m) orange-weathered, elongated and fractured rock fragments. Rock fragments are locally surrounded by flow-like structures comprising disintegrated mylonites.

Field relationships suggest that these rock fragments could be a relic of an orthopyroxene dike. A few larger rock fragments have retained a hierarchical fracture system

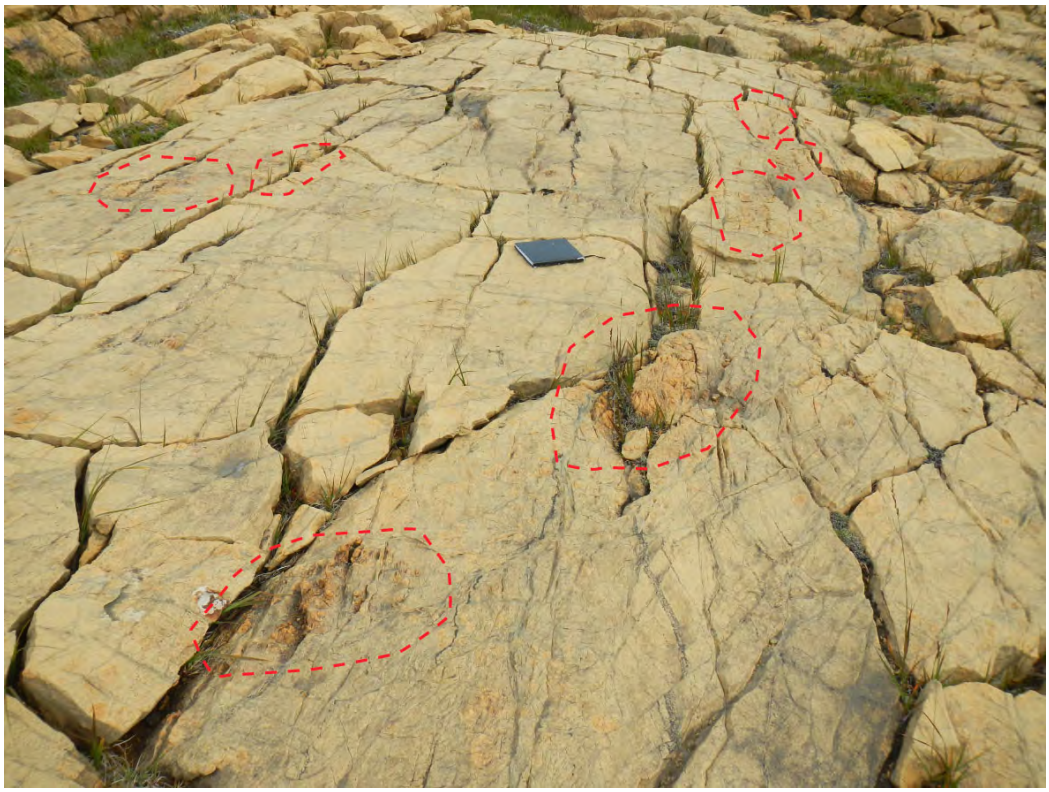

(a) Larger deformation zone

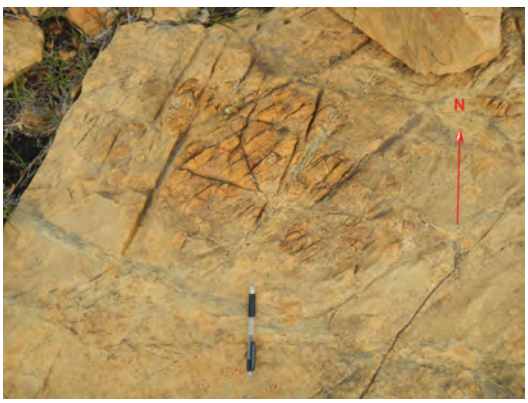

(b) Orange-weathered rock fragment

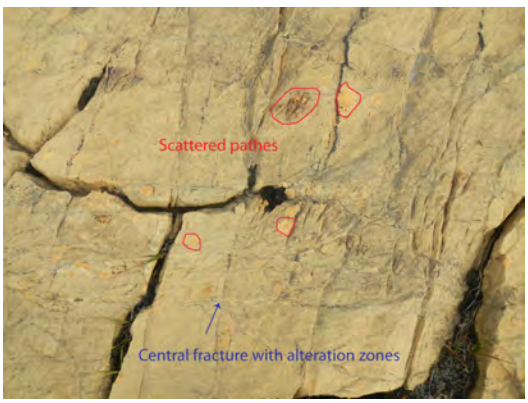

(c) Fragmented orange-weathered patches

Figure 2.20: (a): The deformation zone covers a larger area ($\sim$ 15-20 m^2) where several mylonite zones converge. This zone differs from similar zones by including larger orange-weathered rock fragments.(b): Closer look at a larger rock fragment displaying two fracture systems. (c): Intense fragmentation of orange-weathered rock into small patches. The photos are taken $\sim$ 5-10 meters north of grid 1 in the map displayed in Figure 2.24. Outcrop A.

(Figure 2.20b). Hierarchical fracturing of orthopyroxene dikes by compressional stresses caused by expanding dunite during serpentinization has been reported by Iyer et al. (2008b). Displaced chromite bands and fractures with bright alteration zones contribute to the chaotic expression of the damage zones.

Deformation/breccia zones

Several grayish deformation/breccia zones cross-cut the dunites at both outcrop A and B. Their strikes vary from 050N to 120N. The zones contain numerous small faults. The width of individual deformation/breccia zones vary from cm to tens of cm and can usually be traced for a few meters along each strike. Locally, the zones form domains of 2-5 m^2 of highly deformed breccias(Figure 2.22). These zones can be either matrix or clast supported, but gradual transitions occur frequently. They may appear chaotic like in Figure 2.25. Their directions usually vary from E-W to NE-SW. The deformation/breccia zones can also be found locally within the previous described damage zones, e.g. , subsite A2.

Subsites A1, A2, B1 and B2 are all located in deformation/breccia zones and examples from these sites follow below.

Subsite A1
Subsite A1 has a striking variety of deformation features. The most prominent features are the $\sim$ EW deformation/breccia zones (Figure 2.21 and 2.22). These zones contain flow-like structures of very finely grained material (olivine) and show a sharp contact to the host rock. Rounded and angular clasts of different sizes are observed within the shear zones where chromite bands sharply deflect eastwards following the shear zone.

Two main fracture orientations, sub-perpendicular to each other, are the second-most dominating feature. The E-W running fractures displace chromite bands at the cm scale, but the amount of displacement over distance can not be established with certainty at this site. Observation of a vertical face at the lower left side of the area (Figure 2.22), indicate both lateral and vertical movement. Foliation is weak and trend 058N where visible at the surface.

Four drill cores, LEKD0311, LEKD0411, LEKD0511 and LEKD0611 (Figure 2.22), were sampled within the mapped area, $4m^2$, (Figure 2.21), and cover several deformation features.

Subsite A2
Subsite A2 is part of a larger damage zone shown in the map displayed in Figure 2.24.

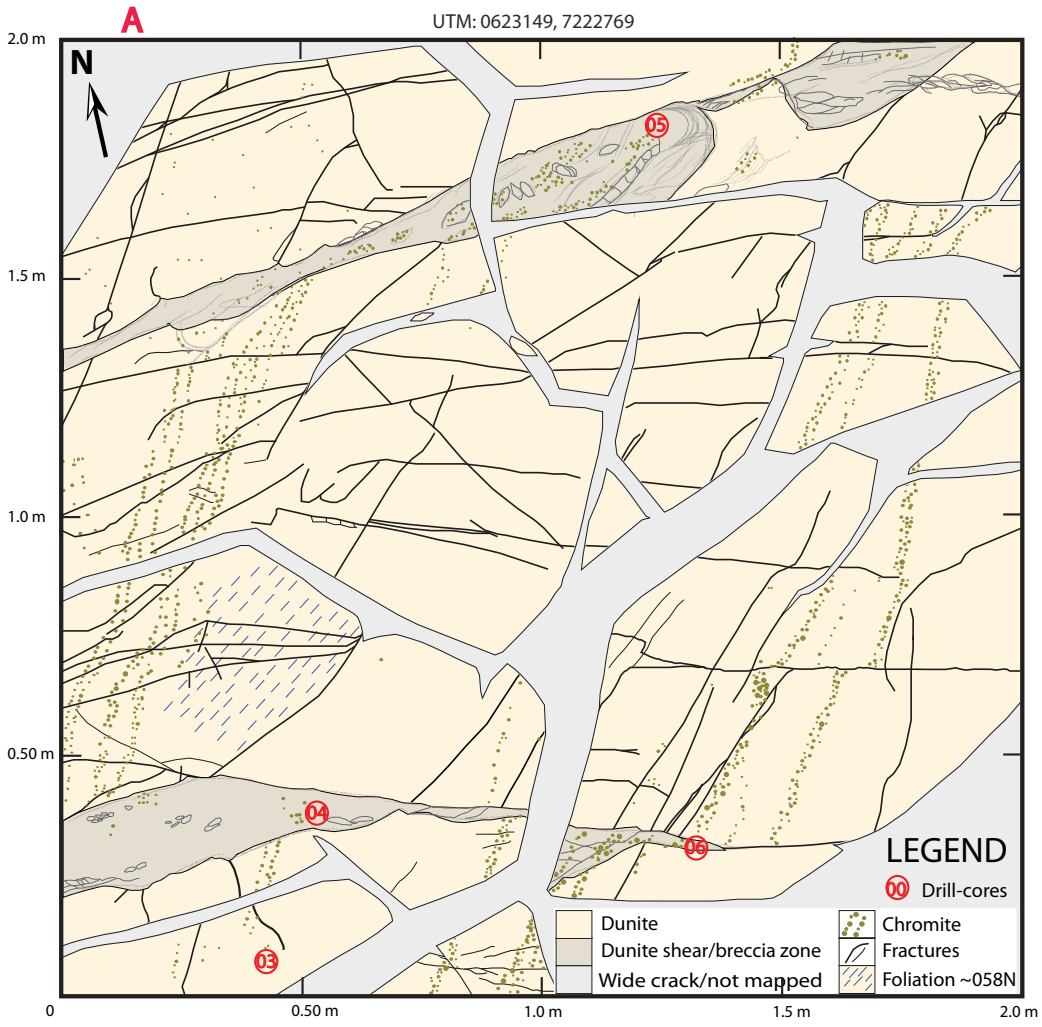

Figure 2.21: Subsite A1. The map covers 4 m^2. Red numbers indicate drill core samples **LEKD0311**, **LEKD0411**, **LEKD0511** and LEKD0611 (boldfaced samples were analyzed by electron micro probe). There is a successive displacement of chromite bands caused by small faults. Chromite bands are dragged into the damage (dunite shear/breccia) zones where they more or less disintegrate into the zone, which contribute to the dark appearance of these zones together with fine grained olivine. The damage zones display various structures such as clasts, both with angular and rounded shapes. At this site the damage zones strike $\sim$ EW and the chromite bands $\sim$ 040N. The strike differs from the direction of chromite bands in Figure 2.11, which strikes between 003 - 027N. Foliation is weak locally.

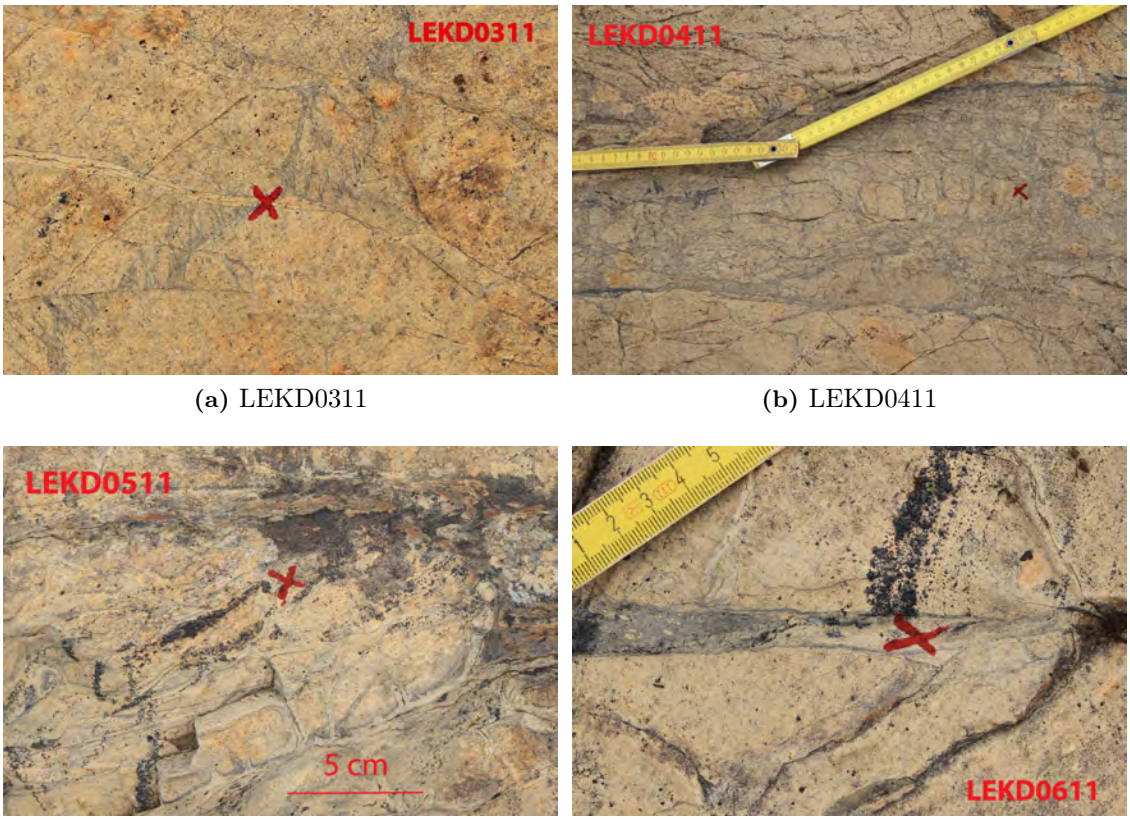

(a) LEKD0311 **(b)** LEKD0411

(c) LEKD0511 **(d)** LEKD0611

Figure 2.22: Details from subsite A1. Red crosses show locations of drill core samples and are mapped in the previous figure. (a): Alteration zone around a central fracture (described in the following subsection). It is the only drill core sampled from outside a deformation/breccia zone. A fine web of thin serpentine veins halts at the alteration zone and continues at the other (b): Transition from matrix to clast supported breccia. The contact between the breccia zone and the host rock is sharp and defined by dark rims. Chromite bands get dispersed when entering the breccia zone. (c): The core was drilled at the small area between two displaced chromite bands in a clast supported breccia (the upper deformation/breccia zone at the grid map 2.21). Below the displaced chromite we see rectangular clasts zones bounded by lighter colored alteration zones with a gray alteration front towards the center of the clasts. Depressions adjacent to these clasts suggest that some clasts have been spalled off. (d): Very finely grained olivine in a host rock of coarser olivine. In the breccia to the left there are a few small, rounded clasts in a very fine matrix. A chromite band is dragged to the left into the shear zone and thereby constitutes a sharp contact between the two different parts. The dark color is caused by fine grained chromite and olivine. Chromite grains are randomly distributed.

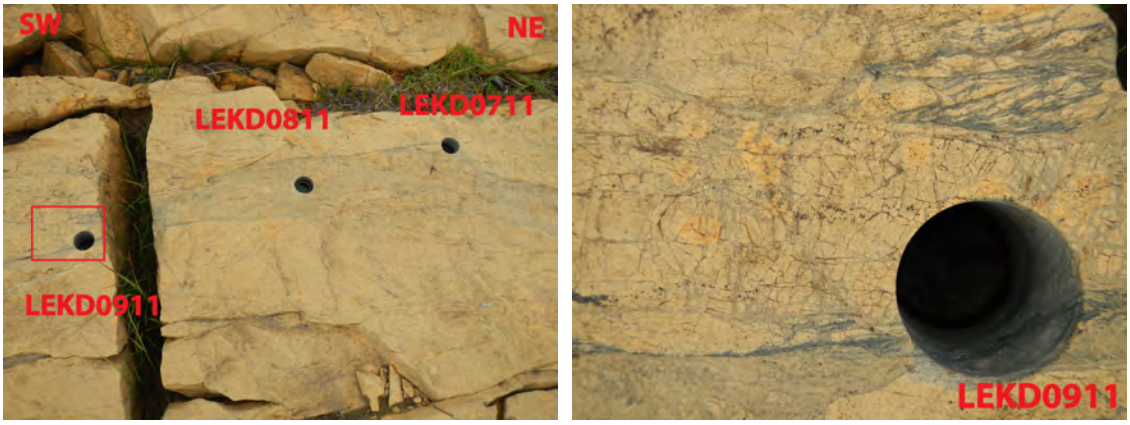

(a) Subsite A2 **(b)**

Figure 2.23: (a): Deformation features like hierarchical fractures, matrix supported breccia and mylonitic flow bands at subsite A2. Shear sense is top to the right. (b): Within the field of view there are 6-7 dominant fractures with smaller fractures oriented perpendicular/subperpendicular to the dominant fractures. Chromite grains are aligned with a few of the dominant fractures.

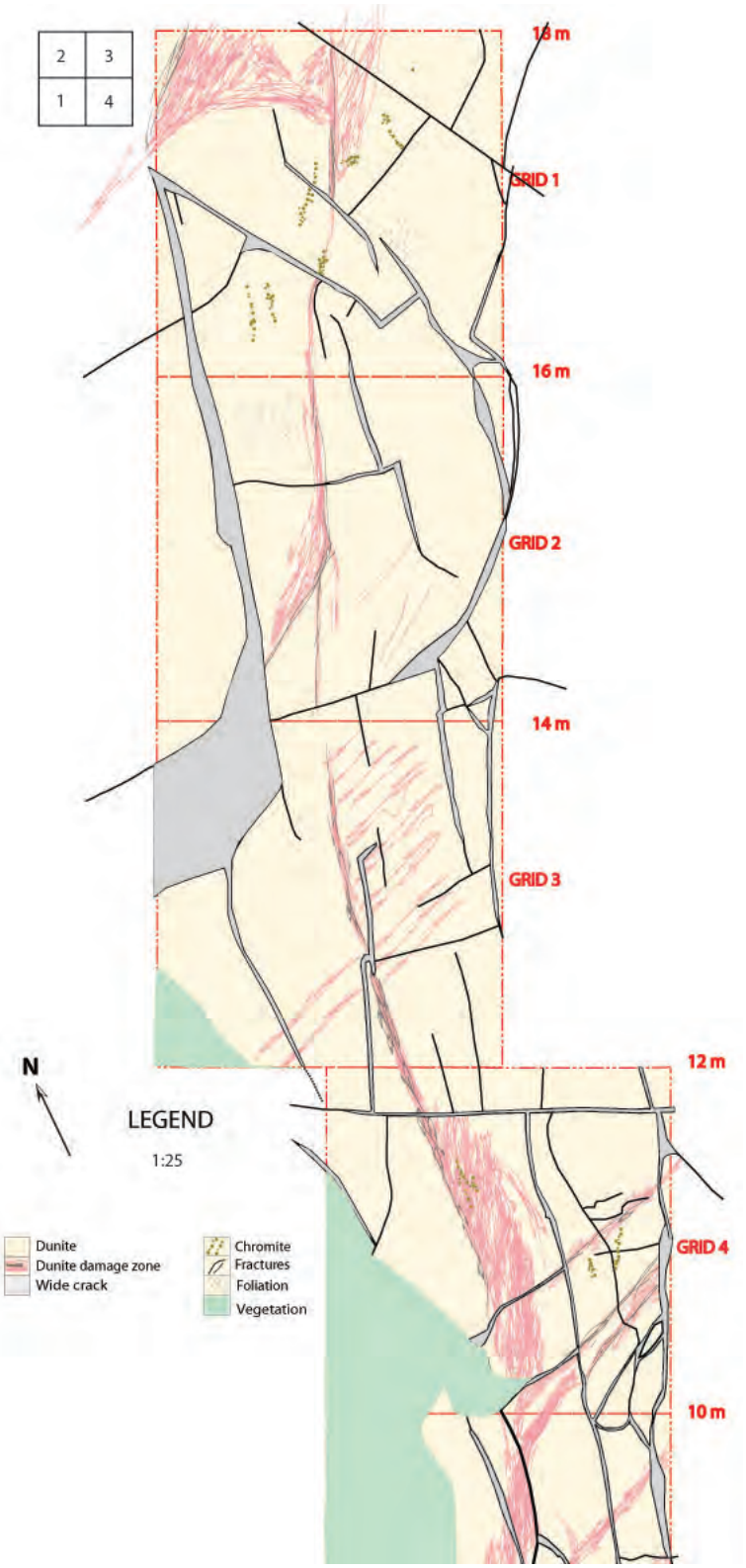

Figure 2.24: The map covers 40 m^2 and depicts different features along strike (chromite bands, foliation and fractures). The degree and amount of shear, brecciation and flow structures vary along strike. In grid 1 and 2 the dunite switches appearance from being a smooth dunite and to brecciated. Grid 4 was moved 1 meter to the SE due to vegetation. Scale 1:25.

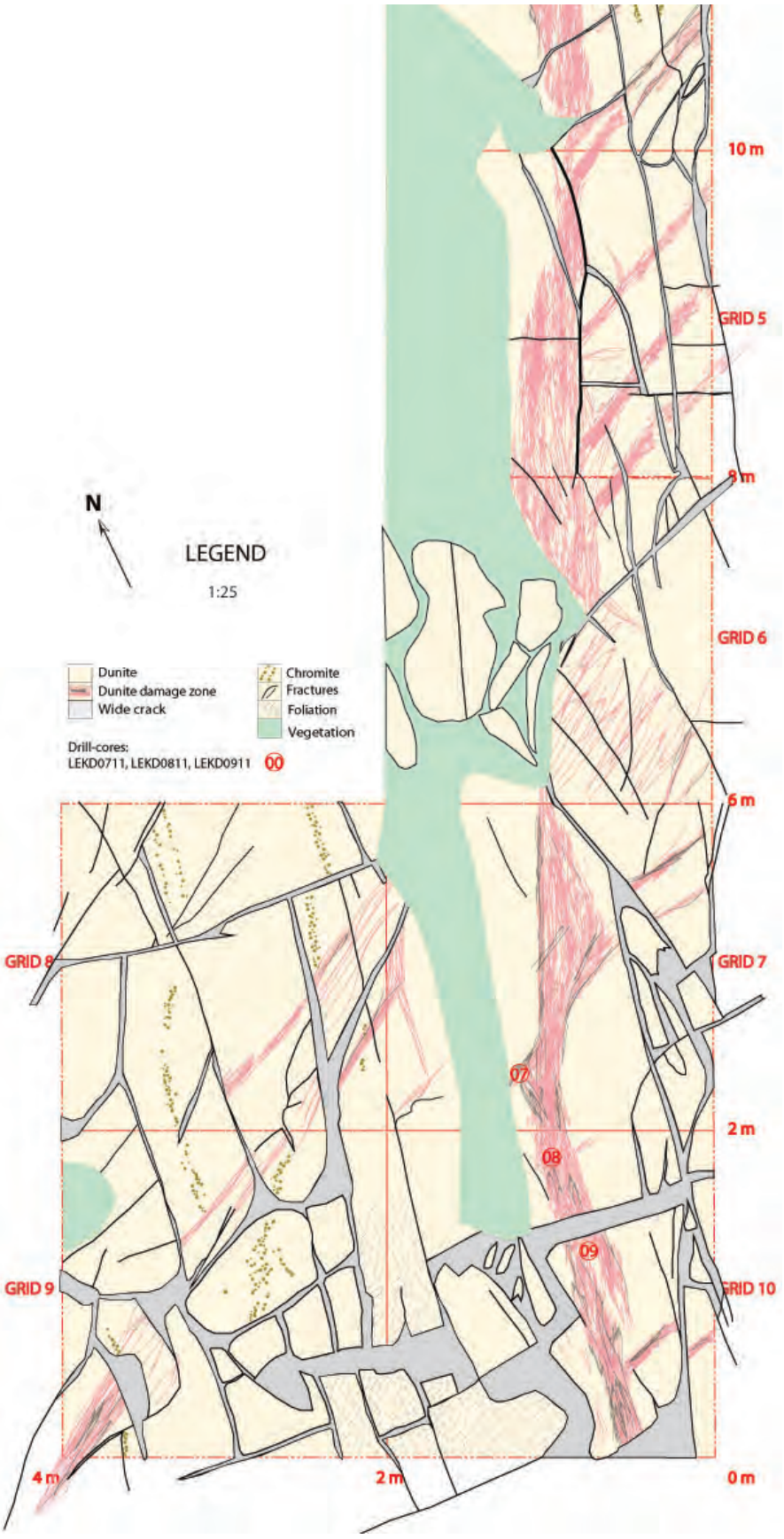

Figure 2.24: Continued figure from previous page includes subsite A2 in grid 7 and 10, with location of sample LEKD0711, LEKD0811 and LEKD0911 plotted. Scale 1:25.

Subsites B1 and B2

(a) Subsite B2 **(b)** Deformation zone

Figure 2.25: (a): Subsite B2 with Prof. Håkon O. Austrheim in the background. The deformation zone continues in elongated and separated blocks similar to the pictured one. (b): Chromite bands are deflected into the deformation zone where they become chaotic. Outcrop B.

The deformation/breccia zones at outcrop B differ from those mapped at subsite A1 by the higher degree of serpentinization and of organization of olivine into domains by grain size. Serpentine at B is to a greater extent localized in networks of thicker veins. Olivine seems to be sorted into domains with similar grain sizes.

Drill cores
The drill cores were collected from four deformation/breccia zones and one mylonitic zone. The purest olivine was found in sample LEKD0311 at subsite A1 (Figure 2.22). Eight drill cores in total, were sampled from outcrop A, while six drill cores were sampled from outcrop B (Figure 2.3). Subsite A1 is depicted in a detailed grid map of 4 m^2 (Figure 2.21). Three drill cores were sampled from subsite A2. Subsite A2 is depicted in a coarser map covering 40 m^2 (Figure 2.24). One drill core was sampled at subsite A3 (Figure 2.19).

Four drill cores were sampled from subsite B1 and a further two from subsite B2. Both subsites are located in deformation/breccia zones. Locations are depicted by arrows in the outcrop map on Figure 2.3. LEKD0112, LEKD0212, LEKD0312 and LEKD0412 (B1) were sampled from a 092-096N trending deformation zone (Figure 2.26a), showing a sinistral sense of shear. This deformation zone can be traced from the vegetation on and $\sim$ 6 meters westwards before it is offset by a right lateral displacement of $\sim$ 2 meters. Shortly after, it meets another deformation/breccia zone at an high angle.

Subsite B2 is a deformation zone that can be divided into a brecciated part (LEKD0612) and an anastomosing part (LEKD0512) (Figure 2.26b). The deformation/breccia zone trends 083N. This deformation zone can be followed westwards $\sim$ 10 meter from the vegetation on and into the surrounding block field, where it transects another deformation/breccia zone and later becomes a part of the larger 070N trending fault zone shown as a bold dashed line in the field area map (Figure 2.3).

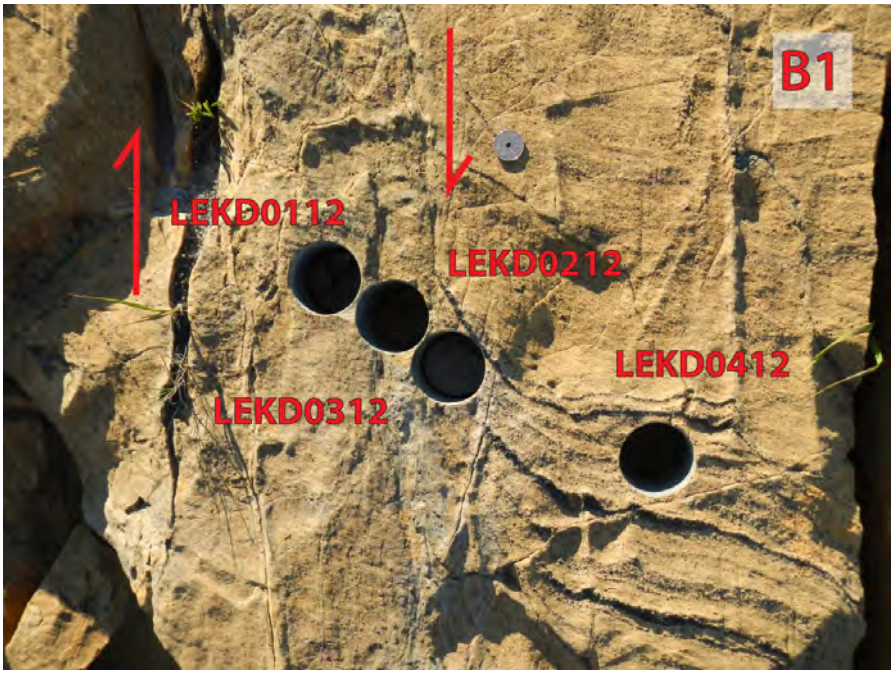

(a) Subsite B1

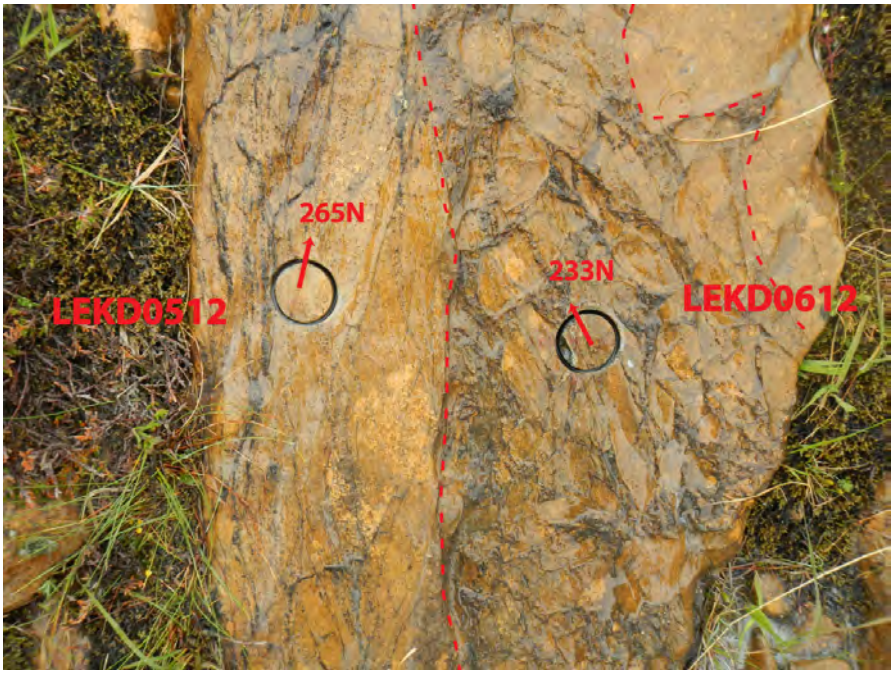

(b) Subsite B2

Figure 2.26: Overview over drill core sample sites at outcrop B. (a): Four cores were drilled in the deformation zone along a profile from undeformed wall rock across the deformation zone. Chromite bands deflect into the shear zone. Several ridges filled with serpentine stands out at the surface. (b): Two cores were drilled in the deformation zone at subsite B2. This subsite is closer to the large 070N fault than subsite B1. The deformation zone in view can be divided in two where the right side contains clasts of dunites surrounded by a matrix of a darker material of smeared chromite bands and fine grained olivine. The left side contains dark anastomosing bands of chromite and fine grained olivine.

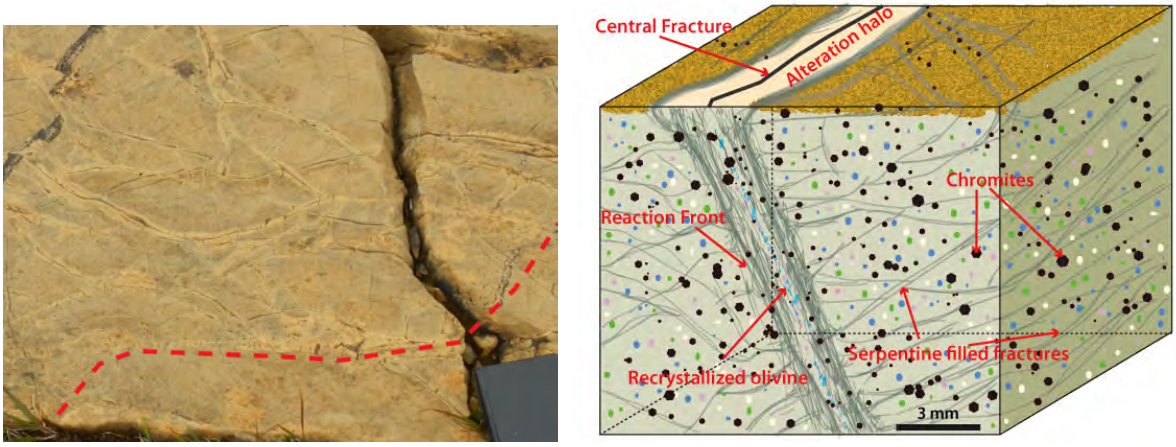

(a) (b)

Figure 2.27: (a): Example of a localized network of lighter colored fracture zones. Observe the displaced chromite. (b): Conceptual relationships of features in an alteration zone around a central fracture. The observations are based on field relations and thinsection of sample LEKD0311 (subsection 4.3.1 in chapter 4). The reaction is initiated when the rock opens up (e.g. by shear) for fluids to react with the host rock. The reaction results in a developement of fine grained olivine in domains at either side of the fracture. These domains are bounded by reaction fronts, dominated by serpentine and very fine grained olivine, towards the host rock. Larger recrystallized olivine grains are aligned with the fracture in the central part.

Small scale (network of) alteration zones (around central fractures)

These zones emanate perpendicularly from a black central fracture and are bounded by gray alteration fronts separating them from the host rock. Any penetrative foliation in the host rock halts against this front, but continues at the opposite side of the alteration zones (Figure 2.14a). A conceptual description of these relationships are given in the caption text of Figure 2.27.The picture collection in Figure 2.28 shows related structures which might represent a progressive development into breccia as described in the captions. This development would involve varying degrees of shear deformation. Small scale alteration zones around central fractures were only noticed at outcrop A.

(a) Fine grained alteration zones around a central fracture

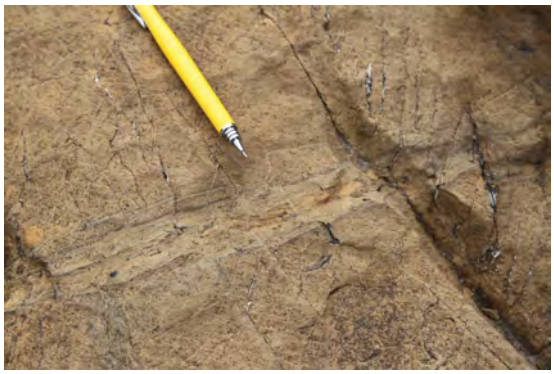

(b) Broader alteration zone

(c) Rectangular clasts with alteration halo

(d) Rounded clasts with alteration halo

Figure 2.28: Outcrop A: The photo serie suggests a progressive development from a narrow fine grained alteration zone around a central fracture to a deformation/breccia zone. (a): Narrow fine grained alteration zones emanates from a central fracture. Parallel gray reaction fronts sharply separate the alteration zone and the much coarser host rock. (b): The fine grained alteration zone gets wider. The black central fracture line transcends into interrupted line fragments. A few later fractures transect the alteration zone perpendicularly. Some serpentine veins terminate against these fractures. A penetrative foliation is present in the host rock, but halts at the alteration zone. (c): Tabular clasts of host rock are rimmed by alteration fronts. The contact between the clast and the alteration front is sharp, while the contact between the host rock and alteration front is chaotic and includes sheared material. A weak penetrative foliation at a low angle to the alteration zone is present. (d): A variation of the clasts in (c). Rounded clasts of host rock. The contact to the host rock is still relatively sharp. The deformation structure resembles mesh textures. Chromite bands deflect around the clasts.

Chapter 3

Methods

3.1 Fieldwork

Mapping
Mapping of outcrops at Oksetmyrå (Figure 2.3) was done by using tracing paper over a topographical map collected from Kilden til arealinformasjon (2012). The detailed map at Subsite A1 (Figure 2.21 on page 42 and the sketch from subsite A2 (Figure 2.24 and 2.24 on page 46 were done on graph papers (1 mm) for easier orientation and scaling of observed structures. The mapping and sketching were aided by a grid made of rope constituting four times 1 x 1 meter squares, i.e. , covering 4 meter^2 of surface at a time. For the sketch, the grid was moved 10 times. A handhold GPS (Garmin 62S), was used for the localization of measure points, layer boundaries, etc. The accuracy was within three meters or less depending on the satellite geometry at any time. A Silva compass was used for strike, dip and trend measurements. The right-hand rule was applied for strike and dip measurements.

Drill Core Sampling
The drill yielded 4.5 cm diameter core samples. 8 drill cores were sampled from outcrop A in 2011. Additional 6 drill cores were sampled from outcrop B in 2012. All cores were sampled from deformation zones in dunite.

Sample preparation
The drill cores and five hand specimen were cut at the Department of Geosciences, University of Oslo. The cut sections from the 2011-samples, except LEKD1111, were prepared for polished thinsections abroad. The remaining cut sections were prepared for thinsections at the Department of Geosciences.

3.2 Analytical Techniques

Optical Microscopy
An Olympus BX 41 mounted with a Leica DFC320 camera was used for petrographic observations and optical microphotographs.

Electron Micro Probe - EMP
Electron Micro Probe (EMP) analyses were performed at the Department of Geosciences, University of Oslo, using a Cameca SX100 instrument fitted with 5 wavelength-dispersive spectrometers (WDS). An accelerating voltage of 15kV and a beam current of 10nA were applied during operation. The diameter of the activation volume of the focused beam was 1-2 μm. Back Scatter Electron (BSE) detectors were used for imaging.

Standard calibration: Ca, Si - wollastonite, Na - albite, K - kalifeldspar, Ti, Mn - pyrophanite, MnTiO3, Fe - pure iron, Cr - Cr2O3, Ni - NiO, Al - corundum, Al2O3, Mg - MgO.

Chapter 4

Petrography and Mineral Chemistry

4.1 Introduction

This section presents textures and observed structural elements from selected thinsections[1]. First I present the petrography from the mapped lithological units as they occur away from the fault zones. Then the petrography from deformation/breccia zones in the dunite at outcrop A and B are presented.

Although the samples from the mapped lithological units were taken up to a few meters from the main faults, it is realized that the intense faulting has affected rocks outside the main fault zones.

Spinel: The opaque phase is dominated by chromite but show a range in composition from chromite to Al-chromite to magnetite.

Modal proportions were estimated by optical microscope.

4.2 The layered sequence at Oksetmyrå

The petrography and mineral chemistry of the mapped lithologies (Figure 4.1) as presented below are based on the following thinsections:

- Dunite(1),LEKD0712.
- Clinopyroxenite(2), LEKD1712.
- Chromite-rich clinopyroxenite(3), LEKD1412.
- Wehrlite(4), LEKD1512.
- Unit of alternating of dunite and clinopyroxenite(5), LEKD1112.

All samples, but the dunite, LEKD0712, were investigated with the electron micro probe.

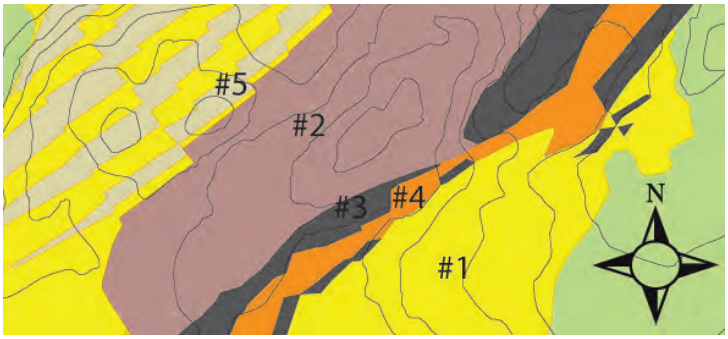

Figure 4.1: Overview showing numbering of the units outcrop B as used in text.

[1]The subsequent thinsections are marked with arrows indicating surface direction.

Dunites(1), LEKD0712

Figure 4.2 shows a typical dunite. The penetrative foliation as seen in the field is oriented vertically and is defined by anastomosing serpentine veins (Figure 4.3). Although the veins are all over the sample, they are locally more closely spaced.

A central fracture transects the sample horizontally resulting in a lateral deflection of vertical veins. This fracture is filled with opaque phases (magnetite?), serpentine and very fine grained olivine. Similar fillings are observed in the obliquely oriented fractures in the upper left corner of Figure 4.2. There is an intense fragmentation along these fractures. These microfaults may be a part of the set of the major faults that is seen to displace the lithologies (Figure 2.3) on a much larger scale.

The dunite contains olivine and serpentine in approximately equally amounts. Accessory chromite is present. The modal estimates are: ∼45-48% olivine; ∼45-48% serpentine; and <1-3% spinel (chromite).

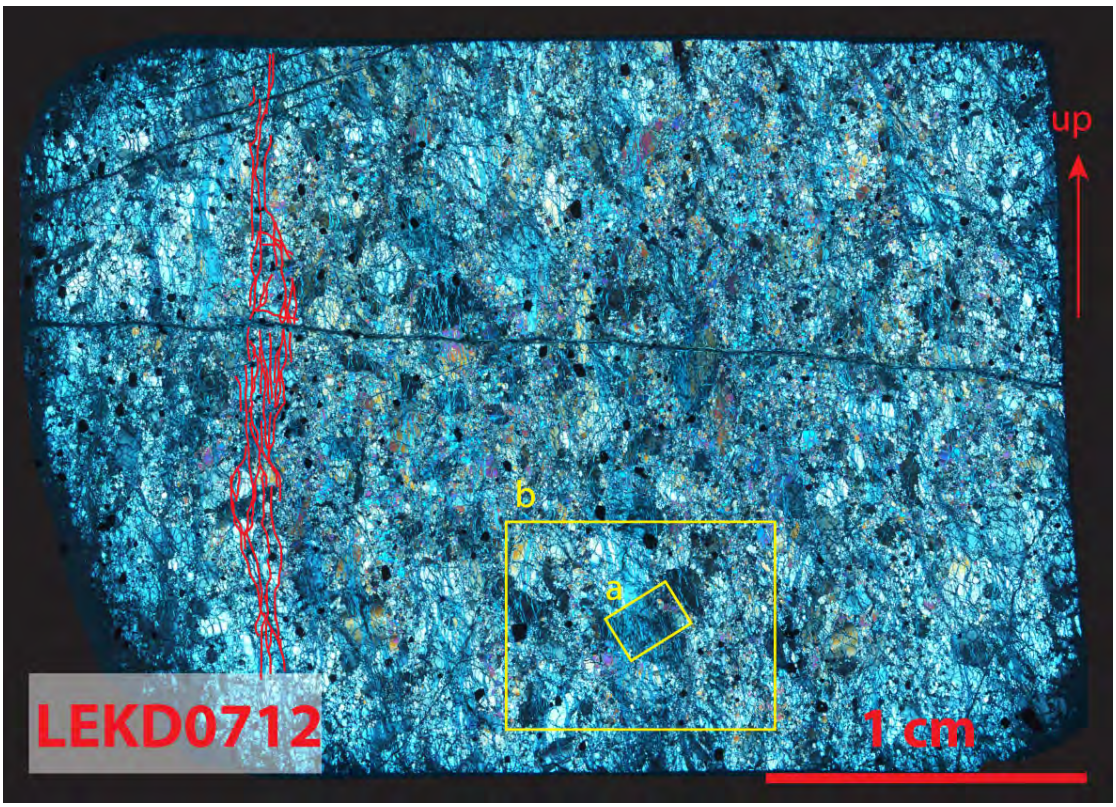

Figure 4.2: Photomerge of thinsection showing dunite(1) with serpentine defining the vertically oriented penetrative foliation. The foliation is highlighted by the red bands.

Olivine displays a grain-size ranging in diameter from <10μm and up to 3mm. An overall coarser-grained texture can be detected as clusters of small olivine fragments with similar orientation (Figures 4.2 and 4.3). These ultrafine to medium sized grains aggregates are elongated and deflects around larger olivine grains with undulose extinction. The elongated domains are parallel with the serpentine foliation (Figures 4.2 and 4.3) and make up areas of optical continuity.

Serpentine occurs in two textural settings. The vein serpentine, which was previously

described, displays fibers oriented perpendicular or subperpendicular to the vein walls. The other type is interstitial serpentine (matrix serpentine).

Chromite is euhedral to anhedral. There is a weak alignment of chromite grains parallel to the serpentine foliation.

The textural evolution described suggest that the dunite evolved from a coarse grained rock and that the main foliation observed in the field relates to serpentinization. The foliation is partly defined by the serpentine veins and partly by elongated aggregates of smaller grains in a serpentine matrix. It is probable that the serpentine allowed the grain to take on the elongated form. It is unclear if the straining of the large olivine grains is the result of an earlier deformation or if it relates to the deformation during serpentinization.

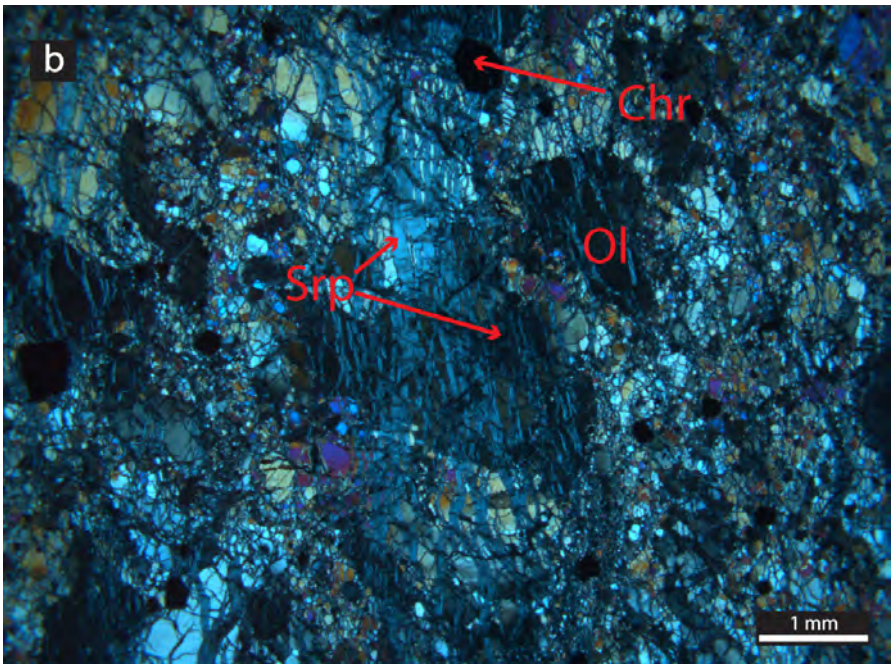

(a)

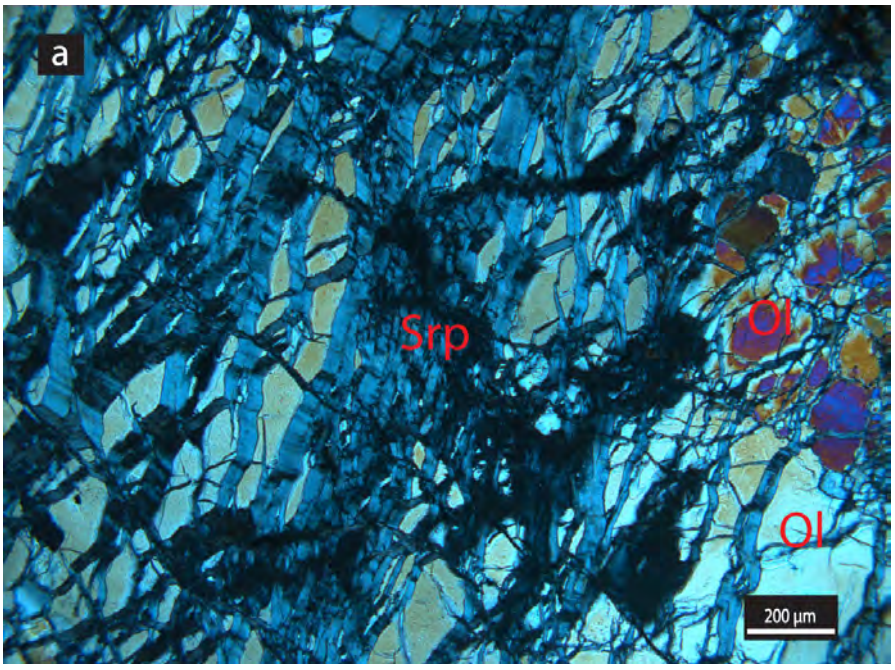

(b)

Figure 4.3: (a): Vertical serpentine veins transect larger olivine grains. (b): An opaque material appear to grow in serpentine. The material might be magnetite which often is associated with serpentine. Optical microphotographs, LEKD0712. Penetrative foliation defined by serpentine veins. Dunite(1), outcrop B.

Clinopyroxenite(2), LEKD1712

This rock is dominated by clinopyroxene with minor amount of olivine and chromite. The sample is moderately serpentinized. Like for the dunite the texture is characterized with a range in grain size with porphyroclasts of clinopyroxene in a finer-grained matrix.

The modal estimates are: ∼35-40% clinopyroxene; ∼50-55% serpentine; < 10% olivine; and <1% chromite.

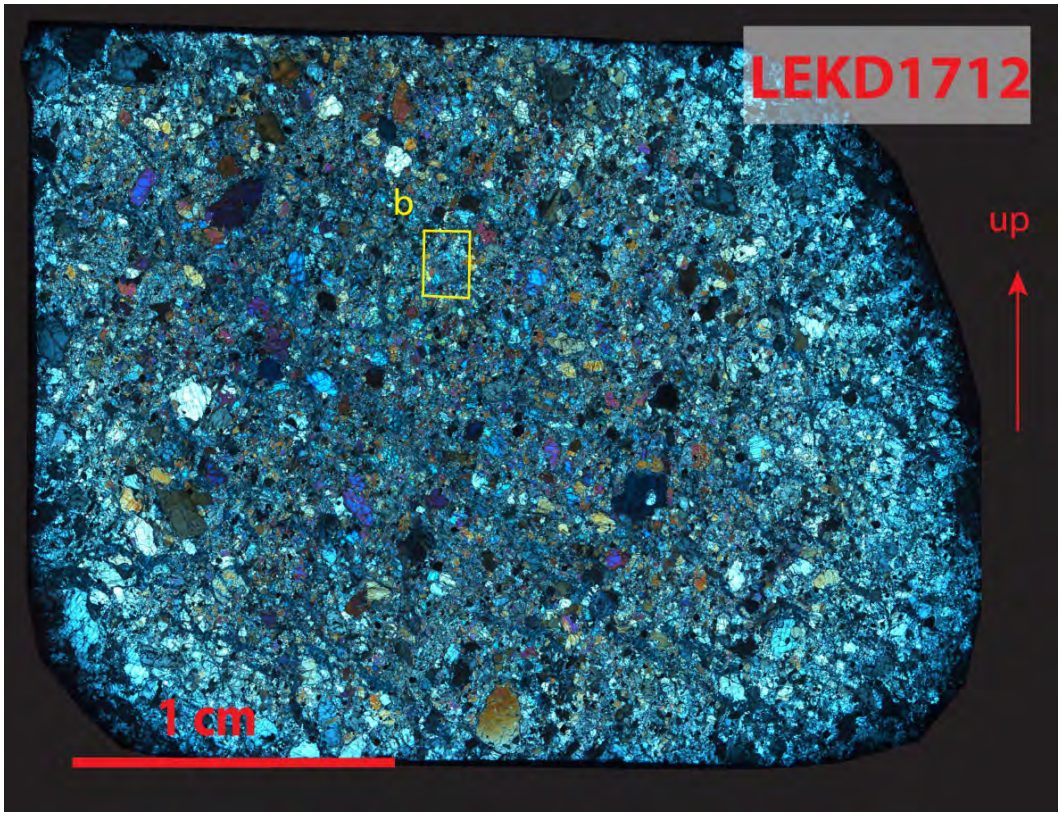

Figure 4.4: Photomerge of thinsection of clinopyroxenite showing a typical porphyroclastic texture. A weak foliation, defined by shape preferred orientation of porphyroclasts runs from the upper left to the lower right. Clinopyroxenite(2).

Clinopyroxene forms three textural types. The first type, cpx1, is subhedral to anhedral, 200μm -5mm across, with irregular grain boundaries, a clear cleavage, and exolution lamellae. This type forms the porphyroclasts seen in Figur 4.4 and is interpreted to represent the remnants of a primary phase.

The second type, cpx2, is an aggregate of fibrous clinopyroxene intergrown with Fe-oxides (Figure 4.5b). Only a few aggregates of this type were discovered by optical microscopy. The fibrous clinopyroxene aggregates have either a tabular or diamond shaped outline.

The third type, cpx3, consists of small rounded grains usually <50μm across, that form thin bands along small serpentine filled shear zones.

Compositionally the three types are all diopside with low Na_2O content. The fibrous aggregates have well defined outlines and may have replaced a previous mineral, possibly orthopyroxene. Austrheim and Prestvik (2008), reported fibrous clinopyroxene

after orthopyroxene in the LOC as part of the rodingitization process. Alternatively the aggregates may represent replacement of olivine by clinopyroxene as reported by both Austrheim and Prestvik (2008); Iyer et al. (2008a) according to the reaction Ol + Ca $\longrightarrow$ Diop + Fe−oxide.

Serpentine is found in various textural settings: as veins with regular walls with widths from ∼1-30μm along grain boundaries, as vein fragments with needle-shaped grains perpendicular to former vein walls, and as interstitial serpentine. All these variations are shown in Figure 4.5.

Olivine is found as larger grains and as very fine fragments in serpentine filled fractures. It also constitutes the matrix mineral together with needle-shaped serpentine. The modal amount of olivine is estimated to less than 10%.

The forsterite content (Fo85) is the lowest analyzed of all the samples studied. Such low numbers (Fo<90) are common for magmatic olivine.

Chromite grains are randomly distributed. Their shapes vary from euhedral to anhedral.

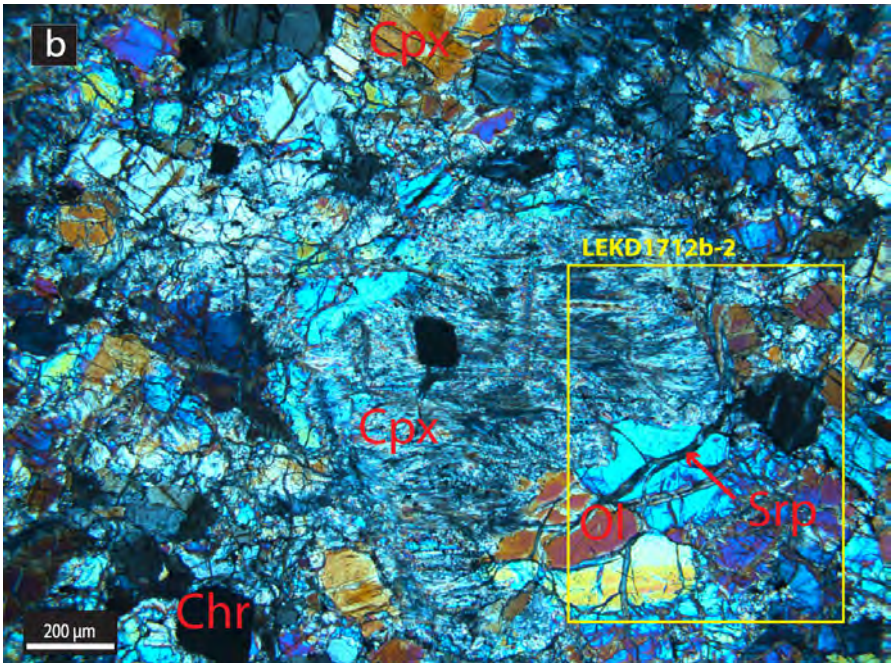

(a)

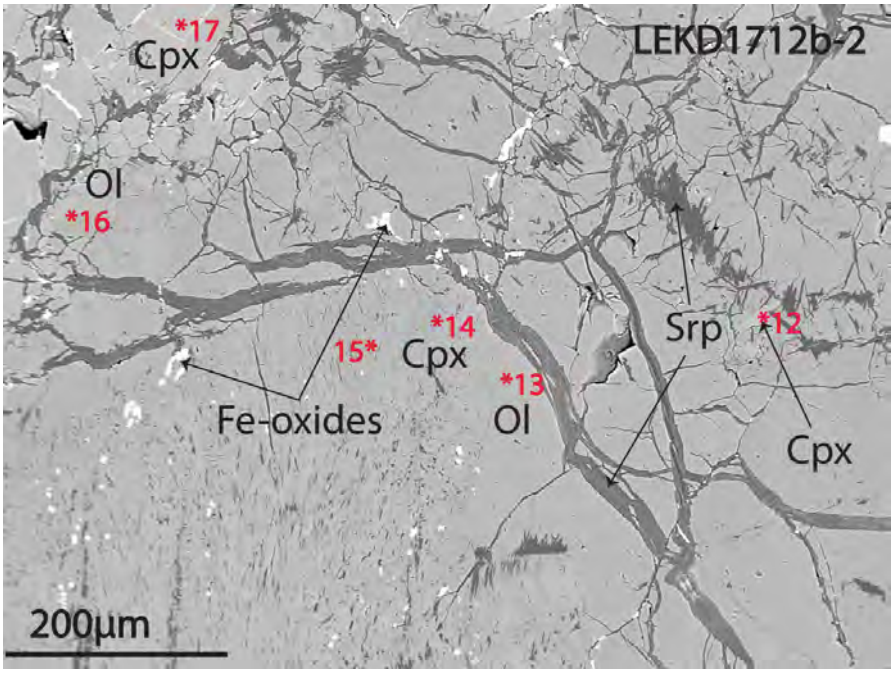

(b)

Figure 4.5: (a): Optical microphotograph of diamond shaped aggregates of fibrous clinopyroxene. An euhedral grain of chromite is enclosed within the fibrous clinopyroxene. The form suggest that the clinopyroxene aggregated, replaced a former mineral. (b): BSE image of the same fibrous aggregate. Relicts of olivine(Ol) suggest that the replaced phase is olivine. Note inclusions of oxides and serpentine in the fibrous aggregates and serpentinization of clinopyroxene. Red numbers show points for EMP analyses listed in tables 4.1 and 4.3. The BSE image is rotated 90° anti-clockwise compared to the optical microphotograph. Clinopyroxenite(2).

Chromite-rich clinopyroxenite(3), LEKD1412

This rock type (Figur 4.6) differs from the previously described clinopyroxenite(2) by containing a higher percentage of chromite (up to ~ 5 modal %) with a charactistic double corona of chlorite (Figure 4.7). It is suggested that the high chromite content gives this rock its dark weathering color. In addition to 90% clinopyroxene, and chromite with chlorite rims the rock contain minor olivine and serpentine.

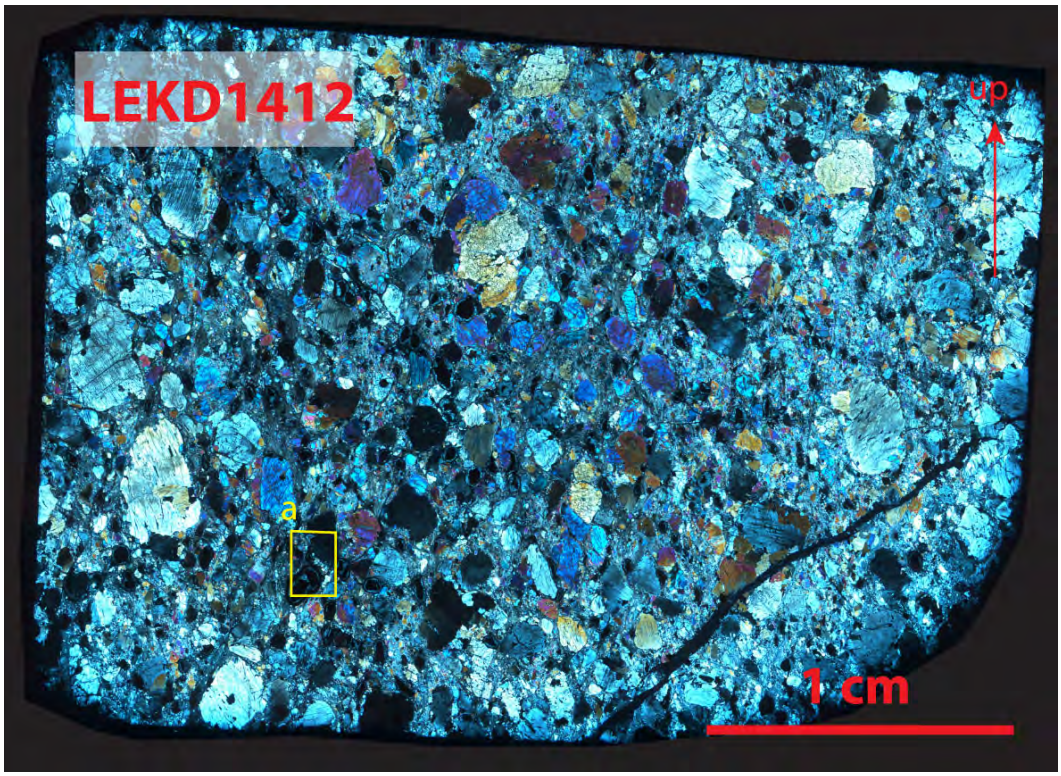

Figure 4.6: Photomerge of thinsection of the chromite-rich clinopyroxenite(3). Note the shape preferred orientation of clinopyroxene grains from upper left to lower right.

Clinopyroxenes with a relatively large grain size, 2-3 mm across, sit in a matrix of finer grained clinopyroxene giving the rock a porphyroclastic texture (Figure 4.6). The clinopyroxene has the composition of a diopside, but the porphyroclasts contain up to 2.6 wt% Al_2O_3 as compared to the matrix clinopyroxene where Al_2O_3 is down to 0.16 wt%.

Both the medium and coarse clinopyroxene grains have strain lamellea, undulose extinction and indented grain boundaries. A few grains are bent and locally faulted. Several grains are cor

A fibrous clinopyroxene(cpx2) occasionally intergrown with olivine make up aggregates with a size similar to the porphyroclastic clinopyroxene. The fibrous clinopyroxene is also diopsidic of composition. The medium to coarse grained porphyroclasts are interpreted to represent a primary clinopyroxene while the smaller matrix grain may represent recrystallized grains. Like for the clinopyroxenite the fibrous clinopyroxene intergrown with olivine is interpreted to form after another phase probably orthopyroxene.

The Mg# vary from 0.91 to 0.95. The low Mg# is correlated with the higher Al-content,

and may represent a primary characteristic.

Olivine(Fo87) appears scattered as fine grains, slightly larger than the very fine clinopyroxene grains constituting the matrix.

Serpentine is found in veins and as patches in reaction zones. Serpentine readily alters to chlorite and is also found mixed with chlorite in coronas around chromite (Figure 4.7).

Chromite is rimmed by two layered coronas. The innermost has bright bluish interference colors under XPL and consist of needle shaped chlorite grains. The outer corona is dark brown under XPL and almost isotropic. The grain boundaries disintegrate into the corona (Figure 4.7).

Chromite is the dominating Al-bearing phase in the ultramafic rocks studied. The core of the chromites show darker BSE-contrast indicating high Al-content. Similar chromites with chlorite rims are observed in wehrlite(4) sample LEKD1512 presented in the next subsection.

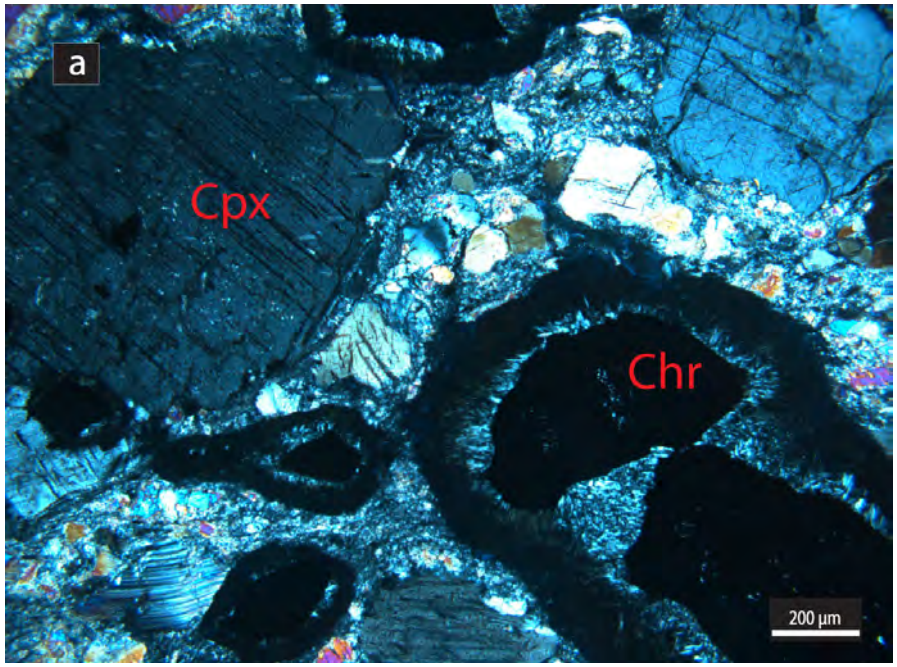

(a)

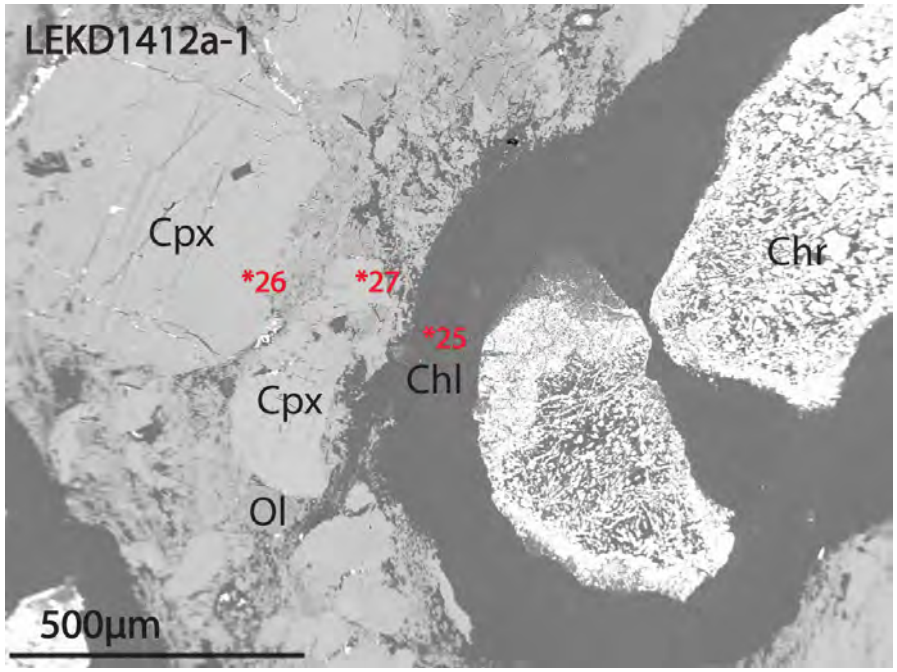

(b)

Figure 4.7: (a): Chromite with two layered corona. The innermost is chlorite, while the almost isotropic outer corona is chlorite intergrown with serpentine. Clinopyroxenes have cleavage and deformed twins, some slightly bent like the grain in the lower left corner. (b): Chromites display a darker high Al core surrounded by a brighter Fe- and Cr- rich rim. The clinopyroxenes adjacent to the chlorite rim are depleted in Al. e.g. Analysis no.27 yielded an Al_2O_3 of 0.82wt% compared to analysis no. 26 (2.64wt%) taken farther from the main reaction front. Red numbers show points for EMP analyses listed in tables 4.2 and 4.4. The BSE image is rotated 90° anti-clockwise compared to the optical microphotograph. Chromite-rich clinopyroxenite(3) at outcrop B.

Wehrlite(4), LEKD1512

The wehrlite (Figure 4.8) contains the minerals; olivine (Fo89-90), serpentine, clinopyroxene, Fe-oxides and chromite rimmed by a double chlorite corona. Minor Ni-sulphides were detected by EDS. The rock is moderately serpentinized, but displays particular textures suggesting extensive alteration and recrystallization as outlined below.

The modal estimates are: ∼75% olivine; ∼10-12% clinopyroxene; ∼15% serpentine; <1% chlorite and <1% chromite.

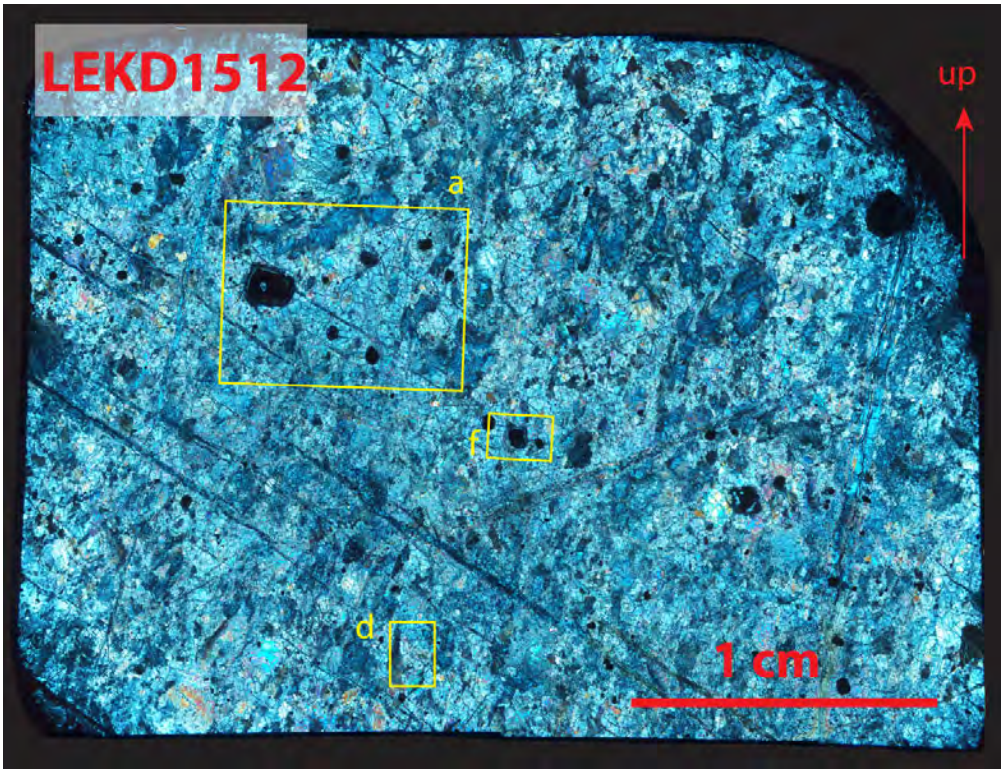

Figure 4.8: Photomerge of thinsection LEKD1512. Wehrlite(4).

Clinopyroxene. Two textural types of clinopyroxene is present. Grains, locally with undulose extinction and with exolution lamellae represent relicts after a primary clinopyroxene(cpx1). Cpx1 is subordinate to a fibrous clinopyroxene(cpx2) intergrown with olivine (Figure 4.9). The olivine-cpx2 intergrowths form domains with a size similar to a medium grained peridotite and suggest that these intergrowths are replacing a primary phase in the peridotite, probably orthopyroxene. Compositionally all clinopyroxene in the wehrlite are diopside with a low Na_2O. The highest content of Al_2O_3 (1.10 wt%) and Cr_2O_3 (0.19 wt%) was measured in cpx1, which also has the lowest Mg# (0.94).

Olivine displays a range of grain sizes varying from ∼ 10μm to 2mm in diameters. Larger grains with undulose extinction may be a part of a primary mineralogy. Olivine intergrown with clinopyroxene has an intermediate grain size (Figure 4.9b). Ultra-fine grained olivine is found in part of the section in domains enclosed with a marked fracture system (Figure 4.10a). These ultra-fine grained olivine domains locally contain coarser grained cores suggesting that they formed by recrystallization. The ultra-fine grained olivine is

typically developed in the vicinity of chromite grains with well developed chlorite rims (Figure 4.11). This may suggest that the olivine recrystallized in response to the corona growth.

Serpentine with a bluish interference color is present in the veins that enclose the domains of ultra-fine olivine and in larger veins that transect the rock. In such veins the serpentine fibers grow perpendicular to the wall.

Chlorite is found as rims around chromite grains. There is a significant Al-enrichment, and conversely, Fe-depletion towards the chromite (Figure 4.10b). In plain polar light both layers are either white or transparent, and the boundary between them is hard to establish. No pleochroism is observed in accordance with the Mg rich composition. Locally the chlorite rim around the chromite is lacking and the chromite is in contact with breccia zones consisting of olivine fragments (Figure 4.11). The change from a chlorite rim to a breccia zone occurs around the same grain. The formation of the breccia around the chromite suggest stress concentrations either related to force of crystallization for the growing chlorite or from external forces.

Chromite grains are fractured and veined by chlorite (Figure 4.11). Since chromite is the main Al-bearing phase in the wehrlite, it is assumed that the chlorite with up to 14 wt% Al_2O_3 formed by the following reaction between chromite and olivine:
$\text{olivine} + \text{Al}-\text{chromite} \longrightarrow \text{chlorite} + \text{chromite}$.

The recrystallization of the olivine to form ultrafine grains together with strong metasomatism indicated with intergrown olivine and clinopyroxene suggests that this rock strongly altered and preserved little of its original textures and mineralogy.

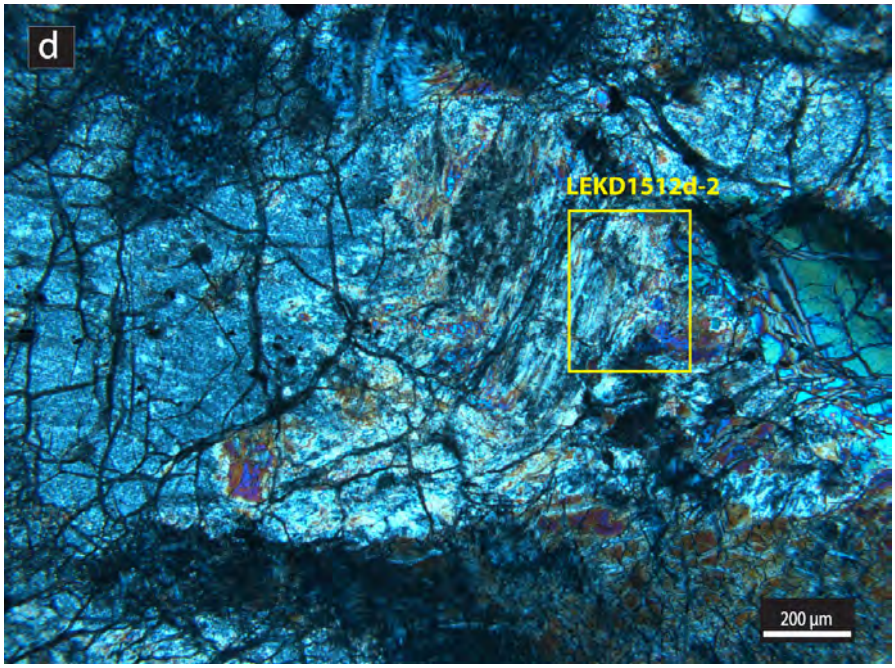

(a)

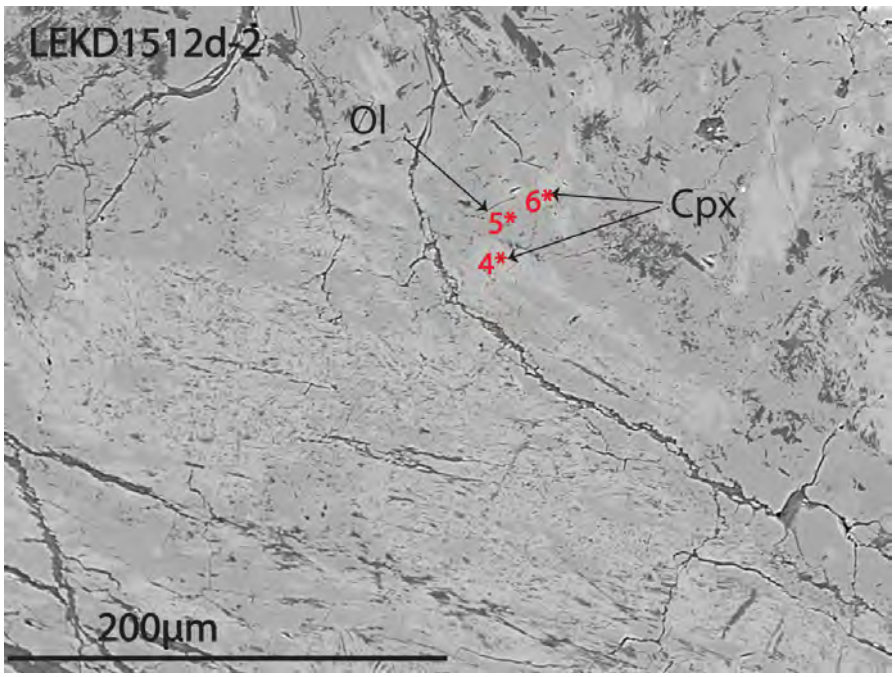

(b)

Figure 4.9: Fibrous grain growth with intergrown olivine and clinopyroxene(cpx2). Red numbers show points for EMP analyses listed in tables 4.1 and 4.3. The BSE image is rotated 90° anti-clockwise compared to the optical microphotograph. Wehrlite(4), at outcrop B.

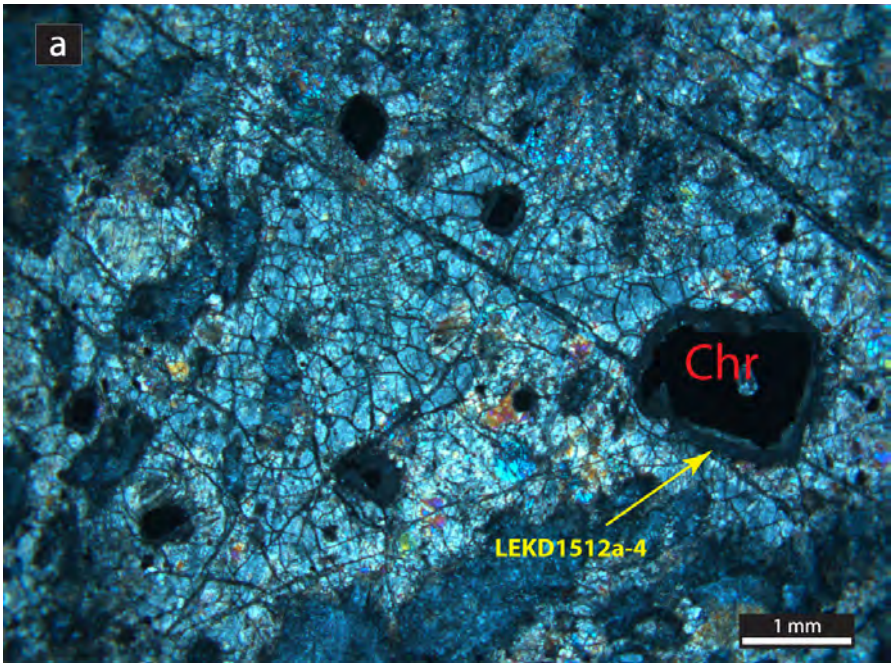

(a)

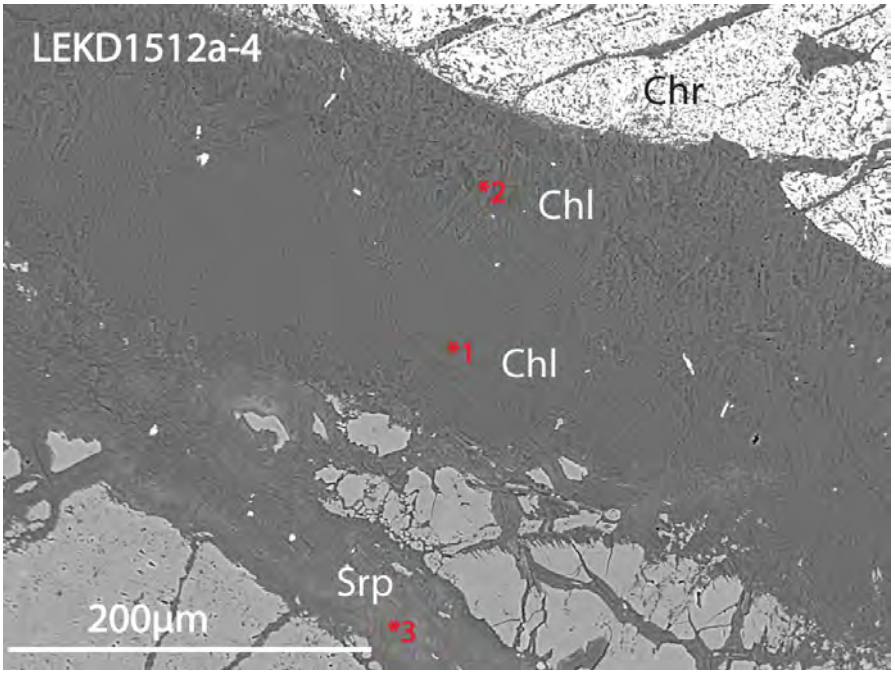

(b)

Figure 4.10: (a): Ultrafine grains of recrystallized olivine surround chromites. Ultrafine grained olivine are grouped within small domains separated by fractures in remarkable pattern. (b): Analysis no.1 yielded an Al_2O_3 of 10.99 wt%, while no.2 yielded 14.18 wt%. Red numbers show points for EMP analyses listed in table 4.4. Optical microphotographs and BSE images, wehrlite(4), at outcrop B.

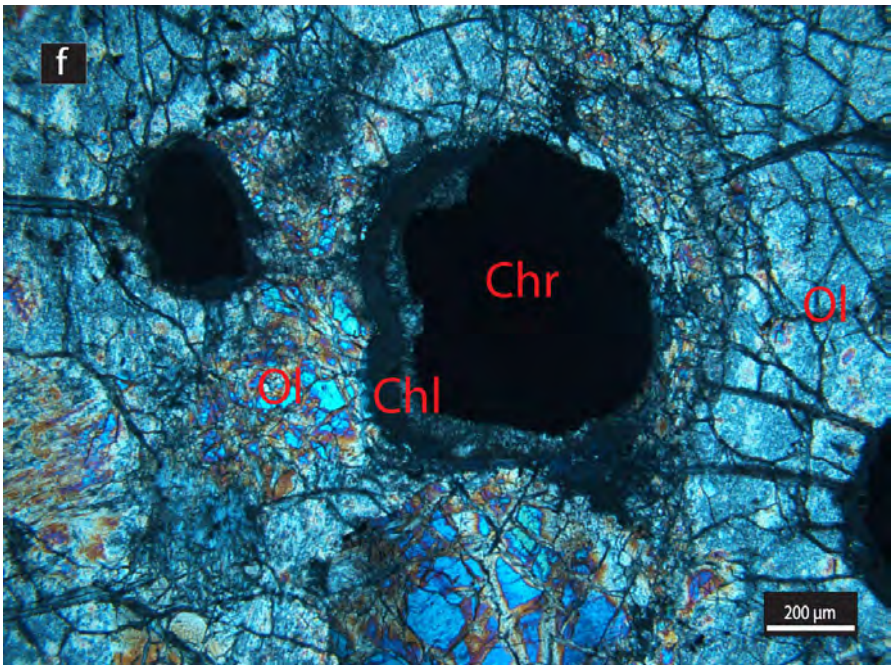

Figure 4.11: Most chromites in this sample have double coronas. Around the grain in the center of this microphotograph the double corona on the left side give way to a zone of brecciated olivine on the right hand side of the grain. The brecciation was likely reaction induced and a result of volume increase imposing local stresses upon the surrounding olivine. Note also that the chromites are inter-connected through serpentine veins. Wehrlite(4) at outcrop B.

Unit of alternating dunite and clinopyroxenite(5), LEKD1112

The clinopyroxenites of the alternating layers display domains of extensive deformation with bands of cataclastic grains of olivine and clinopyroxene in a matrix of serpentine (Figure 4.12).

The modal estimates are: ∼45-47% clinopyroxene; ∼40-45% serpentine; < 5% olivine; and ∼1-3% chromite.

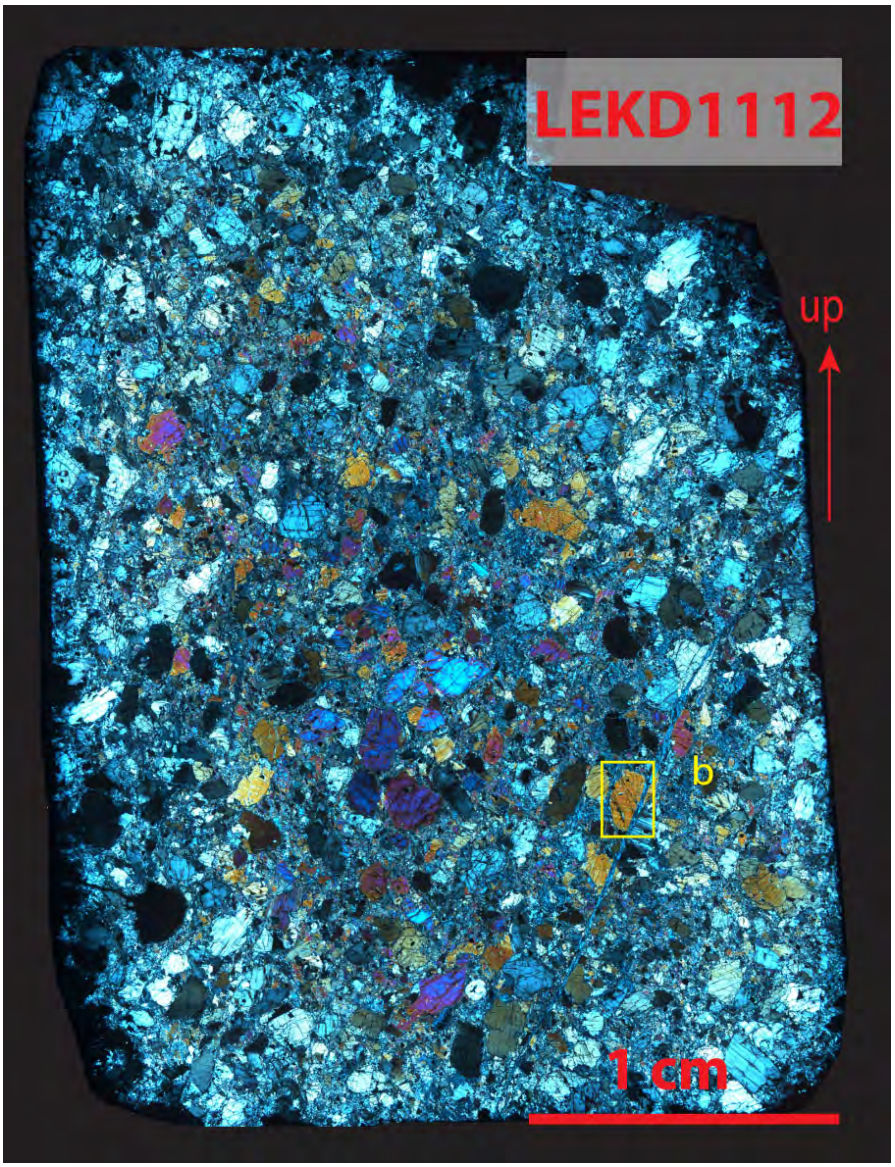

Figure 4.12: Photomerge of thinsection of clinopyroxenite(5) with porphyroclastic texture from the unit of alternating dunite and clinopyroxenite layers.

Clinopyroxenes with a diameter up to 2 mm show strain in form of undulose extinction. Like all the studied lithologies clinopyroxene is serpentinized (Figure 4.13). The replacement of clinopyroxene by serpentine provides Ca for growth of fibrous clinopyroxene(cpx2). The clinopyroxenes are all of diopsidic composition.

Serpentine appears as both veins with needle shaped grains of different gray interference colors and as domains covering areas at the size of up to 1 mm. The serpentine veins are straight and occasionally cross-cuts clinopyroxene.

One analysis (no.37- Figure 4.13b) of needle-shaped serpentine yielded a FeO content of 6.23 wt%, almost twice as much as the other two analyses. As for other Fe-rich serpentine the total was quite low with 82.87 wt%.

Olivine. There are only minor amounts of olivine (Fo87-88). Grains are anhedral and the outline of the original grain is not longer visible. Some analyses show remarkably low totals. The EMP was controlled, and the likely cause for these low totals is the presence of water.

Chromite grains are anhedral to subhedral and are randomly distributed.

Fe-oxides (magnetite?) occur as irregular trails following zones of very fine grained material. They are also found as micrograins in clinopyroxene crystals.

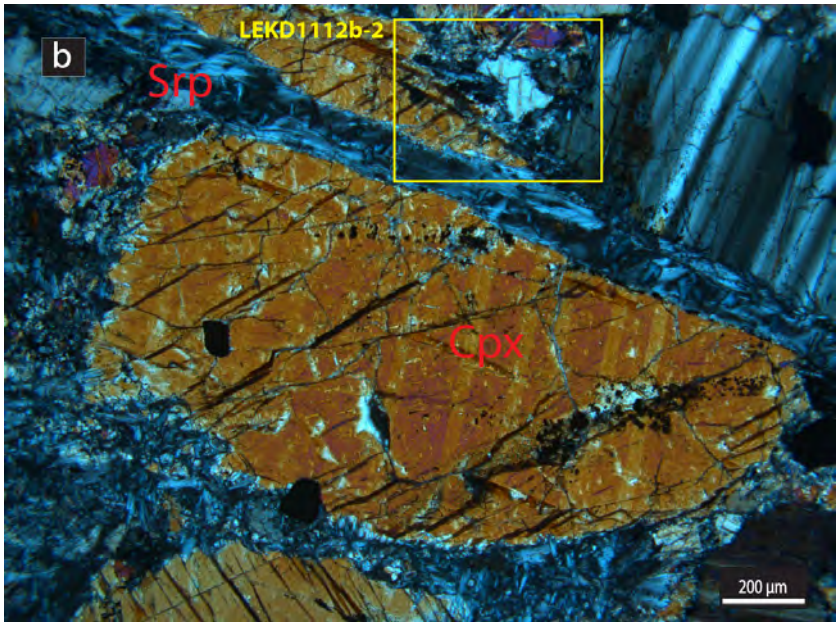

(a)

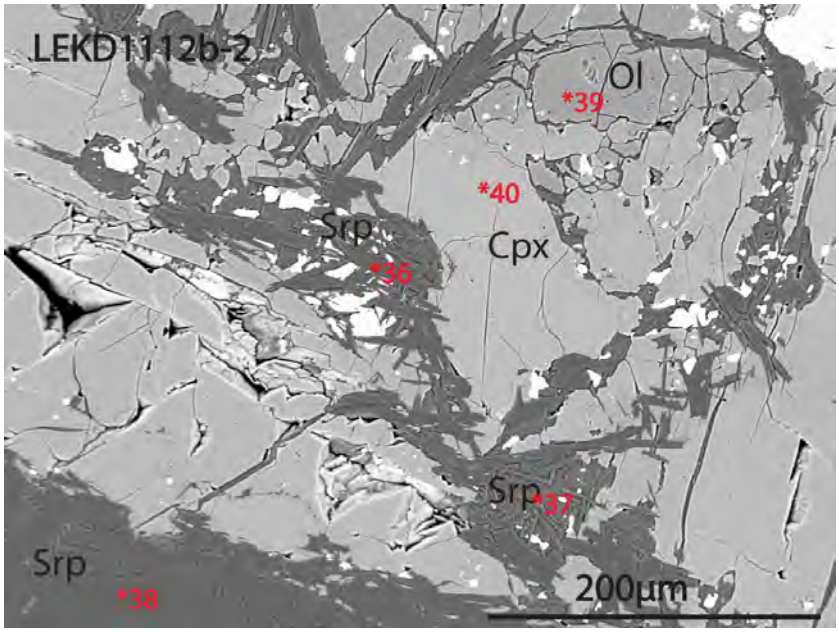

(b)

Figure 4.13: (a): Fragments of a large clinopyroxene has been displaced relative to each other (sinistral shear sense) by a serpentine filled fault. The larger grain display exolution lamellae, while the grain in the upper right corner show strain lamellae. (b): The clinopyroxene(cpx1), is replaced by needles of serpentine. Red numbers in BSE image show points for EMP analyses listed in tables 4.1, 4.2 and 4.4. The optical microphotograph is rotated 90° clockwise compared to thinsection LEKD1112.

Sample: LEKD	1112	1112	1112	1112	1412	1412	1512	1512	1512	1512	1712	1712
Analysis #	33	34	39	41	18	30	5	9	10	11	13	16
Mineral	Ol	Ol	Ol	Ol	Ol	Ol	Ol	Ol	Ol	Ol	Ol	Ol
Comment	AC(5)	AC(5)	AC(5)	AC(5)	CRC(3)	CRC(3)	W(4)	W(4)	W(4)	W(4)	C(2)	C(2)
[wt.%]												
SiO_2	39,19	39,96	39,27	39,69	40,26	39,91	39,95	39,40	40,26	40,31	40,14	40,00
TiO_2	n.d.	n.d.	n.d.	n.d.	n.d.	n.d.	n.d.	0,02	0,02	0,02	n.d.	0,02
Al_2O_3	n.d.	0,01	0,02	n.d.	n.d.	n.d.	n.d.	0,02	n.d.	n.d.	0,02	n.d.
Cr_2O_3	n.d.	n.d.	0,04	n.d.	n.d.	n.d.	n.d.	n.d.	0,02	n.d.	n.d.	n.d.
FeO(tot)	12,32	12,48	12,22	11,75	12,61	12,35	10,95	10,41	9,49	10,88	14,15	14,14
NiO	0,22	0,12	0,10	0,15	0,14	0,20	0,33	0,41	0,47	0,30	0,16	0,12
MgO	46,53	47,03	46,97	46,53	47,19	47,38	48,11	48,41	49,77	48,64	45,47	46,03
MnO	0,25	0,31	0,26	0,31	0,30	0,22	0,18	0,21	0,21	0,21	0,28	0,33
CaO	n.d.	0,08	0,08	0,03	n.d.	0,03	0,03	0,10	n.d.	0,06	n.d.	0,16
Na_2O	n.d.	n.d.	n.d.	n.d.	n.d.	n.d.	n.d.	0,01	n.d.	n.d.	n.d.	n.d.
K_2O	n.d.	0,01	n.d.	n.d.	0,01	n.d.	n.d.	n.d.	n.d.	n.d.	n.d.	n.d.
Total	98,51	99,99	98,95	98,47	100,50	100,09	99,55	98,99	100,24	100,45	100,21	100,79
Si	0,989	0,993	0,986	0,999	0,995	0,991	0,991	0,983	0,986	0,991	1,002	0,994
Ti	n.d.	n.d.	n.d.	n.d.	n.d.	n.d.	n.d.	n.c.	n.c.	n.c.	n.d.	n.c.
Al	n.d.	n.c.	0,001	n.d.	n.d.	n.d.	n.d.	n.c.	n.d.	n.d.	n.c.	n.d.
Cr	n.d.	n.d.	0,001	n.d.	n.d.	n.d.	n.d.	n.d.	n.c.	0,001	n.d.	n.d.
Fe	0,260	0,259	0,257	0,247	0,261	0,256	0,227	0,217	0,194	0,223	0,295	0,294
Ni	0,004	0,002	0,002	0,003	0,003	0,004	0,007	0,008	0,009	0,006	0,003	0,002
Mg	1,751	1,743	1,759	1,745	1,739	1,753	1,779	1,800	1,818	1,782	1,692	1,705
Mn	0,005	0,006	0,006	0,007	0,006	0,005	0,004	0,005	0,004	0,004	0,006	0,007
Ca	n.d.	0,002	0,002	0,001	n.d.	0,001	0,001	0,003	n.d.	0,002	n.d.	0,004
Na	n.d.	n.d.	n.d.	n.d.	n.d.	n.d.	n.d.	n.c.	n.d.	n.d.	n.d.	n.d.
K	n.d.	n.c.	n.d.	n.d.	0,000	n.d.	n.d.	n.d.	n.d.	n.d.	n.d.	n.d.
Total	3,011	3,007	3,013	3,001	3,005	3,009	3,009	3,017	3,013	3,009	2,998	3,006
Mg/(Mg+Fe)	0,87	0,87	0,87	0,88	0,87	0,87	0,89	0,89	0,90	0,89	0,85	0,85

Table 4.1: Analyses of olivine, part 7. Sorted by increasing sample numbers. C(2) = clinopyroxenite, CRC(3) = chromite-rich clinopyroxenite, W(4) = wehrlite, AC(5) = unit of alternating dunite and clinopyroxenite, n.d. = not detected, n.c. = not calculated. Calculated on 4 oxygens.

Sample: LEKD	1112	1112	1112	1412	1412	1412	1412	1412	1412	1412	1412	1412	1412
Analysis #	32	35	40	19	20	21	22	23	24	26	27	28	29
Mineral	Cpx1	Cpx1	Cpx1	Cpx3	Cpx1	Cpx1	Cpx1	Cpx2	Cpx2	Cpx1	Cpx2	Cpx2	Cpx1
Comment	AC(5)	AC(5)	AC(5)	CRC(3)	CRC(3)	CRC(3)	CRC(3)	CRC(3) IG	CRC(3) IG	CRC(3)	CRC(3) IG	CRC(3) IG	CRC(3)
SiO_2	53,96	53,93	54,57	54,74	54,01	55,09	53,23	54,34	54,46	52,23	53,58	53,83	52,68
TiO_2	0,05	0,00	0,06	0,02	0,04	0,03	0,14	0,09	0,09	0,09	0,06	0,05	0,14
Al_2O_3	0,88	0,49	0,27	0,16	0,92	0,45	2,54	1,20	1,25	2,64	0,82	0,95	2,55
Cr_2O_3	0,37	0,13	0,04	0,00	0,07	0,05	0,19	0,16	0,16	0,17	0,05	0,04	0,33
FeO(tot)	2,43	2,40	1,76	1,82	2,36	2,11	2,54	1,95	2,15	2,87	2,26	2,39	2,53
MnO	0,16	0,12	0,09	0,13	0,10	0,03	0,08	0,07	0,14	0,06	0,09	0,17	0,05
MgO	17,58	17,85	17,72	17,98	17,53	18,08	16,87	17,39	17,42	17,09	17,53	17,70	16,68
NiO	0,00	0,01	0,00	0,00	0,00	0,05	0,05	0,00	0,01	0,03	0,00	0,01	0,02
CaO	24,56	24,91	26,01	25,71	25,50	25,21	25,10	25,53	25,04	24,80	25,27	25,51	25,40
Na_2O	0,11	0,09	0,07	0,09	0,00	0,01	0,07	0,07	0,00	0,04	0,02	0,03	0,04
K_2O	0,00	0,01	0,01	0,00	0,00	0,00	0,02	0,00	0,00	0,01	0,00	0,00	0,00
SUM	100,07	99,93	100,59	100,66	100,53	101,11	100,82	100,79	100,74	100,02	99,68	100,69	100,44
mg#	92,8	93,0	94,7	94,6	93,0	93,9	92,2	94,1	93,5	91,4	93,3	92,9	92,2
Si	1,959	1,958	1,968	1,971	1,952	1,977	1,920	1,958	1,965	1,897	1,951	1,941	1,909
Al IV	0,038	0,021	0,011	0,007	0,039	0,019	0,080	0,042	0,035	0,103	0,035	0,040	0,091
Al VI	0,000	0,000	0,000	0,000	0,000	0,000	0,028	0,008	0,018	0,010	0,000	0,000	0,018
Ti	0,001	0,000	0,002	0,001	0,001	0,001	0,004	0,003	0,003	0,003	0,002	0,001	0,004
Cr	0,010	0,004	0,001	0,000	0,002	0,001	0,005	0,004	0,004	0,005	0,001	0,001	0,010
Fe3+	0,020	0,033	0,027	0,028	0,027	0,013	0,022	0,015	0,003	0,043	0,030	0,038	0,029
Fe2+	0,054	0,040	0,026	0,026	0,045	0,051	0,055	0,044	0,061	0,044	0,039	0,034	0,047
Mn	0,005	0,004	0,003	0,004	0,003	0,001	0,003	0,002	0,004	0,002	0,003	0,005	0,002
Mg	0,951	0,966	0,952	0,965	0,944	0,967	0,907	0,934	0,937	0,925	0,952	0,951	0,901
Ni	0,000	0,000	0,000	0,000	0,000	0,002	0,001	0,000	0,000	0,001	0,000	0,000	0,001
Ca	0,955	0,969	1,005	0,992	0,987	0,969	0,970	0,985	0,968	0,965	0,986	0,985	0,986
Na	0,007	0,006	0,005	0,006	0,000	0,001	0,005	0,005	0,000	0,003	0,002	0,002	0,003
ox	5,980	5,967	5,973	5,972	5,973	5,987	5,978	5,985	5,997	5,957	5,970	5,962	5,971
Al total	0,038	0,021	0,011	0,007	0,039	0,019	0,108	0,051	0,053	0,113	0,035	0,040	0,109
Fe tot	0,074	0,073	0,053	0,055	0,071	0,063	0,077	0,059	0,065	0,087	0,069	0,072	0,077
Fe3+	0,020	0,033	0,027	0,028	0,027	0,013	0,022	0,015	0,003	0,043	0,030	0,038	0,029
Di+Hd	0,914	0,944	0,992	0,982	0,946	0,950	0,891	0,943	0,931	0,862	0,949	0,941	0,897
En+Fs	0,046	0,031	-0,007	0,005	0,021	0,034	0,035	0,017	0,034	0,053	0,021	0,022	0,026

Table 4.2: Analyses of clinopyroxene - the layered sequence. CRC(3) = chromite-rich clinopyroxenite, AC(5) = unit of alternating dunite and clinopyroxenite layers. Sorted by increasing sample numbers. Structural formula according to Neumann (1976)

Sample: LEKD	1512	1512	1512	1512	1712	1712	1712	1712
Analysis #	4	6	7	8	14	15	12	17
Mineral	Cpx2	Cpx2	Cpx1	Cpx2	Cpx2	Cpx2	Cpx3	Cpx1
Comment	W(4) Fibrous	W(4) Fibrous	W(4)	W(4) Fibrous	C(2) Fibrous	C(2) Fibrous	C(2)	C(2)
[wt.%]								
SiO_2	53,79	53,19	54,24	53,98	54,24	53,79	53,19	53,98
TiO_2	0,01	0,03	0,06	0,00	0,06	0,01	0,03	0,00
Al_2O_3	0,11	0,27	1,10	0,27	1,10	0,11	0,27	0,27
Cr_2O_3	0,01	0,02	0,19	0,04	0,19	0,01	0,02	0,04
FeO(tot)	1,44	1,80	1,88	1,23	1,88	1,44	1,80	1,23
MnO	0,02	0,07	0,05	0,04	0,05	0,02	0,07	0,04
MgO	19,25	19,49	17,93	18,21	17,93	19,25	19,49	18,21
NiO	0,01	0,05	0,04	0,03	0,04	0,01	0,05	0,03
CaO	25,03	24,23	24,91	25,63	24,91	25,03	24,23	25,63
Na_2O	0,04	0,12	0,09	0,15	0,09	0,04	0,12	0,15
K_2O	0,00	0,00	0,00	0,02	0,00	0,00	0,00	0,02
SUM	99,71	99,26	100,50	99,58	100,50	99,71	99,26	99,58
mg#	96,0	95,1	94,4	96,4	94,4	96,0	95,1	96,4
Si	1,943	1,927	1,955	1,957	1,955	1,943	1,927	1,957
Al IV	0,005	0,012	0,045	0,012	0,045	0,005	0,012	0,012
Al VI	0,000	0,000	0,002	0,000	0,002	0,000	0,000	0,000
Ti	0,000	0,001	0,002	0,000	0,002	0,000	0,001	0,000
Cr	0,000	0,001	0,005	0,001	0,005	0,000	0,001	0,001
Fe3+	0,043	0,054	0,021	0,037	0,021	0,043	0,054	0,037
Fe2+	0,000	0,000	0,036	0,000	0,036	0,000	0,000	0,000
Mn	0,001	0,002	0,002	0,001	0,002	0,001	0,002	0,001
Mg	1,036	1,053	0,963	0,984	0,963	1,036	1,053	0,984
Ni	0,000	0,001	0,001	0,001	0,001	0,000	0,001	0,001
Ca	0,968	0,941	0,962	0,996	0,962	0,968	0,941	0,996
Na	0,003	0,009	0,007	0,011	0,007	0,003	0,009	0,011
ox	5,944	5,930	5,979	5,958	5,979	5,944	5,930	5,958
Al total	0,005	0,012	0,047	0,012	0,047	0,005	0,012	0,012
Fe tot	0,043	0,054	0,057	0,037	0,057	0,043	0,054	0,037
Fe3+	0,056	0,070	0,021	0,042	0,021	0,056	0,070	0,042
Di+Hd	0,963	0,928	0,917	0,983	0,917	0,963	0,928	0,983
En+Fs	0,037	0,063	0,041	0,001	0,041	0,037	0,063	0,001

Table 4.3: Analyses of clinopyroxene - the layered sequence (cont.). C(2) = clinopyroxenite, W(4) = wehrlite. Sorted by increasing sample numbers. Structural formula according to Neumann (1976)

Sample: LEKD	1112	1112	1112	1512	0311	0411	1412	1512	1512
Analysis #	36	37	38	3	18	21	25	1	2
Mineral	Srp	Srp	Srp	Srp	Chl	Chl	Chl	Chl	Chl
Comment	AC(5)	AC(5)	AC(5)	W(4)	AH	D1	CRC(3)	W(4)	W(4)
[wt.%]									
SiO_2	42,78	38,25	43,39	34,37	34,68	35,45	34,25	35,27	32,60
TiO_2	0,01	0,01	n.d.	0,01	n.d.	0,01	n.d.	n.d.	0,01
Al_2O_3	1,24	0,06	1,16	0,28	10,08	10,55	12,97	10,99	14,18
Cr_2O_3	0,23	0,02	0,23	0,05	3,56	4,00	0,62	1,07	0,58
FeO(tot)	3,68	6,23	3,14	7,20	3,10	2,69	3,91	2,98	3,85
NiO	0,09	0,03	0,06	0,25	0,23	0,16	0,07	0,06	0,12
MgO	38,57	38,08	39,28	39,72	35,88	36,24	34,87	35,51	33,71
MnO	0,07	0,12	0,05	0,22	0,01	0,02	0,01	n.d.	0,04
CaO	0,17	0,05	0,02	0,14	n.d.	0,04	0,04	0,04	0,01
Na_2O	n.d.	0,01	n.d.	n.d.	0,03	0,06	0,03	0,01	0,04
K_2O	n.d.	n.d.	n.d.	n.d.	0,01	0,02	0,01	0,01	0,01
Total	86,86	82,87	87,32	82,23	87,57	89,23	86,78	85,94	85,14
Si	2,010	1,929	2,020	1,781	6,574	6,581	6,498	6,729	6,311
Ti	n.c.	n.c.	n.d.	n.c.	n.d.	0,001	n.d.	n.d	0,001
Al	0,069	0,004	0,064	0,017	2,252	2,308	2,901	2,471	3,235
Cr	0,009	0,001	0,008	0,002	0,533	0,587	0,093	0,161	0,090
Fe	0,145	0,263	0,122	0,312	0,491	0,417	0,621	0,475	0,623
Ni	0,004	0,001	0,002	0,011	0,035	0,024	0,011	0,009	0,018
Mg	2,702	2,863	2,725	3,069	10,141	10,028	9,865	10,099	9,730
Mn	0,003	0,005	0,002	0,009	0,001	0,003	0,001	n.d	0,007
Ca	0,008	0,003	0,001	0,008	n.d.	0,008	0,008	0,007	0,002
Na	n.d.	0,001	n.d.	n.d.	0,012	0,020	0,009	0,005	0,015
K	n.d.	n.d.	n.d.	n.d.	0,002	0,006	0,003	0,003	0,004
Total	4,950	5,069	4,944	5,209	20,041	19,983	20,011	19,959	20,035
Mg/(Mg+Fe)	0,95	0,92	0,96	0,91	0,95	0,96	0,94	0,96	0,94

Table 4.4: Analyses of serpentine, part 2 and chlorite. D = domain, AH = alteration halo, CRC(3) = chromite-rich clinopyroxenite, W(4) = wehrlite, AC(5) = small scale alternation of dunite and clinopyroxenite, sorted by increasing sample numbers. n.d. = not detected, n.c. = not calculated. Serpentine calculated on 7 oxygens, chlorite calculated on 28 oxygens.

4.3 Petrography of deformation zones at outcrop A and B

As outlined in the field relation section (section 2.2.5) and shown on the map (Figure 2.3), the area is transected by faults and shear zones.

The observed deformation zones were previously categorized into the following three categories determined by their appearance in the field.

- Mylonite and larger damage zones
- Matrix or clast supported deformation/breccia zones
- Small-scale (network of) fractures with alteration zones

In this section I present the microtexture and the mineral chemistry from these high strain zones, from both outcrop A and B. The location of the investigated samples are shown on Figure 4.14 (outcrop A) and Figure 4.28 (outcrop B).

4.3.1 Outcrop A

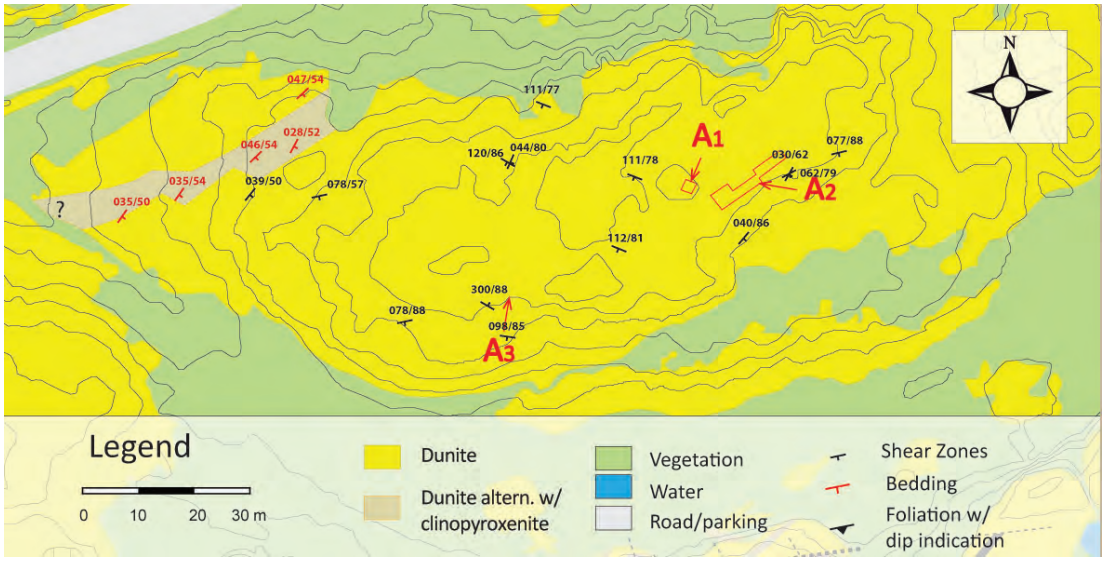

Figure 4.14: Detail of map show locality A where two deformation zones were mapped in detail (A1, A2). For the complete map please refer to Figure 2.3

Small-scale fractures with yellow alteration rims

Sample **LEKD0311** (Figure 4.15) was cored from a deformation zone with alteration halos as shown in Figure 2.22a. The zone is ca 0.3 cm across. The drill site is located ca 25 cm from a major breccia zone at subsite A1 (Figure 4.14), which was mapped in detail (Figure 2.21).

A photomerge of the thinsection placed perpendicular to the deformation zone is shown in Figure 4.15a. The central deformation zone with its alteration halos runs from the upper left to the lower right part of Figure 4.15a.

The small-scale alteration zone
The yellow alteration halos are developed around a central microshear zone filled with serpentine and olivine grains. The yellow alteration halos consist of fine grained olivine surrounded by serpentine veins. A marked reduction in the olivine grains outward in the alteration halos is evident and the outer dark rim seen in the field consists of ultra-fine grained olivine (Figure 4.15b).

The wall rock display a marked fracture pattern slightly oblique to the deformation zone. Whether this fracture pattern is related to the fine web of thin serpentine veins displayed at the surface (Figure 2.22a) or is a relict of a pervasive serpentine foliation is not clear. The fractures are still filled with serpentine and have a few olivine grains with their long dimension oriented parallel to the fracture wall (Figure 4.18). Vein borders are decorated with larger olivine grains (Figure 4.18). The texture of the wall rock is characterized by small ($\sim$10-50μm) olivine grains surrounded by thin ($\sim$1-5μm) serpentine veins. Locally aggregates of slightly larger olivine grains with undulose extinction can be seen.

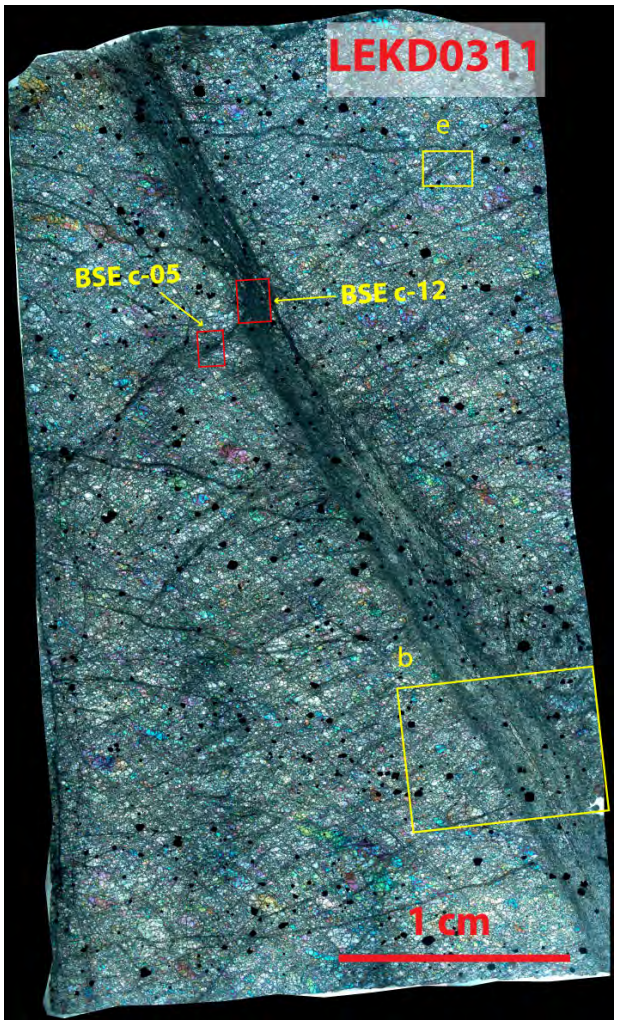

(a)

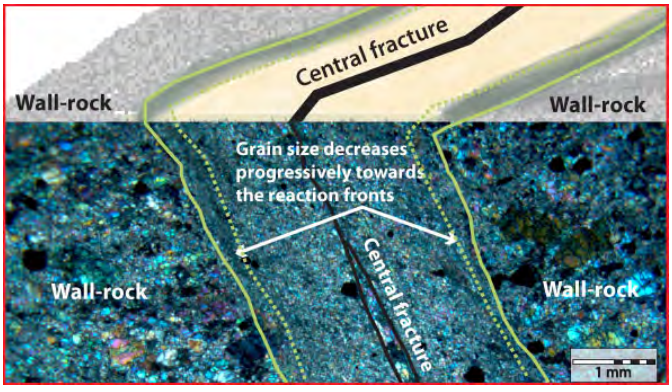

(b)

Figure 4.15: (a): Photomerge of thinsection, subsite A1 showing the fracture with the yellow alteration halos and its wall rock. (b): The combined drawing and microphotograph shows the relationship between small-scale fractures with alteration zones as seen in the field, and the texture revealed by optical micrography. Locally the central fracture, which is filled with interstitial serpentine, contains somewhat larger ($<100\mu$m) olivine grains. The reaction fronts propagate perpendicularly from the central fracture and outwards. The reaction front is a serpentinization front recognized by both an increased amount of serpentine as well as increased fragmentation of olivine grains. The intense grain size reduction at the reaction front gives the abrupt dark gray border between the alteration zone and the wall-rock as seen in the field.

LEKD0311

Olivines(Fo92-94) in the wall rock occur as large and intermediate sized porphyroclasts (50μm-250μm) and as fine (10-50μm) to ultra-fine (<10μm) clasts. Porphyroclasts display typical olivine fracturing, subgrain boundaries and undulose extinction (Figure 4.18). Some larger clasts are stretched (shape preferred orientation), which together with undulose extinction are indicative for intracrystalline deformation and dynamic recrystallization (Passchier and Trouw, 2005). Dungan (1977) observed olivine nucleation along vein margins, which may be analogue to our observations of mineral growth along serpentine veins. If the growth of olivine is caused by dehydration then the following reaction suggested by the same author might be applicable: antigorite + brucite $\longrightarrow$ forsterite + H_2O.

Serpentine make up the interstitial matrix mineral. This applies to all samples from outcrop A presented in this subsection. In the wall rock serpentine also occur in thin veins and as scattered needle-shaped grains in the marked fracture pattern. The latter might be relicts of a former serpentine network, possibly a part of the pervasive foliation observed locally in the field. The FeO content of serpentine in the central fracture is about 2 wt%. The average for analyses from wall rock veins is ~3.8%, but vary from 2.05wt% to 6.47wt%.

Clinopyroxenes are all diopsides and are found in bands following serpentine veins in the wall rock (Figure 4.17a) or at reaction fronts (Figure 4.17b). Within the alteration zone clinopyroxene bands or single grains are also intergrown with olivine at grain boundaries. This clinopyroxene(cpx3) can be distinguished by their textural type as well as by their low or no Al_2O_3, and higher CaO content. Austrheim and Prestvik (2008) suggested that this type of clinopyroxene (referred to as cpx3 in this thesis) replaced cpx1(primary clinopyroxene) during Ca-metasomatism following Ca-releasing breakdown of cpx1. Cpx1 (primary clinopyroxene) and cpx2 (fibrous clinopyroxene) have not been observed in this sample, which may indicate transport of CaO along the deformation zone.

Chromite. Some grains show strong and sharp compositional zonation from a chromite core via chromian magnetite inner rim (Fe-rich and Al-depleted) to magnetite outer rim. Such grains have rugged non-idiomorphic grain boundaries (Figure 4.16c). Chromite readily modifies during prograde metamorphism following hydration. At elevated temperatures (above 550°) chromite will be subjected to Al-depletion (Barnes, 2000). The same author suggest that the composition at the chromite-magnetite boundary may be indicative for metamorphic grade.

The petrography of the small scale fractures and their alteration zones observed in the field (Figure 4.15b) represent intense deformation zones where the grain size of olivine is strongly reduced, where the serpentinzation increases, and where transport of Ca occur as indicated by the bands of the diopsidic clinopyroxene(cpx3) (Figure 4.17b).

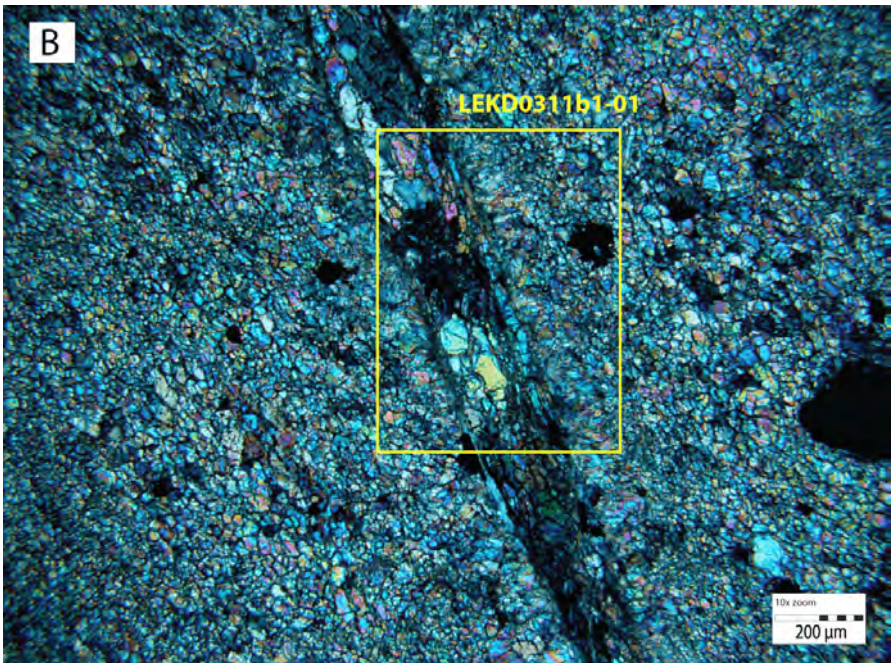

(a) Central fracture with alteration halos. Dynamically recrystallized olivine in a matrix of serpentine.

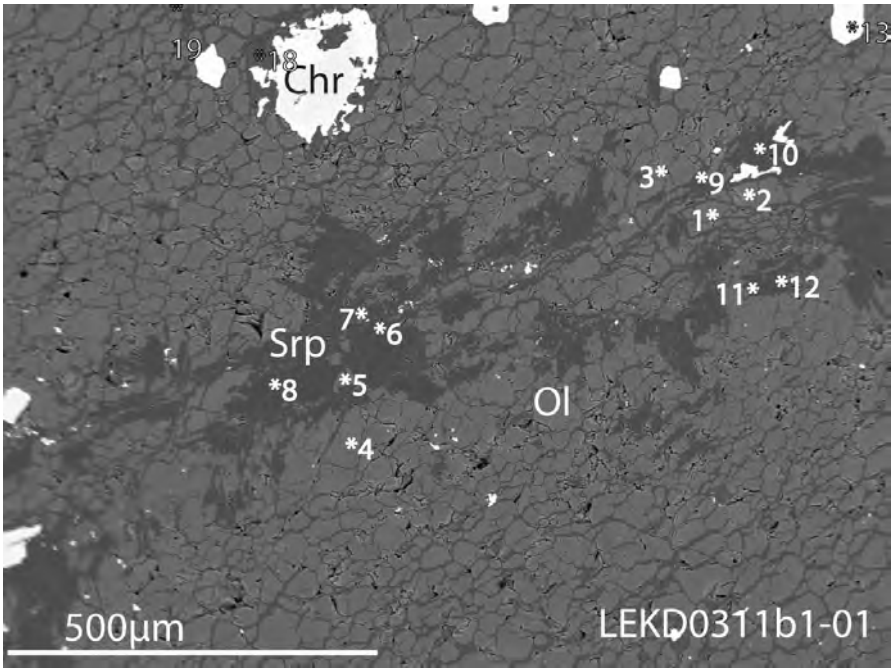

(b) BSE image of central fracture - outlined in microphotograph above.

Figure 4.16: (a): The microphotograph show growth of olivine in the sharply defined central domain of the mylonitic alteration halos. The growth of olivine is stronger along the shear fracture(s) in the center of the microphotograph. The illustration shows to the central fracture with alteration halos depicted in Figure 4.15. The elongated grain shape is encourage by the bounding vein walls. (b): Olivines grow from the rims inward of a former serpentine vein. Patches of serpentine remain in the central domain. Also note the non-idiomorphic grain boundary of the chromite grain. This grain is displayed in Figure 4.16c below. White numbers show points for EMP analyses listed in tables 4.5 and 4.11. The BSE image is rotated 90° anti-clockwise compared to the optical microphotograph.

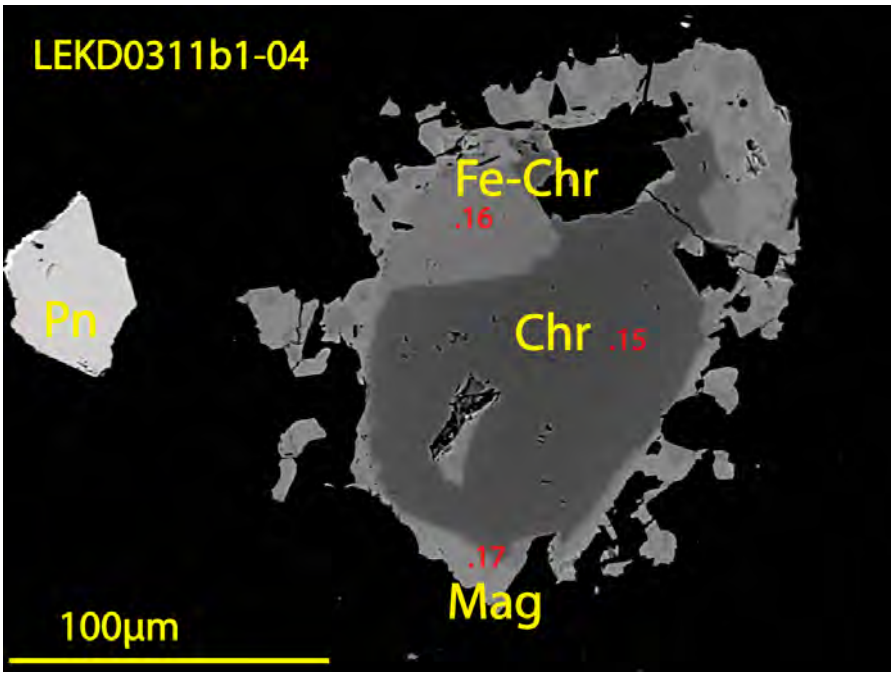

(c) BSE close up of chromite grain in (b).

Figure 4.16: Chromite/chromian magnetite grain. Example of strong zonation of chromite with Fe enrichment towards the rim, which is non-idiomorphic. Note the sharp boundaries. Pn denotes pentlandite. Red numbers show points for EMP analyses listed in table 4.13. The BSE image is rotated 90° anti-clockwise compared to the optical microphotograph.

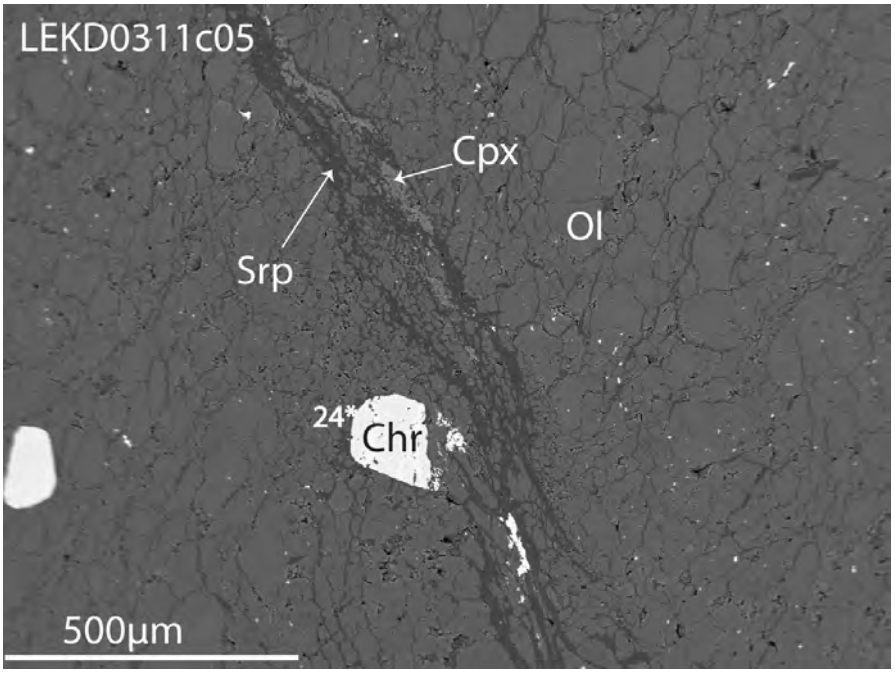

(a)

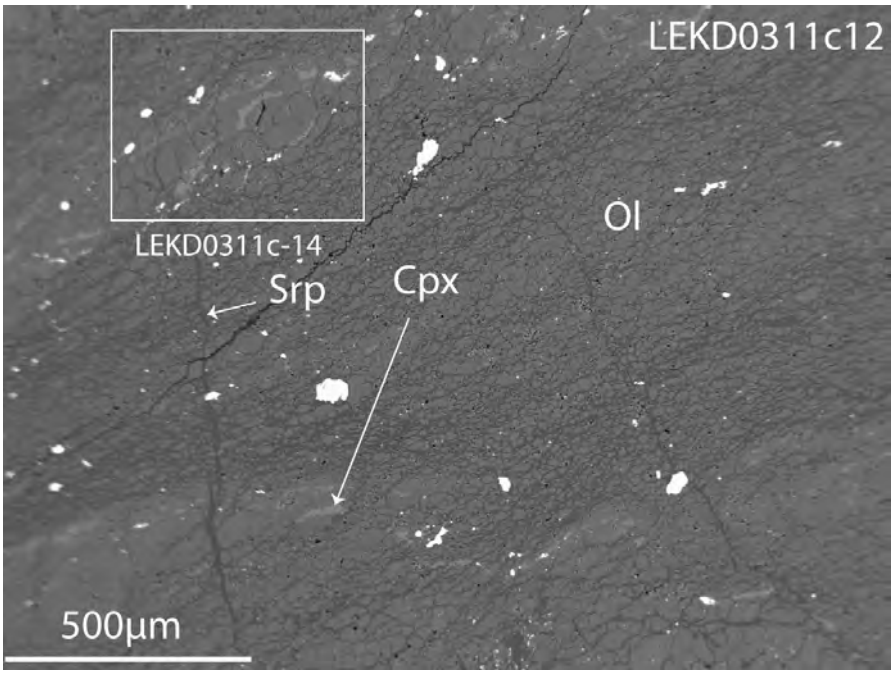

(b)

Figure 4.17: (a): Clinopyroxene band along a serpentine vein. (b): Clinopyroxene bands along a deformation zone. White number shows point for EMP analyses listed in table 4.5. The location of these BSE images are marked on the photomerge of the thinsection (Figure 4.15a) and are rotated 90° anti-clockwise compared to the thinsection (LEKD0311).

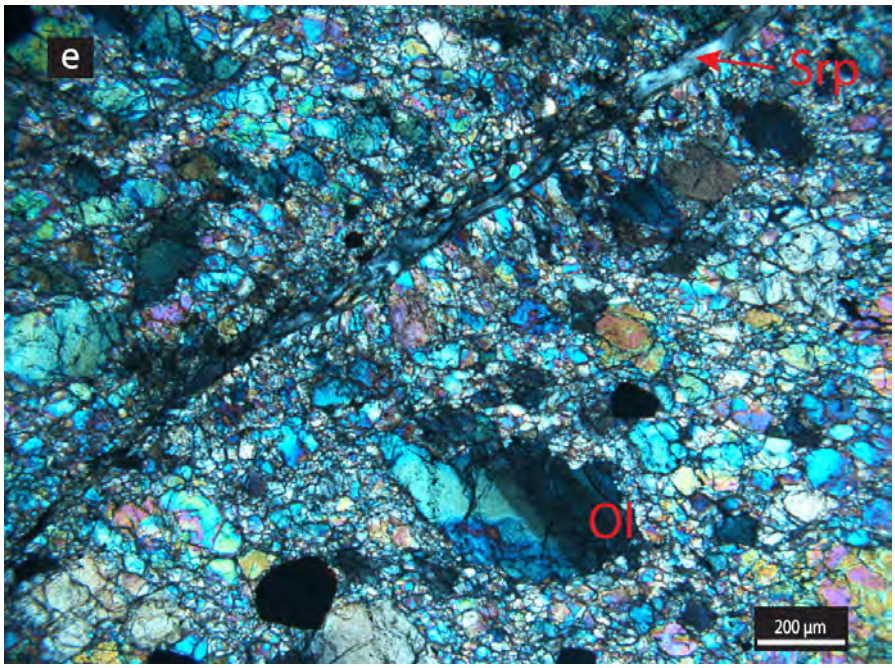

Figure 4.18: Olivines grow along a serpentine vein with their long axes perpendicular to the vein orientation resembling fibrous growth into an extensional vein. Note the straight subgrain boundaries and inclusion trails of the olivine porphyroclast.

Breccia

Sample LEKD0411 (Figure 4.19), was collected from a clast supported breccia (Figure 2.22b). It contains the following minerals; olivine(Fo91-95), serpentine, clinopyroxene and chromite. Minor pentlandite (FeNiS) were detected by EDS. The rock is moderately serpentinized.

Fabrics changes across the thinsection reflecting the different clasts that constitute this breccia. The thinsection is therefore divided into different fault-bound domains based on the differences in fabric.

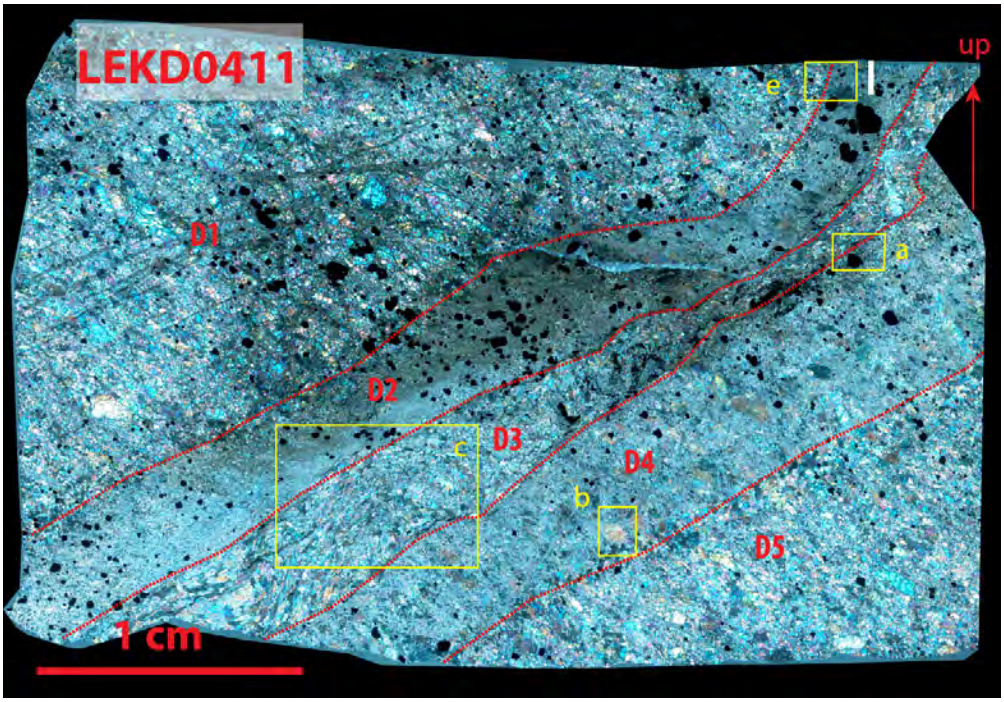

Figure 4.19: Photomerge of thinsection representing breccia at outcrop A.

Olivine Domain 1: The distribution of olivine resembles LEKD0311. Grain sizes vary from ~10μm to 2mm. Porphyroclasts show typical olivine fracturing, undulose extinction and have inclusions. Larger porphyroclasts have a shape preferred orientation making up an oblique foliation from upper left to lower right. Most porphyroclast have intermediate sizes (<1mm). The domain is set of criss-crossing fractures. Small clasts are loosely organized in bands following the same foliation. Larger clasts occur along (dehydrated?) serpentine veins (Figure 4.21 and 4.22). Such grains often have a typical elongated shape perpendicular to the vein. They may also display a local sense of shear. The larger clasts formed along serpentine veins had the highest Fo component (up to 95) of the analyzed olivines.

Domain 2: High temperature mylonite with ultra-fine (<10μm) grains. This domain is shown in the upper left corner of Figure 4.23.

Domain 3: Olivines are elongated and bent. Elongation and bending vary within the domain (Figure 4.23). These olivines do not show undulose extinction and are interpreted to have formed by the simplified reaction srp $\longrightarrow$ ol during dehydration.

Domain 4: This domain consist predominantly of very fine to ultra-fine dynamically recrystallized olivine, but opposite to domain 2 this domain also has a few, intensely fragmented porphyroclast (0.5 -2mm), with a slightly shape preferred orientation (Figure 4.24).

Domain 5: Similar to domain 1, but less fractured.

Serpentine occur as interstitial matrix mineral and in thin veins. Locally the interstitial serpentine forms slightly larger areas (∼10-50μm). In connection with veins these areas may be up to 200μm in diameter (Figure 4.20) . Serpentine is also found as needle-shaped relicts in the ultra-mylonite.

The most Fe-rich serpentine is found in porous serpentine (Figure 4.20b) or adjacent to chromite.

Clinopyroxenes are diopsidic of composition and occur as clinopyroxene bands or grains intergrown with olivine along remains of serpentine veins as in Figure 4.22a from domain 1. The clinopyroxenes are all of type cpx3.

Chromite. In domain 1 chromites are euhedral to subhedral and loosely organized in a band deflecting into the ultra mylonitic zone. Along the boundaries of the mylonitic zone chromites occur locally as boudins. Anhedral to non-idiomorhic chromites are found in domain 3 (Figure 4.23). Chromite are occasionally depleted in Cr_2O_3 along some rugged fractures and faces.

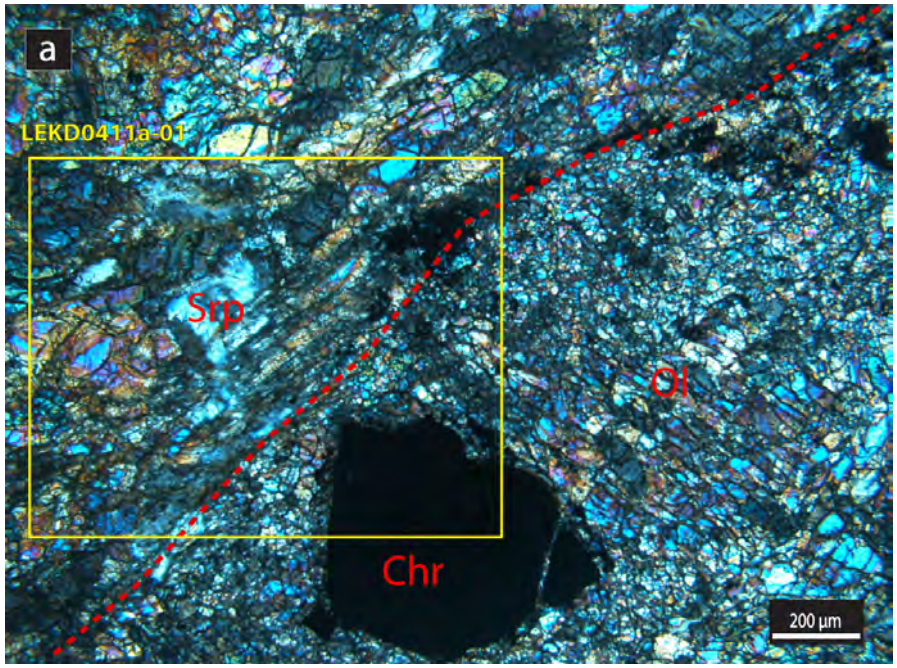

(a)

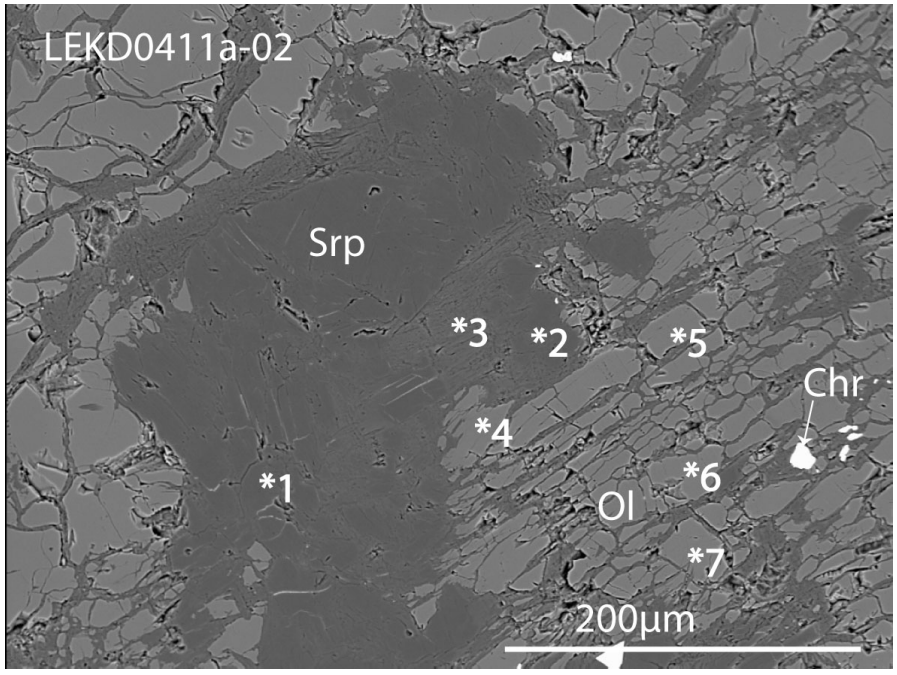

(b)

Figure 4.20: (a): Sheared olivine around chromite. The chromite is located in D4 at the boundary to D3. Note the different foliation direction in the two domains. Dashed red line indicate the boundary between D3 and D4. (b): The serpentine patch is situated in D3. In the lower left corner we see the sheared olivine lamellae from the shear zone. Grains in the upper left corner are less impacted by the relatively local shearing at the fault plane. White numbers show points for EMP analyses listed in tables 4.6 and 4.12. Optical microphotograph and BSE images.

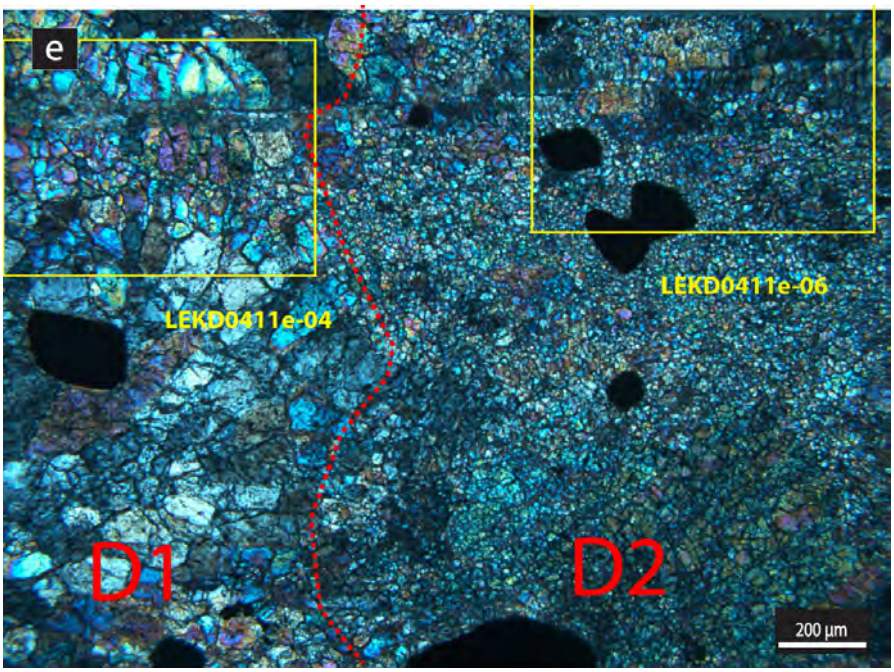

Figure 4.21: Nucleation and growth of olivine along a straight fracture. The microphotograph shows the boundary between D1 and D2. A serpentine vein transects both domains in the upper part. Olivine grows from the vein and outwards with their long dimensions perpendicular to the vein.

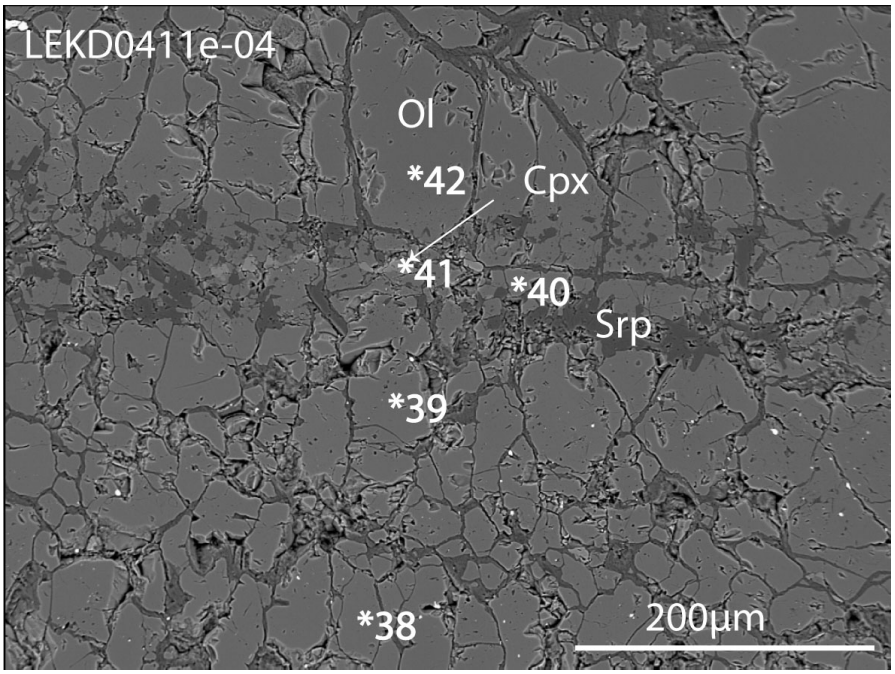

(a)

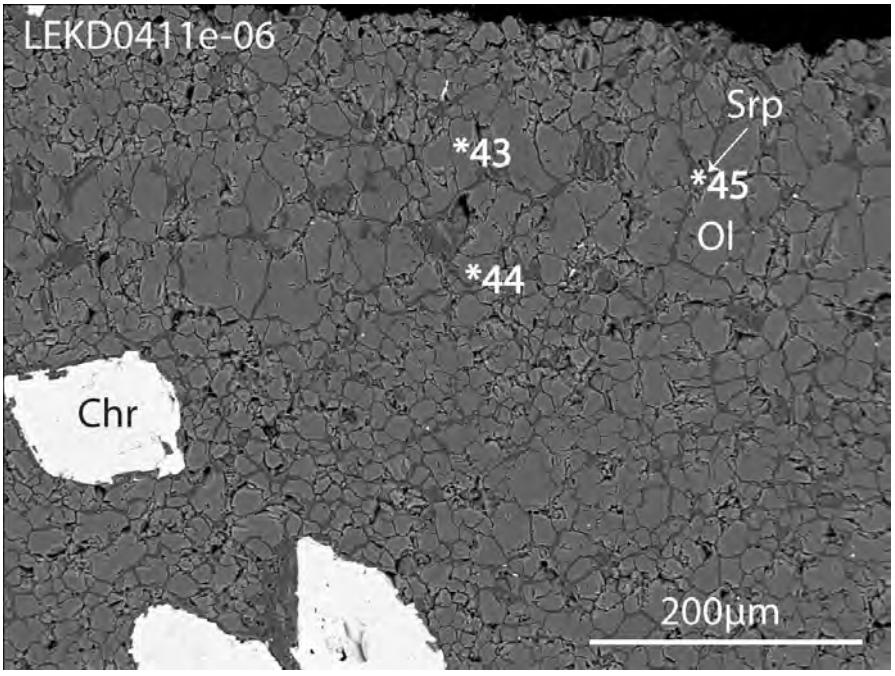

(b)

Figure 4.22: (a): D2: Two parallel zones of serpentine with a central fracture filled with serpentine. Olivine may have grown both from the central fracture and from former vein walls. (b): D1: The parallel zones turn into one zone. BSE images from outcrop A. White numbers show points for EMP analyses listed in tables 4.7, 4.8 and 4.10.

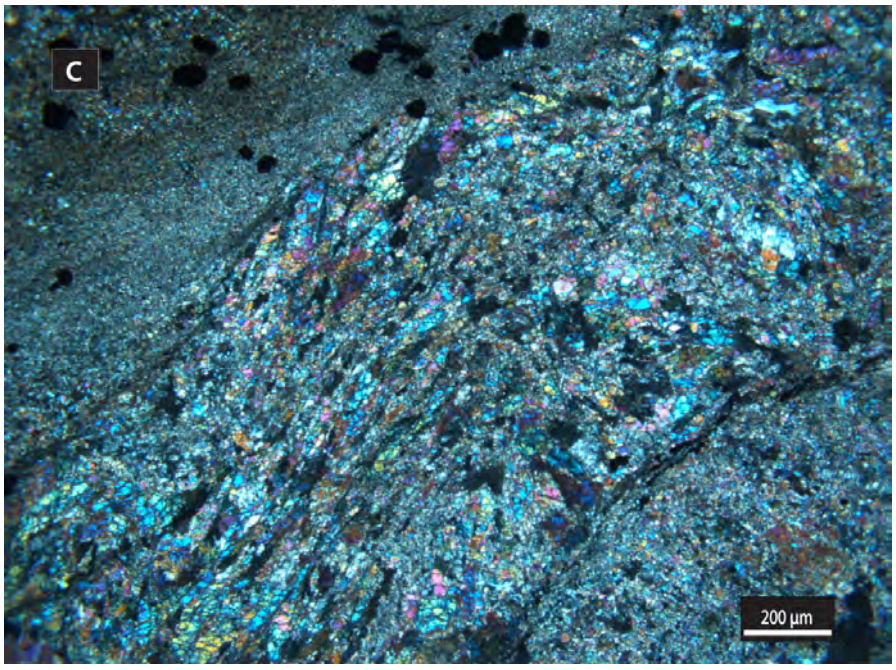

Figure 4.23: D3: Faultbound block with suspicious elongated olivine. The olivine may represent a metamorphic olivine after serpentine. Serpentine make up the matrix mineral. Chromite is smeared out along the fault plane. Optical microphotograph from outcrop A.

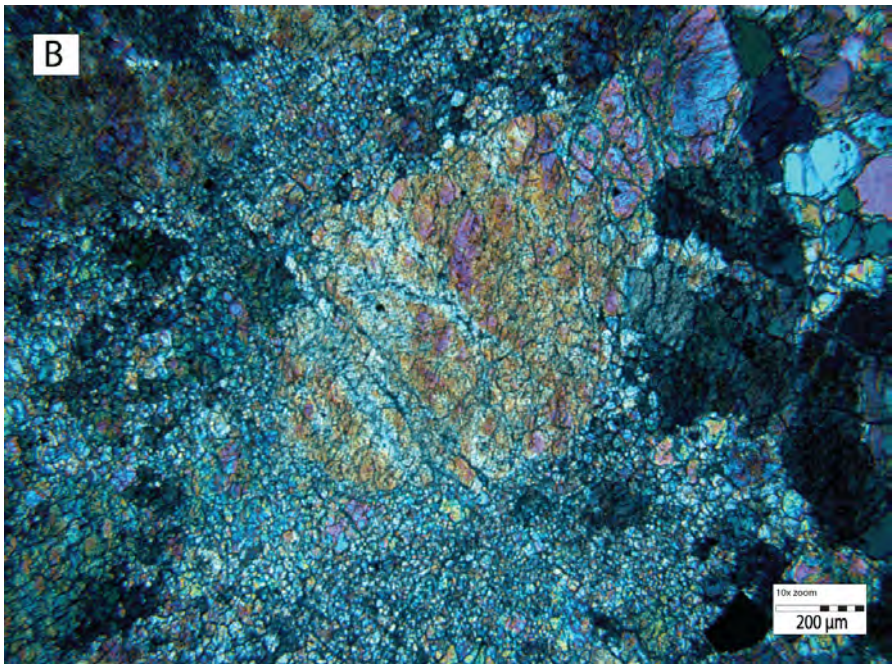

Figure 4.24: D4: Incipient kinking of olivine. Optical microphotograph from outcrop A.

Mylonite

Sample LEKD0511A (Figure 4.25) was drilled in a mylonite/breccia zone. The core include displaced chromite bands. The most prominent features are the bands of coarser grains. Due to their coarser sizes they appear brighter than the surrounding mylonite under crossed polars. A wedge shaped lens (breccia) is penetrating the sample from above. The rock is moderately serpentinized. A disseminated band of very fine chromite grains is oriented from the upper right corner and obliquely downwards were it halts towards a fracture perpendicular to the chromite band. An aggregate (∼0.5cm) of chromite is restricted on two sides by respectively a fracture and a wider zone of finer (10-50μm) recrystal

The sample contains the minerals: olivine(Fo92-94), serpentine, clinopyroxene, chromite. Minor NiFe-sulphides were interpreted by EDS.

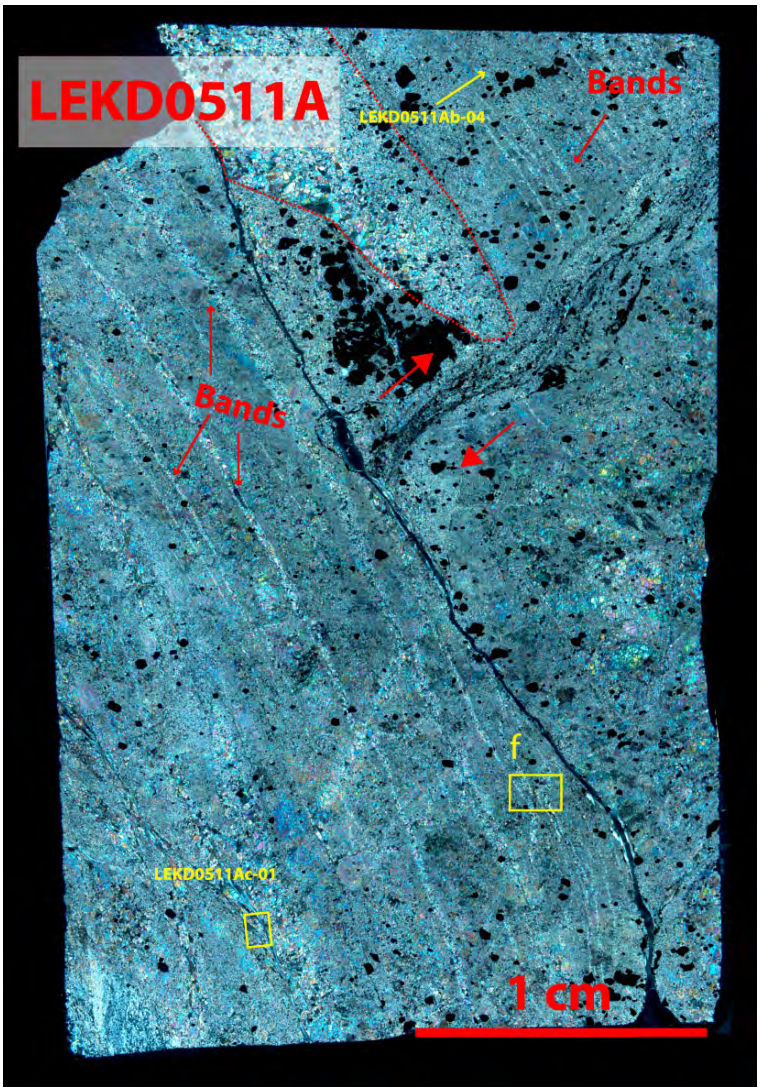

Figure 4.25: The microtexture is characterized by banding. The photomerge represents mylonites at outcrop A.

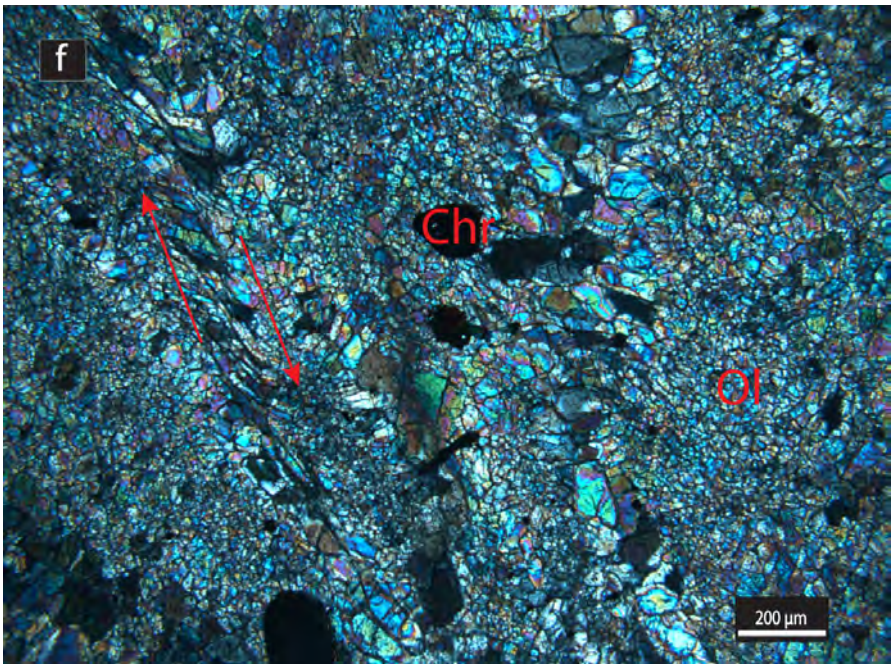

Figure 4.26: Converging bands with growth of olivine along fractures filled with serpentine. The amount of shear vary from band to band. Optical microphotograph.

Olivine. The bands are composed of olivine with a grain size between (10-50μm) across, in a matrix of very fine grained olivine (<10μm). The bands of slightly coarser olivine are also enriched in serpentine. Grain shapes in these zones vary from rounded (finer grains) in wider zones to angular (larger grains). In narrower zones olivine grows perpendicular at both sides of a central fracture or of parallel fractures. It is observed that olivine grows into larger grains along such structures than in other areas of recrystallized olivine.

The thin shear zones are variably sheared (Figure 4.26).

Serpentine occurs in veins. Locally veins are narrowed down into thin fractures, which form a basis for the growth of olivine along the vein/fracture.

Clinopyroxene(cpx3) are found in bands along serpentine veins (Figure 4.27). Their occur

Chromite are usually subhedral to non-idiomorphic. They also occur as trails and as inclusions in olivine.

The texture of the mylonite zones are characterized with growth of coarser olivine in zones where the amount of serpentine is high. This is a feature observed in several of the studied samples and may suggest that olivine was both serpentinized and that new olivine grains grew in equilibrium with serpentine in the high strain zone.

The same textures as described in the previous examples are observed in the remaining samples of subsite A1 and A2.

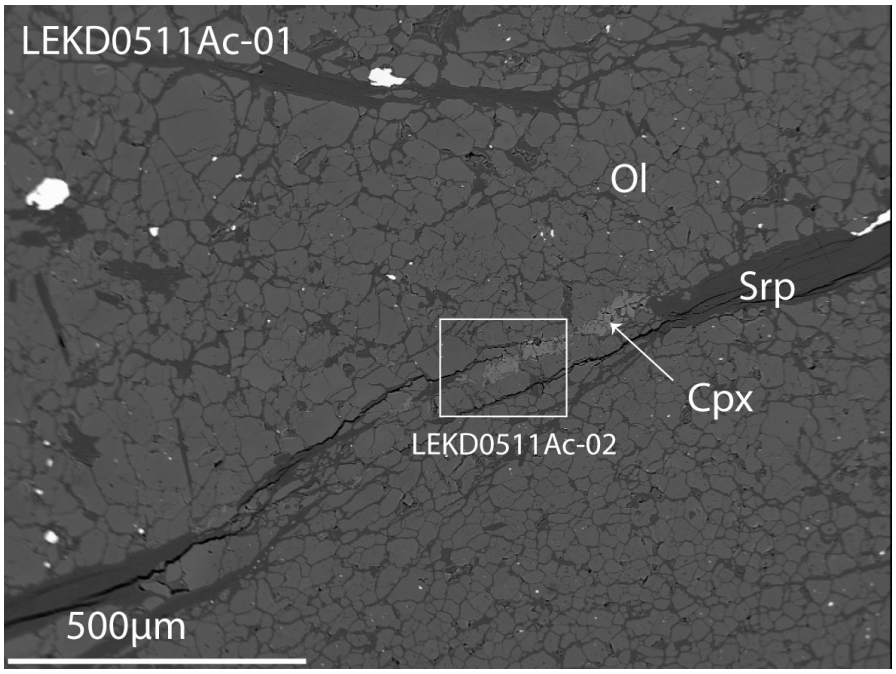

Figure 4.27: Formation of clinopyroxene(cpx3) organized in bands following a serpentine vein. The BSE image is rotated 90° anti-clockwise compared to thinsection(LEKD0511A). Outcrop A.

Sample: LEKD	0311	0311	0311	0311	0311	0311	0311	0311	0311	0311	0311	0311	0311	0311	0311
Analysis #	1	2	3	4	5	20	21	22	23	24	25	26	27	28	42
Mineral	Ol	Ol	Ol	Ol	Ol	Ol	Ol	Ol	Ol	Ol	Ol	Ol	Ol	Ol	Ol
Comment	CF	CF	CF	CF	CF	WR	WR	WR	WR	WR	WR	WR	WR	WR	WR
[wt.%]															
SiO_2	41,33	41,69	41,56	42,24	41,70	41,55	41,89	41,25	41,48	41,46	41,43	41,39	41,21	41,32	41,39
TiO_2	n.d.	n.d.	n.d.	n.d.	n.d.	0,03	n.d.	n.d.	n.d.	n.d.	n.d.	n.d.	n.d.	n.d.	n.d.
Al_2O_3	n.d.	n.d.	0,04	n.d.	0,03	0,02	n.d.	n.d.	n.d.	n.d.	n.d.	n.d.	0,01	n.d.	n.d.
Cr_2O_3	n.d.	0,05	0,03	n.d.	n.d.	0,07	0,01	0,03	n.d.	0,01	0,02	n.d.	0,05	0,04	0,02
FeO(tot)	7,94	8,09	6,91	6,96	7,82	7,30	5,87	6,87	7,51	7,19	7,06	7,38	7,97	7,14	6,09
NiO	0,45	0,66	0,11	0,15	0,45	0,18	0,14	0,13	0,27	0,11	0,16	0,26	0,30	0,25	0,38
MgO	51,27	50,84	52,53	52,17	50,84	51,84	53,03	52,75	50,97	52,19	51,70	51,46	51,42	51,45	52,61
MnO	0,09	0,06	0,03	0,06	0,13	0,13	0,07	n.d.	0,18	0,11	0,08	0,14	0,17	0,10	0,07
CaO	0,01	0,03	n.d.	0,03	n.d.	n.d.	0,01	0,05	0,02	0,04	0,01	0,01	0,01	n.d.	0,02
Na_2O	n.d.	0,02	n.d.	n.d.	n.d.	n.d.	n.d.	0,01	n.d.	n.d.	n.d.	n.d.	0,01	n.d.	0,01
K_2O	0,01	n.d.	0,01	n.d.	n.d.	0,01	n.d.	0,01	0,02	n.d.	n.d.	n.d.	0,01	0,02	n.d.
Total	101,09	101,43	101,24	101,61	100,97	101,13	101,01	101,10	100,45	101,12	100,47	100,65	101,16	100,32	100,60
Si	0,995	1,001	0,993	1,004	1,003	0,996	0,998	0,987	1,002	0,993	0,998	0,997	0,992	0,998	0,993
Ti	n.d.	n.d.	n.d.	n.d.	n.d.	0,001	n.d.	n.d.	n.d.	n.d.	n.d.	n.d.	n.d.	n.d.	n.d.
Al	n.d.	n.d.	0,001	n.d.	0,001	0,001	n.d.	n.d.	n.d.	n.d.	n.d.	n.d.	n.c.	n.d.	n.d.
Cr	n.d.	0,001	0,001	n.d.	n.d.	0,001	n.c.	n.c.	n.d.	n.c.	n.c.	n.d.	0,001	0,001	n.c.
Fe	0,160	0,162	0,138	0,138	0,157	0,146	0,117	0,138	0,152	0,144	0,142	0,149	0,160	0,144	0,122
Ni	0,009	0,013	0,002	0,003	0,009	0,004	0,003	0,003	0,005	0,002	0,003	0,005	0,006	0,005	0,007
Mg	1,840	1,819	1,871	1,849	1,823	1,852	1,883	1,883	1,835	1,864	1,856	1,849	1,844	1,852	1,881
Mn	0,002	0,001	0,001	0,001	0,003	0,003	0,001	n.d.	0,004	0,002	0,002	0,003	0,003	0,002	0,001
Ca	n.c.	0,001	n.d.	0,001	n.d.	n.d.	n.c.	0,001	n.c.	0,001	n.c.	n.c.	n.c.	n.d.	0,001
Na	n.d.	0,001	n.d.	n.d.	n.d.	n.d.	n.d.	0,001	n.d.	n.d.	n.d.	n.d.	n.c.	n.d.	n.c.
K	n.c.	n.d.	n.c.	n.d.	n.d.	n.c.	n.d.	n.c.	n.c.	n.d.	n.d.	n.d.	n.d.	0,001	n.c.
Total	3,005	2,999	3,006	2,996	2,996	3,003	3,002	3,013	2,998	3,007	3,002	3,003	3,008	3,002	3,007
Mg/(Mg+Fe)	0,92	0,92	0,93	0,93	0,92	0,93	0,94	0,93	0,92	0,93	0,93	0,93	0,92	0,93	0,94

Table 4.5: Analyses of olivine, part 1. Sorted by increasing sample numbers. CF = central fracture, WR = wall rock, n.d. = not detected, n.c. = not calculated. Calculated on 4 oxygens.

Sample: LEKD	0311	0311	0311	0311	0311	0411	0411	0411	0411	0411	0411	0411	0411	0411	0411
Analysis #	43	45	47	48	49	4	5	6	7	8	10	12	16	22	23
Mineral	Ol	Ol	Ol	Ol	Ol	Ol	Ol	Ol	Ol	Ol	Ol	Ol	Ol	Ol	Ol
Comment	AH	CF	WR	WR	D3	D3	D3	D3	D3	D3	D3	D3	D4	D1	D1
[wt.%]															
SiO_2	41,80	41,79	41,21	40,78	41,37	41,29	40,67	41,11	41,21	41,74	41,38	41,69	41,09	40,63	40,71
TiO_2	0,01	n.d.	n.d.	n.d.	n.d.	0,02	0,02	0,01	0,01	n.d.	n.d.	n.d.	n.d.	n.d.	n.d.
Al_2O_3	n.d.	n.d.	0,01	0,01	0,01	n.d.	n.d.	n.d.	n.d.	n.d.	n.d.	n.d.	n.d.	n.d.	n.d.
Cr_2O_3	0,05	0,04	n.d.	0,05	n.d.	0,02	0,01	0,03	n.d.	0,20	0,03	0,03	0,18	0,02	0,03
FeO(tot)	6,05	5,56	8,14	8,31	7,83	7,46	7,15	7,71	7,78	7,36	8,54	6,92	8,51	7,74	7,65
NiO	0,36	0,22	0,37	0,30	0,39	0,25	0,16	0,28	0,39	0,12	0,38	0,13	0,22	0,30	0,40
MgO	52,31	53,36	51,01	50,48	50,70	51,62	50,77	51,14	51,38	51,21	50,34	51,55	49,88	50,79	50,99
MnO	0,06	0,01	0,12	0,10	0,14	0,09	0,08	0,08	0,12	0,07	0,07	0,06	0,12	0,13	0,14
CaO	0,02	0,03	n.d.	n.d.	0,06	0,03	0,04	n.d.	n.d.	n.d.	n.d.	0,07	0,01	0,04	0,02
Na_2O	n.d.	n.d.	n.d.	n.d.	n.d.	n.d.	0,01	n.d.	n.d.	n.d.	n.d.	n.d.	n.d.	n.d.	0,02
K_2O	n.d.	n.d.	0,01	n.d.	n.d.	n.d.	n.d.	0,01	n.d.	n.d.	n.d.	n.d.	n.d.	n.d.	0,01
Total	100,66	101,02	100,86	100,02	100,50	100,78	98,92	100,35	100,89	100,71	100,74	100,46	100,00	99,66	99,95
Si	1,001	0,995	0,995	0,994	1,001	0,994	0,996	0,995	0,993	1,003	1,001	1,003	1,001	0,992	0,991
Ti	n.c.	n.d.	n.d.	n.d.	n.d.	n.c.	n.c.	n.c.	n.c.	n.d.	n.d.	n.d.	n.d.	n.d.	n.d.
Al	n.d.	n.d.	n.c.	n.c.	n.c.	n.d.	n.d.	n.d.	n.d.	n.d.	n.d.	n.d.	n.d.	n.d.	n.d.
Cr	0,001	0,001	n.d.	0,001	n.d.	n.c.	n.c.	n.c.	n.d.	0,004	0,001	0,001	0,003	n.c.	0,001
Fe	0,121	0,111	0,164	0,169	0,158	0,150	0,147	0,156	0,157	0,148	0,173	0,139	0,173	0,158	0,156
Ni	0,007	0,004	0,007	0,006	0,008	0,005	0,003	0,005	0,007	0,002	0,007	0,003	0,004	0,006	0,008
Mg	1,867	1,893	1,836	1,834	1,828	1,853	1,854	1,845	1,846	1,835	1,816	1,848	1,812	1,848	1,850
Mn	0,001	n.c.	0,002	0,002	0,003	0,002	0,002	0,002	0,002	0,001	0,001	0,001	0,002	0,003	0,003
Ca	0,001	0,001	n.d.	n.c.	0,001	0,001	0,001	n.d.	n.d.	n.d.	n.d.	0,002	n.c.	0,001	n.c.
Na	n.d.	n.d.	n.d.	n.d.	n.d.	n.d.	n.c.	n.d.	n.d.	n.d.	n.d.	n.d.	n.d.	n.d.	0,001
K	n.d.	n.d.	n.c.	n.d.	n.d.	n.d.	n.d.	n.c.	n.d.	n.d.	n.d.	n.d.	n.d.	n.d.	n.d.
Total	2,999	3,005	3,005	3,006	2,999	3,005	3,003	3,005	3,006	2,995	2,999	2,997	2,997	3,008	3,009
Mg/(Mg+Fe)	0,94	0,94	0,92	0,92	0,92	0,93	0,93	0,92	0,92	0,93	0,91	0,93	0,91	0,92	0,92

Table 4.6: Analyses of olivine, part 2. Sorted by increasing sample numbers. CF = central fracture, WR = wall rock, D = domain , n.d. = not detected, n.c. = not calculated. Calculated on 4 oxygens.

Sample: LEKD	0411	0411	0411	0411	0411	0411	0411	0411	0411	0411	0411	0411	0411	0411	0411
Analysis #	24	25	26	27	28	29	30	31	32	33	34	36	38	39	40
Mineral	Ol	Ol	Ol	Ol	Ol	Ol	Ol	Ol	Ol	Ol	Ol	Ol	Ol	Ol	Ol
Comment	D1	D1	D1	D1	D1	D1	D1	D1	D1	D1	D1	D1	D1	D1	D1
[wt.%]															
SiO_2	40,82	41,19	41,27	41,59	41,42	41,41	41,89	40,43	40,32	41,10	41,06	41,29	41,58	41,70	41,54
TiO_2	n.d.	n.d.	n.d.	0,01	n.d.	0,01	0,01	n.d.	n.d.	n.d.	n.d.	0,03	n.d.	n.d.	0,02
Al_2O_3	n.d.	n.d.	0,01	0,01	n.d.	n.d.	n.d.	n.d.	n.d.	n.d.	n.d.	0,01	0,01	0,05	0,01
Cr_2O_3	0,15	n.d.	n.d.	n.d.	0,03	n.d.	n.d.	0,02	n.d.	n.d.	0,02	0,05	n.d.	0,03	0,03
FeO(tot)	7,10	7,52	7,40	6,55	6,73	7,38	7,07	8,07	7,67	7,38	7,32	6,58	6,44	6,09	6,91
NiO	0,30	0,29	0,33	0,34	0,29	0,31	0,32	0,28	0,26	0,34	0,35	0,18	0,40	0,47	0,05
MgO	51,45	51,38	51,26	52,19	51,84	50,70	51,80	50,49	50,77	51,17	50,82	51,23	51,60	51,97	52,46
MnO	0,15	0,13	0,15	0,11	0,07	0,08	0,07	0,17	0,11	0,14	0,14	0,04	0,06	0,05	0,06
CaO	0,03	n.d.	0,02	n.d.	0,04	0,02	n.d.	0,02	0,04	0,04	0,04	0,04	0,02	0,03	0,06
Na_2O	n.d.	n.d.	n.d.	n.d.	n.d.	n.d.	n.d.	n.d.	0,01	0,01	n.d.	0,01	n.d.	n.d.	n.d.
K_2O	n.d.	0,01	0,01	0,01	0,01	0,01	0,01	n.d.	n.d.	n.d.	n.d.	0,02	n.d.	0,01	n.d.
Total	100,00	100,51	100,44	100,80	100,43	99,91	101,18	99,48	99,18	100,17	99,74	99,47	100,11	100,41	101,14
Si	0,990	0,995	0,997	0,997	0,997	1,004	1,002	0,990	0,989	0,996	0,999	1,002	1,003	1,001	0,993
Ti	n.d.	n.d.	n.d.	n.c.	n.d.	n.c.	n.c.	n.d.	n.d.	n.d.	n.d.	n.c.	n.d.	n.d.	n.c.
Al	n.d.	n.d.	n.c.	n.c.	n.d.	n.d.	n.d.	n.d.	n.d.	n.d.	n.d.	n.c.	n.c.	0,001	n.c.
Cr	0,003	n.d.	n.d.	n.d.	0,001	n.d.	n.d.	n.c.	n.d.	n.d.	n.c.	0,001	n.d.	0,001	0,001
Fe	0,144	0,152	0,150	0,131	0,135	0,150	0,141	0,165	0,157	0,150	0,149	0,134	0,130	0,122	0,138
Ni	0,006	0,006	0,006	0,007	0,006	0,006	0,006	0,005	0,005	0,007	0,007	0,004	0,008	0,009	0,001
Mg	1,861	1,850	1,846	1,865	1,861	1,833	1,847	1,844	1,856	1,848	1,843	1,854	1,855	1,861	1,870
Mn	0,003	0,003	0,003	0,002	0,002	0,002	0,002	0,003	0,002	0,003	0,003	0,001	0,001	0,001	0,001
Ca	0,001	n.d.	n.c.	n.d.	0,001	n.c.	n.d.	0,001	0,001	0,001	0,001	0,001	0,001	0,001	0,001
Na	n.d.	n.d.	n.d.	n.d.	n.d.	n.d.	n.d.	n.d.	n.c.	n.c.	n.d.	n.c.	n.d.	n.d.	n.d.
K	n.d.	n.c.	n.c.	n.c.	n.c.	n.c.	n.c.	n.d.	n.d.	n.d.	n.d.	0,001	n.d.	n.c.	n.d.
Total	3,008	3,005	3,003	3,003	3,003	2,996	2,998	3,009	3,011	3,004	3,001	2,997	2,997	2,998	3,006
Mg/(Mg+Fe)	0,93	0,92	0,93	0,93	0,93	0,92	0,93	0,92	0,92	0,93	0,93	0,93	0,93	0,94	0,93

Table 4.7: Analyses of olivine, part 3. Sorted by increasing sample numbers. D = domain ,n.d. = not detected, n.c. = not calculated. Calculated on 4 oxygens.

Sample: LEKD	0411	0411	0411	0411	0511A	0511A	0511A	0511A	0511A	0511A	0511A	0511A	0511A	0511A
Analysis #	42	43	44	47	2	3	8	11	12	15	20	22	23	24
Mineral	Ol	Ol	Ol	Ol	Ol	Ol	Ol	Ol	Ol	Ol	Ol	Ol	Ol	Ol
Comment	D1	D1	D1	D1	Band	Band	Band	ACA	ACA	ACA	ACA	SV	SV	ACA
[wt.%]														
SiO_2	41,77	42,00	42,00	41,77	40,89	41,60	41,91	42,07	41,80	42,02	40,93	41,46	41,43	40,59
TiO_2	n.d.	n.d.	0,02	n.d.	n.d.	n.d.	n.d.	n.d.	n.d.	n.d.	n.d.	0,02	0,03	n.d.
Al_2O_3	0,01	n.d.	n.d.	n.d.	n.d.	0,03	0,02	0,01	n.d.	n.d.	n.d.	n.d.	n.d.	0,01
Cr_2O_3	0,28	0,05	0,02	0,01	0,02	n.d.	0,04	0,47	0,12	0,70	0,01	n.d.	0,02	0,97
FeO(tot)	5,06	6,76	6,60	7,74	7,17	7,34	6,76	6,65	6,71	6,26	6,98	7,82	6,94	7,45
NiO	0,25	0,08	0,12	0,27	0,31	0,42	0,06	0,42	0,38	0,42	0,15	0,25	0,17	0,14
MgO	53,57	51,88	51,72	51,61	51,73	51,45	52,02	52,24	52,11	53,02	51,80	51,65	51,91	52,20
MnO	n.d.	0,09	0,06	0,12	0,06	0,03	0,03	0,09	0,07	0,04	0,04	0,07	0,07	0,03
CaO	0,02	0,04	0,02	0,03	0,01	n.d.	0,02	0,02	0,03	n.d.	0,04	0,01	0,03	0,04
Na_2O	n.d.	0,01	n.d.	n.d.	n.d.	n.d.	0,01	n.d.	n.d.	n.d.	n.d.	n.d.	n.d.	n.d.
K_2O	n.d.	n.d.	n.d.	0,01	n.d.	0,01	n.d.	0,01	n.d.	0,01	n.d.	n.d.	0,01	n.d.
Total	100,96	100,90	100,57	101,55	100,18	100,88	100,85	101,97	101,22	102,47	99,95	101,28	100,61	101,43
Si	0,993	1,005	1,007	0,999	0,990	1,000	1,003	0,998	0,999	0,992	0,992	0,994	0,996	0,975
Ti	n.d.	n.d.	n.c.	n.d.	n.d.	n.d.	n.d.	n.d.	n.d.	n.d.	n.d.	n.c.	n.d.	n.d.
Al	n.c.	n.d.	n.d.	n.d.	n.d.	0,001	n.c.	n.c.	n.d.	n.d.	n.d.	n.d.	n.c.	n.c.
Cr	0,005	0,001	n.c.	n.c.	n.c.	n.c.	0,001	0,009	0,002	0,013	n.c.	n.d.	n.c.	0,018
Fe	0,101	0,135	0,132	0,155	0,145	0,147	0,135	0,132	0,134	0,124	0,141	0,157	0,140	0,150
Ni	0,005	0,002	0,002	0,005	0,006	0,008	0,001	0,008	0,007	0,008	0,003	0,005	0,003	0,003
Mg	1,899	1,850	1,848	1,839	1,867	1,843	1,855	1,848	1,856	1,865	1,871	1,847	1,861	1,869
Mn	n.d.	0,002	0,001	0,002	0,001	0,001	0,001	0,002	0,001	0,001	0,001	0,002	0,001	0,001
Ca	0,001	0,001	0,001	0,001	n.c.	n.d.	n.c.	n.c.	0,001	n.d.	0,001	n.c.	0,001	0,001
Na	n.d.	n.c.	n.d.	n.d.	n.d.	n.d.	n.c.	n.d.	n.d.	n.d.	n.d.	n.d.	n.d.	n.d.
K	n.d.	n.d.	n.d.	n.c.	n.d.	n.c.	n.d.	n.c.	n.d.	n.c.	n.d.	n.d.	n.c.	n.d.
Total	3,004	2,995	2,993	3,001	3,010	3,000	2,997	2,998	3,000	3,002	3,008	3,005	3,003	3,016
Mg/(Mg+Fe)	0,95	0,93	0,93	0,92	0,93	0,93	0,93	0,93	0,93	0,94	0,93	0,92	0,93	0,93

Table 4.8: Analyses of olivine, part 4. Sorted by increasing sample numbers. D = domain, ACA = adjacent chromite aggregate, SV = larger serpentine vein n.d. = not detected, n.c. = not calculated. Calculated on 4 oxygens.

Sample: LEKD	0511A	0511A	0511A	0511A	0511A
Analysis #	26	27	29	32	33
Mineral	Ol	Ol	Ol	Ol	Ol
Comment	ACA	ACA	WL	WL	WL
[wt.%]					
SiO_2	42,01	41,32	41,30	41,02	41,36
TiO_2	n.d.	n.d.	n.d.	n.d.	0,01
Al_2O_3	n.d.	n.d.	n.d.	n.d.	n.d.
Cr_2O_3	0,56	0,12	0,01	0,04	0,02
FeO(tot)	7,01	8,34	7,21	8,40	6,54
NiO	0,07	0,37	0,32	0,35	0,10
MgO	51,71	50,45	50,97	51,14	52,23
MnO	0,06	0,06	0,09	0,07	n.d.
CaO	0,02	n.d.	0,04	0,02	0,05
Na_2O	n.d.	n.d.	n.d.	n.d.	n.d.
K_2O	0,01	0,01	0,01	0,01	n.d.
Total	101,46	100,67	99,96	101,04	100,31
Si	1,002	1,000	1,001	0,990	0,995
Ti	n.d.	n.d.	n.d.	n.d.	n.c.
Al	n.d.	n.d.	n.d.	n.d.	n.d.
Cr	0,010	0,002	n.c.	0,001	n.c.
Fe	0,140	0,169	0,146	0,170	0,132
Ni	0,001	0,007	0,006	0,007	0,002
Mg	1,838	1,820	1,842	1,840	1,874
Mn	0,001	0,001	0,002	0,001	n.d.
Ca	0,001	n.d.	0,001	n.c.	0,001
Na	n.d.	n.d.	n.d.	n.d.	n.d.
K	n.c.	n.c.	n.c.	n.c.	n.d.
Total	2,993	2,999	2,999	3,010	3,004
Mg/(Mg+Fe)	0,93	0,92	0,93	0,92	0,93

Table 4.9: Analyses of olivine, part 5. Sorted by increasing sample numbers. ACA = adjacent chromite aggregate, WL = wedge shaped lens, n.d. = not detected, n.c. = not calculated. Calculated on 4 oxygens.

Sample:LEKD	0311	0311	0411	0411	0411	0411	0411	0411	0511A	0511A	0511A	0511A
Analysis#	30	41	9	11	35	41	46	48	6	14	19	30
Mineral	Cpx3	Cpx3	Cpx3	Cpx3	Cpx3	Cpx3	Cpx3	Cpx3	Cpx3	Cpx3	Cpx3	Cpx3
Comment	WR	SV	D3	D3	D1	D1	D1	D1	Band	ACA	ACA	WL
SiO_2	55,85	55,23	55,69	55,54	55,12	55,52	55,52	55,92	55,79	56,09	55,45	55,49
TiO_2	0,01	0,00	0,00	0,01	0,01	0,00	0,00	0,00	0,02	0,00	0,03	0,00
Al_2O_3	0,00	0,00	0,00	0,01	0,03	0,00	0,12	0,05	0,00	0,02	0,00	0,00
Cr_2O_3	0,06	0,12	0,05	0,11	0,02	0,06	0,02	0,05	0,08	0,63	0,13	0,02
FeO(tot)	0,72	0,74	0,90	0,78	0,90	0,85	1,21	1,15	0,79	1,00	0,76	0,87
MnO	0,05	0,01	0,00	0,00	0,00	0,03	0,04	0,00	0,04	0,00	0,02	0,03
MgO	18,49	18,16	18,14	17,99	19,01	18,10	18,87	18,11	18,01	18,67	18,38	18,43
NiO	0,04	0,06	0,01	0,06	0,01	0,02	0,07	0,08	0,07	0,03	0,02	0,00
CaO	26,32	26,50	26,22	26,50	25,91	25,97	25,34	25,73	26,12	26,01	26,27	26,19
Na_2O	0,02	0,02	0,03	0,00	0,04	0,04	0,18	0,08	0,02	0,01	0,04	0,03
K_2O	0,01	0,00	0,00	0,00	0,00	0,00	0,01	0,01	0,00	0,00	0,00	0,00
SUM	101,55	100,83	101,03	100,99	101,06	100,59	101,36	101,16	100,94	102,46	101,11	101,06
mg#	97,9	97,8	97,3	97,6	97,4	97,4	96,5	96,6	97,6	97,1	97,7	97,4
Si	1,988	1,982	1,995	1,992	1,966	1,997	1,976	2,002	2,001	1,982	1,983	1,984
Al IV	0,000	0,000	0,000	0,000	0,001	0,000	0,005	0,000	0,000	0,001	0,000	0,000
Al VI	0,000	0,000	0,000	0,000	0,000	0,000	0,000	0,002	0,000	0,000	0,000	0,000
Ti	0,000	0,000	0,000	0,000	0,000	0,000	0,000	0,000	0,000	0,000	0,001	0,000
Cr	0,002	0,003	0,001	0,003	0,001	0,002	0,000	0,001	0,002	0,018	0,004	0,001
Fe^{3+}	0,012	0,017	0,005	0,006	0,027	0,004	0,027	0,000	0,000	0,009	0,016	0,017
Fe^{2+}	0,009	0,005	0,022	0,017	0,000	0,022	0,008	0,034	0,024	0,021	0,007	0,010
Mn	0,002	0,000	0,000	0,000	0,000	0,001	0,001	0,000	0,001	0,000	0,001	0,001
Mg	0,981	0,971	0,969	0,962	1,011	0,971	1,001	0,966	0,963	0,984	0,980	0,982
Ni	0,001	0,002	0,000	0,002	0,000	0,001	0,002	0,002	0,002	0,001	0,001	0,000
Ca	1,004	1,019	1,006	1,018	0,990	1,001	0,966	0,987	1,004	0,985	1,006	1,003
Na	0,002	0,001	0,002	0,000	0,003	0,003	0,012	0,005	0,001	0,001	0,003	0,002
ox	5,988	5,983	5,995	5,994	5,966	5,996	5,973	6,001	6,002	5,991	5,984	5,983
Al total	0,000	0,000	0,000	0,000	0,001	0,000	0,005	0,002	0,000	0,001	0,000	0,000
Fe tot	0,022	0,022	0,027	0,023	0,027	0,026	0,036	0,034	0,024	0,030	0,023	0,026
Fe3+	0,012	0,017	0,005	0,006	0,034	0,004	0,027	0,000	0,000	0,009	0,016	0,017
Di+Hd	1,002	1,018	1,006	1,018	0,989	1,000	0,960	0,987	1,003	0,984	1,006	1,002
En+Fs	-0,006	-0,021	-0,008	-0,020	0,011	-0,003	0,025	0,007	-0,008	0,010	-0,010	-0,005

Table 4.10: Analyses of clinopyroxene at outcrop A. Sorted by increasing sample numbers. WR = wall rock, SV = larger serpentine vein, D = domain, ACA = adjacent chromite aggregate, WL= wedge shaped lens. Structural formula according to Neumann (1976)

Sample: LEKD	0311	0311	0311	0311	0311	0311	0311	0311	0311	0311	0311	0311	0311	0311	0311
Analysis #	6	7	8	9	10	11	12	29	31	32	33	34	35	44	46
Mineral	Srp	Srp	Srp	Srp	Srp	Srp	Srp	Srp	Srp	Srp	Srp	Srp	Srp	Srp	Srp
Comment	CF	CF	CF	CF	CF	CF	CF	WR	WR	WR	WR	WR	WR	AH	WR
[wt.%]															
SiO_2	44,66	44,99	43,79	44,57	44,69	43,85	44,42	43,91	44,99	38,34	34,81	35,75	39,19	37,81	39,80
TiO_2	n.d.	0,02	n.d.	n.d.	n.d.	n.d.	0,01	n.d.	n.d.	n.d.	n.d.	n.d.	n.d.	0,02	n.d.
Al_2O_3	0,31	0,69	1,17	1,10	0,60	1,27	0,64	1,20	0,37	n.d.	0,04	n.d.	0,02	4,78	2,76
Cr_2O_3	0,01	0,06	0,10	0,09	0,07	0,81	0,11	0,43	0,06	n.d.	0,01	0,04	0,03	0,46	0,53
FeO(tot)	1,81	1,95	2,06	2,19	2,21	2,22	1,90	1,83	2,05	3,36	6,47	5,30	3,39	3,63	2,43
NiO	0,12	0,08	0,14	0,09	0,39	0,17	0,13	0,17	0,13	0,00	0,15	0,21	0,06	0,18	0,01
MgO	40,48	39,93	39,86	41,63	41,11	40,23	39,81	40,60	40,98	41,77	40,30	39,90	40,86	40,53	38,07
MnO	0,03	n.d.	n.d.	0,06	n.d.	0,01	0,05	0,03	n.d.	0,06	0,09	0,08	0,06	0,04	n.d.
CaO	n.d.	n.d.	n.d.	n.d.	n.d.	0,01	0,01	0,06	0,04	0,02	0,09	0,03	0,06	0,05	0,05
Na_2O	0,02	n.d.	0,02	0,01	0,01	0,04	0,01	0,01	0,01	n.d.	0,04	0,04	0,04	0,03	0,10
K_2O	n.d.	0,01	0,03	0,01	0,01	0,02	0,01	n.d.	0,01	0,01	0,01	n.d.	n.d.	n.d.	0,01
Total	87,43	87,73	87,19	89,75	89,10	88,63	87,09	88,23	88,63	83,54	82,00	81,35	83,70	87,53	83,74
Si	2,059	2,065	2,029	2,010	2,032	2,007	2,056	2,013	2,049	1,892	1,798	1,843	1,927	1,784	1,934
Ti	n.d.	0,001	n.d.	n.d.	n.d.	n.d.	n.c.	n.d.	n.d.	n.d.	n.d.	n.d.	n.d.	0,001	n.d.
Al	0,017	0,037	0,064	0,058	0,032	0,069	0,035	0,065	0,020	n.d.	0,002	n.d.	0,001	0,266	0,158
Cr	n.c.	0,002	0,004	0,003	0,002	0,029	0,004	0,016	0,002	n.d.	0,001	0,002	0,001	0,017	0,021
Fe	0,070	0,075	0,080	0,082	0,084	0,085	0,074	0,070	0,078	0,139	0,279	0,228	0,139	0,143	0,099
Ni	0,004	0,003	0,005	0,003	0,014	0,006	0,005	0,006	0,005	n.c.	0,006	0,009	0,002	0,007	n.c.
Mg	2,781	2,732	2,753	2,799	2,785	2,745	2,747	2,774	2,783	3,073	3,103	3,066	2,994	2,851	2,758
Mn	0,001	n.d.	n.d.	0,002	n.d.	0,001	0,002 1	0,001	n.d.	0,002	0,004	0,004	0,002	0,002	n.d.
Ca	n.d.	n.d.	n.d.	n.d.	n.d.	n.c.	n.c.	0,003	0,002	0,001	0,005	0,002	0,003	0,003	0,002
Na	0,001	n.d.	0,002	0,001	0,001	0,004	0,001	n.c.	0,001	n.d.	0,004	0,004	0,004	0,003	0,010
K	n.d.	0,001	0,002	0,001	0,001	0,001	0,001	n.d.	0,001	n.c.	0,001	n.d.	n.d.	n.d.	n.c.
Total	4,934	4,915	4,939	4,960	4,952	4,947	4,925	4,958	4,941	5,108	5,203	5,158	5,074	5,075	4,982
Mg/(Mg+Fe)	0,98	0,97	0,97	0,97	0,97	0,97	0,97	0,98	0,97	0,96	0,92	0,93	0,96	0,95	0,97

Table 4.11: Analyses of serpentine, part 1. Sorted by increasing sample numbers. CF = central fracture, AH = alteration halo, WR = wall rock, n.d. = not detected, n.c. = not calculated. Calculated on 7 oxygens.

Sample: LEKD	0411	0411	0411	0411	0411	0411	0411	0511A	0511A	0511A	0511A	0511A	0511A	0511A
Analysis #	1	2	3	15	19	37	45	4	7	16	21	25	31	34
Mineral	Srp	Srp	Srp	Srp	Srp	Srp	Srp	Srp	Srp	Srp	Srp	Srp	Srp	Srp
Comment	D3	D3	D3	D4	D4	D1	D1	Band	Band	ACA	ACA	ACA	SV	WL
[wt.%]														
SiO_2	44,60	42,16	34,85	33,27	34,41	44,70	35,57	39,77	42,08	33,32	39,70	35,98	42,03	39,82
TiO_2	0,01	0,01	n.d.	n.d.	n.d.	0,01	0,01	n.d.	n.d.	n.d.	0,02	0,01	n.d.	n.d.
Al_2O_3	0,80	2,61	8,00	9,36	0,01	0,38	n.d.	4,78	2,95	11,41	3,97	8,00	0,53	4,22
Cr_2O_3	0,13	1,30	3,90	4,99	0,12	0,08	0,03	0,78	1,17	3,91	0,77	5,01	0,35	0,82
FeO(tot)	1,93	2,27	2,53	3,16	5,47	1,94	5,39	1,84	1,83	2,54	2,08	3,02	2,91	1,85
NiO	0,01	0,01	0,03	0,19	0,27	0,04	0,06	0,18	0,17	0,24	0,03	0,10	0,18	0,00
MgO	40,98	38,74	35,40	34,67	43,49	40,42	39,54	38,78	40,26	34,21	38,30	36,63	41,21	37,57
MnO	0,02	n.d.	0,01	0,02	0,09	0,01	0,03	n.d.	n.d.	0,02	n.d.	n.d.	0,04	n.d.
CaO	n.d.	n.d.	0,03	n.d.	0,05	0,01	0,05	0,03	0,04	n.d.	0,03	0,01	n.d.	0,02
Na_2O	n.d.	n.d.	0,05	0,03	0,04	n.d.	0,10	0,11	0,08	0,04	0,07	0,08	n.d.	0,06
K_2O	n.d.	n.d.	0,02	0,01	n.d.	0,01	0,01	0,01	0,03	0,01	0,01	n.d.	n.d.	n.d.
Total	88,47	87,10	84,83	85,69	83,95	87,62	80,80	86,27	88,60	85,70	84,98	88,84	87,25	84,34
Si	2,034	1,965	1,700	1,622	1,736	2,057	1,846	1,874	1,931	1,611	1,899	1,686	1,969	1,913
Ti	n.c.	n.c.	n.d.	n.d.	n.d.	n.c.	0,001	n.d.	n.d.	n.d.	0,001	n.c.	n.d.	n.d.
Al	0,043	0,143	0,460	0,538	n.c.	0,020	n.d.	0,265	0,160	0,650	0,224	0,442	0,029	0,239
Cr	0,005	0,048	0,151	0,192	0,005	0,003	0,001	0,029	0,042	0,149	0,029	0,186	0,013	0,031
Fe	0,074	0,088	0,103	0,129	0,231	0,075	0,234	0,073	0,070	0,103	0,083	0,118	0,114	0,074
Ni	n.c.	n.c.	0,001	0,008	0,011	0,002	0,002	0,007	0,006	0,009	0,001	0,004	0,007	n.c.
Mg	2,786	2,693	2,575	2,521	3,270	2,772	3,059	2,724	2,753	2,465	2,731	2,559	2,878	2,691
Mn	0,001	n.d.	n.c.	0,001	0,004	0,001	0,001	n.d.	n.d.	0,001	n.d.	n.d.	0,001	n.d.
Ca	n.d.	n.d.	0,001	n.d.	0,003	0,001	0,003	0,002	0,002	n.d.	0,001	n.c.	n.d.	0,001
Na	n.d.	n.d.	0,005	0,003	0,004	n.d.	0,010	0,010	0,007	0,004	0,006	0,007	n.d.	0,006
K	n.d.	n.d.	0,001	n.c.	n.d.	0,001	0,001	n.c.	0,002	0,001	0,001	n.d.	n.d.	n.d.
Total	4,942	4,939	4,998	5,014	5,264	4,931	5,158	4,984	4,973	4,992	4,977	5,003	5,010	4,955
Mg/(Mg+Fe)	0,97	0,97	0,96	0,95	0,93	0,97	0,93	0,97	0,98	0,96	0,97	0,96	0,96	0,97

Table 4.12: Analyses of serpentine, part 2. D = domain, ACA = adjacent chromite aggregate, SV = larger serpentine vein, WL = wedge shaped lens. Sorted by increasing sample numbers. n.d. = not detected, n.c. = not calculated. Calculated on 7 oxygens.

Sample: LEKD	0311	0311	0311	0311	0311	0311	0311	0311	0411	0411	0411	0411	0511A	0511A	0511A	0511A	0312	0312	0312
Analysis #	17	15	16	36	37	38	39	50	13	14	17	18	10	13	17	18	20	28	29
Mineral	Mag	Chr	Chr	Chr	Chr	Chr	Chr	Chr	Chr	Chr	Chr	Chr	Chr	Chr	Chr	Chr	Chr	Chr	Chr
Comment	AH	AH	AH	WR	WR	WR	WR	WR	D4	D4	D4/D5	D4/D5	ACA	CA	CA	CA	-	-	-
[wt.%]																			
SiO_2	0,02	n.d.	0,01	0,05	0,05	n.d.	n.d.	n.d.	n.d.	n.d.	0,01	0,02	n.d.	0,02	0,01	0,02	0,02	0,23	n.d.
TiO_2	0,01	0,12	0,12	0,10	0,08	0,09	0,12	0,10	0,08	0,12	0,09	0,14	0,08	0,10	0,10	0,11	0,32	0,75	0,34
Al_2O_3	0,03	8,04	0,69	0,11	8,28	4,71	2,17	8,09	7,79	0,41	3,90	8,08	8,40	8,57	8,44	0,59	13,11	2,71	24,63
Al_2O_3	4,58	58,75	35,05	37,24	56,97	44,38	41,27	58,03	58,66	45,49	52,67	57,89	57,88	56,33	57,79	45,91	51,93	37,18	38,88
FeO(tot)	86,49	26,02	56,90	52,84	27,71	44,73	50,74	26,63	24,47	47,80	35,97	26,68	26,25	27,58	28,54	46,99	24,24	51,50	23,65
NiO	0,49	0,10	0,40	0,25	0,02	0,16	0,16	0,04	n.d.	0,17	0,01	0,01	0,11	n.d.	n.d.	0,29	0,07	0,35	0,15
MgO	0,48	7,16	2,08	2,42	6,03	3,67	3,06	6,82	8,16	3,08	4,76	7,14	7,09	5,83	5,25	2,54	9,40	2,60	10,21
MnO	n.d.	0,30	0,32	0,82	0,48	0,64	0,55	0,44	0,39	0,45	0,40	0,37	0,38	0,34	0,45	0,47	0,40	0,55	0,30
CaO	0,03	0,01	0,03	n.d.	n.d.	0,03	n.d.	n.d.	0,03	0,02	n.d.	n.d.	n.d.	0,02	n.d.	n.d.	0,05	0,02	n.d.
Na_2O	0,02	0,02	0,01	0,02	n.d.	0,01	0,04	0,02	0,02	0,03	n.d.	0,05	0,01	0,01	0,02	0,03	n.d.	0,02	n.d.
K_2O	0,01	n.d.	n.d.	n.d.	n.d.	n.d.	n.d.	n.d.	n.d.	n.d.	n.d.	n.d.	0,01	n.d.	n.d.	n.d.	0,01	n.d.	n.d.
Total	92,17	100,51	95,62	93,84	99,62	98,42	98,11	100,16	99,59	97,56	97,81	100,38	100,21	98,80	100,60	96,94	99,55	95,90	98,16
Si	0,001	n.d.	0,001	0,002	0,002	n.d.	n.d.	n.d.	n.d.	n.d.	n.c.	0,001	n.d.	0,001	0,000	0,001	0,001	0,009	n.d.
Ti	0,001	0,003	0,004	0,003	0,002	0,003	0,003	0,003	0,002	0,004	0,002	0,004	0,002	0,003	0,003	0,003	0,008	0,023	0,008
Al	0,002	0,324	0,034	0,006	0,340	0,212	0,102	0,328	0,315	0,019	0,172	0,327	0,340	0,354	0,344	0,028	0,515	0,130	0,925
Cr	0,183	1,590	1,175	1,262	1,567	1,341	1,298	1,580	1,593	1,439	1,556	1,571	1,570	1,560	1,579	1,460	1,368	1,197	0,979
Fe^{3+}	n.c.	n.c.	n.c.	n.c.	n.c.	n.c.	n.c.	n.c.	n.c.	n.c.	n.c.	n.c.	n.c.	n.c.	n.c.	n.c.	n.c.	n.c.	n.c.
Fe(tot)	3,660	0,745	2,018	1,894	0,806	1,429	1,687	0,767	0,703	1,599	1,124	0,766	0,753	0,808	0,825	1,581	0,676	1,754	0,630
Ni	0,020	0,003	0,014	0,008	0,001	0,005	0,005	0,001	n.d.	0,006	n.c.	n.c.	0,003	n.c.	n.d.	0,009	0,002	0,012	0,004
Mg	0,036	0,365	0,132	0,154	0,313	0,209	0,181	0,350	0,418	0,184	0,265	0,365	0,363	0,304	0,271	0,152	0,467	0,158	0,485
Mn	n.d.	0,009	0,011	0,030	0,014	0,021	0,019	0,013	0,011	0,015	0,013	0,011	0,011	0,010	0,013	0,016	0,011	0,019	0,008
Ca	0,002	n.c.	0,002	n.d.	n.d.	0,001	n.d.	n.d.	0,001	0,001	n.d.	n.d.	n.d.	0,001	n.d.	n.d.	0,002	0,001	n.d.
Na	0,002	0,001	0,001	0,002	n.d.	0,001	0,003	0,001	0,001	0,002	n.d.	0,003	0,001	n.c.	0,001	0,002	n.d.	0,001	n.d.
K	0,001	n.d.	n.d.	n.d.	n.d.	n.d.	n.d.	n.d.	n.d.	n.d.	n.d.	n.d.	n.c.	n.d.	n.d.	n.d.	n.c.	n.d.	n.d.
Total	3,907	3,041	3,391	3,362	3,043	3,221	3,298	3,044	3,045	3,268	3,133	3,048	3,043	3,040	3,036	3,253	3,050	3,305	3,040
Mg/(Mg+Fe)	0,01	0,33	0,06	0,08	0,28	0,13	0,10	0,31	0,37	0,10	0,19	0,32	0,32	0,27	0,25	0,09	0,41	0,08	0,43
Cr/(Cr+Al)	0,99	0,83	0,97	1,00	0,82	0,86	0,93	0,83	0,83	0,99	0,90	0,83	0,82	0,82	0,82	0,98	0,73	0,90	0,51

Table 4.13: Analyses of magnetite and chromite 1. Sorted by increasing sample numbers. AH = alteration halo, WR = wall rock, D = Domain, ACA = adjacent chromite aggregate, CA = chromite aggregate, n.d. = not detected, n.c. = not calculated. Calculated on 4 oxygens.

4.3.2 Outcrop B

Four samples were cored across one of the major dextral fault zones at subsite B1 (Figure 4.29). The location of the samples relative to the deformation zone is shown in Figure 4.28. The margin of zone (LEKD0312) and the core of the deformation zone (LEKD0112) were chosen for detailed studies.

Two samples were collected from another faultzone (Figure 4.36) of the same fault set at subsite B2 (Figure 4.28) and one of the samples was investigated by optical microscopy and EMP.

Both the examined deformation/breccia zones are part of (subparallel to) the faultzones shown in Figure 4.28.

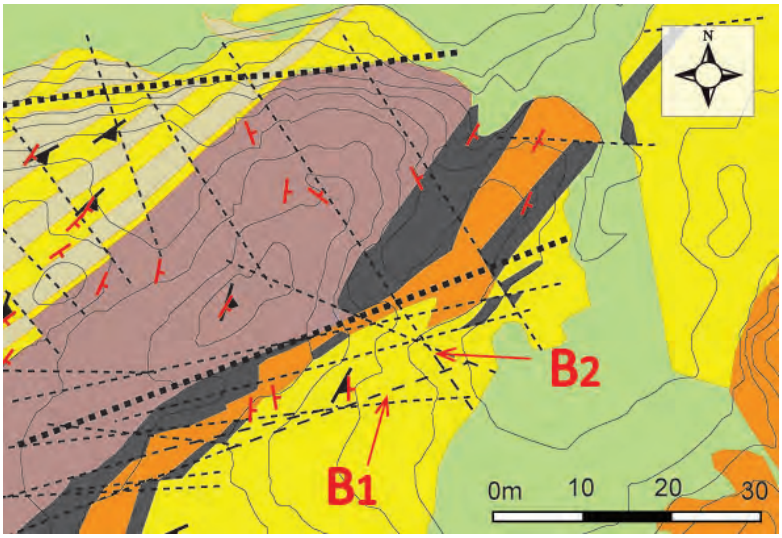

Figure 4.28: Detail of map at locality B. For the complete map please refer to Figure 2.3.

Serpentinized deformation/breccia zone, subsite B1

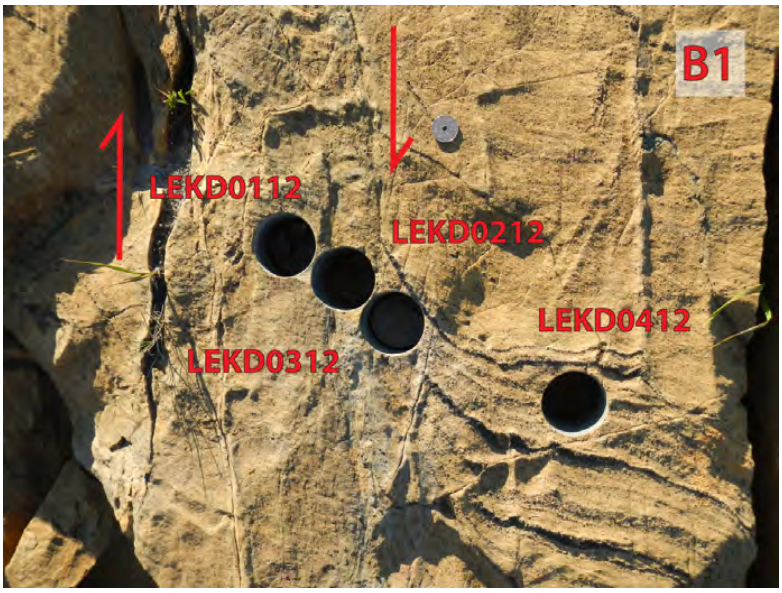

Figure 4.29: Deformation zone at subsite B1 showing location of the cored samples. Note how the chromite layers are dragged into the deformation zone indicating a dextral movement.

Margin of the fault zone
Sample **LEKD0312** was drilled at the margin of the deformation zone zone where the chromite layers start to deflect into the deformation zone (Figure 4.29). The chromite bands are the dominating features of this sample and are seen as the two parallel dark bands running from the upper left to the lower right.

The central band (width 1-2mm) has a particular high density of chromite grains, with sizes up to ∼1mm, giving the band a strong black color. A significantly less dense band accompanies the other band on the upper side. At the down side even weaker bands are still recognizable due to the alignment of the chromite grains.

Another feature is pervasive subperpendicular veins of serpentine (lighter blue interference colors in XPL). These veins resemble the pervasive foliation described in subsection 4.2 on page 58, about dunites in «The layered sequence at Oksetmyrå». A second type of pervasive serpentine veins (darker blue interference colors in XPL) transects the subvertical veins at an angle of ∼40°. The second type of veins does not posses clearly defined vein walls like the first type, but permeates through the rock with a preferred direction parallel to the chromite bands, leaving intensely fragmented olivine and clinopyroxene grains in their paths (Figure 4.32c). They make up a secondary local foliation, aligned with primary layers of chromite. A set of sub-horizontal parallel veins cross-cut the sample in the lower part of Figure 4.30. This set of veins cuts chromite grains.

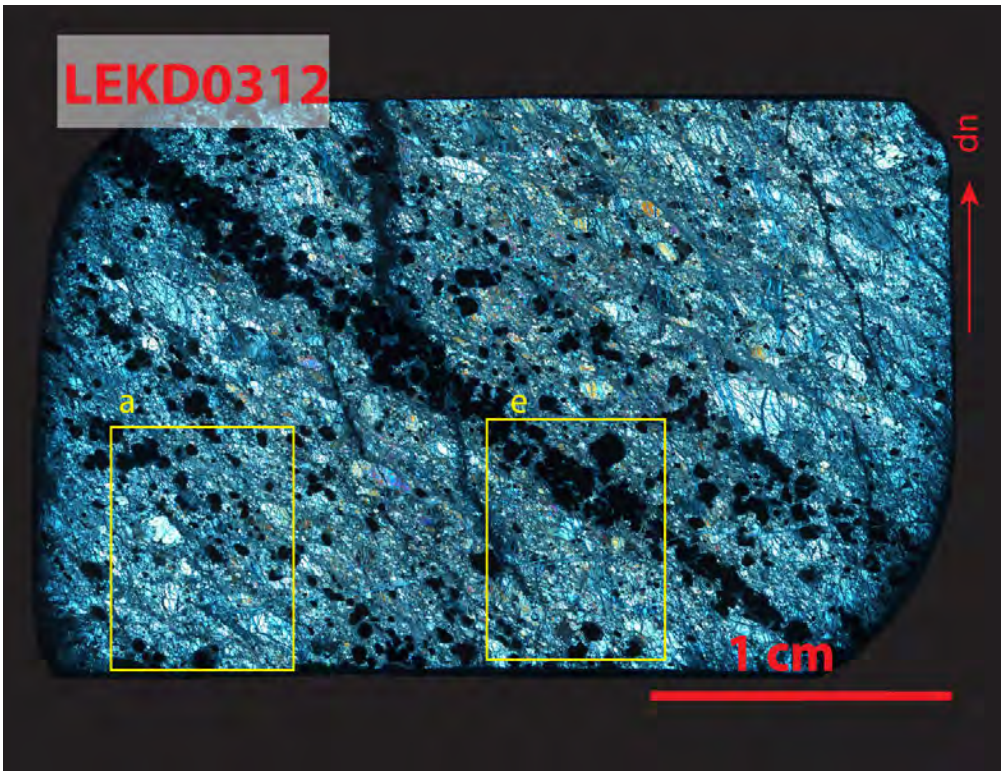

Figure 4.30: Photomerge of thinsection from the margin of the fault zone at subsite B1.

LEKD0312

The modal estimates are: ∼34-40% olivine; ∼45-50% serpentine; ∼3-5% clinopyroxene; and <∼10-12% chromite.

Olivine(Fo91) occur as large and intermediate anhedral porphyroclast (50-400μm) and as fine (10-50μm) to ultra-fine (<10μm) angular clasts. The porphyroclast display strong undulose extinction and are flattened with their long axes orientated parallel to chromite bands and the dominating direction of permeating serpentine.

Olivine analysis no.3 and 5 have higher content of CaO with 2.16wt% and 0.63wt%. These analyzes were taken in a zone of olivine-clinopyroxene intergrowth (Figur 4.32) and must represent a mix between olivine and clinopyroxene.

Serpentine. The highest content of FeO (6.29wt% - analysis no.6) was measured in serpentine dividing a clinopyroxene(cpx) porphyroclast and zone of olivine-clinopyroxene intergrowth (Figure 4.32a).

Clinopyroxene. Three textural types of clinopyroxene were observed in this sample. Larger clinopyroxene(cpx1) grains (up to ∼1mm) with exolution lamellae show locally undulose extinction. A few fibrous grains intergrown with olivine were observed by optical microscope. These are likely of cpx2 type and it has been suggested earlier (subsection 4.1) that these intergrowths probably are replacing orthopyroxene (Figur 4.32).

The clinopyroxene are diopsides with low Na_2O. The highest content of Al_2O_3 (1.45wt%) and Cr_2O_3 (0.98wt%) was measured in cpx1 (both analysis no.1). Three analyses (no.1,

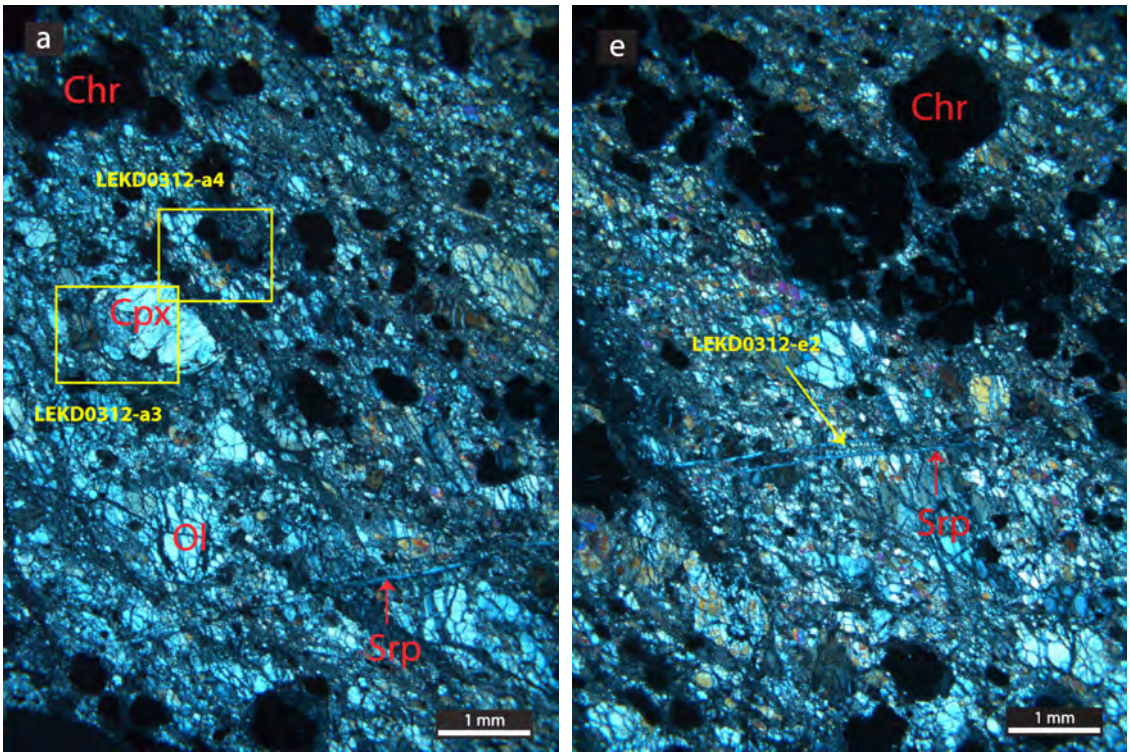

(a) **(b)**

Figure 4.31: (a): Large clinopyroxene porphyroclast in a matrix of serpentine and ultra-fine grained olivine. (b): A parallel set of sub-horizontal veins cross in the lower part of the thin section. Optical microphotographs.

11 and 12) were done in the same grain, where no.11 yielded a content of Al_2O_3 down to 0.26wt% suggesting zonation. No or very low amounts of Al_2O_3 were measured in cpx3.

Chromites are euhedral to anhedral. Some are deformed and may have trails of minute grains. Cr# for chromite vary between 0,51-0,90. Chromite analysis no.28 has a TiO_2 content of 0,75wt%. This chromite is fractured by the subhorizontal parallel serpentine veins (not shown in figure).

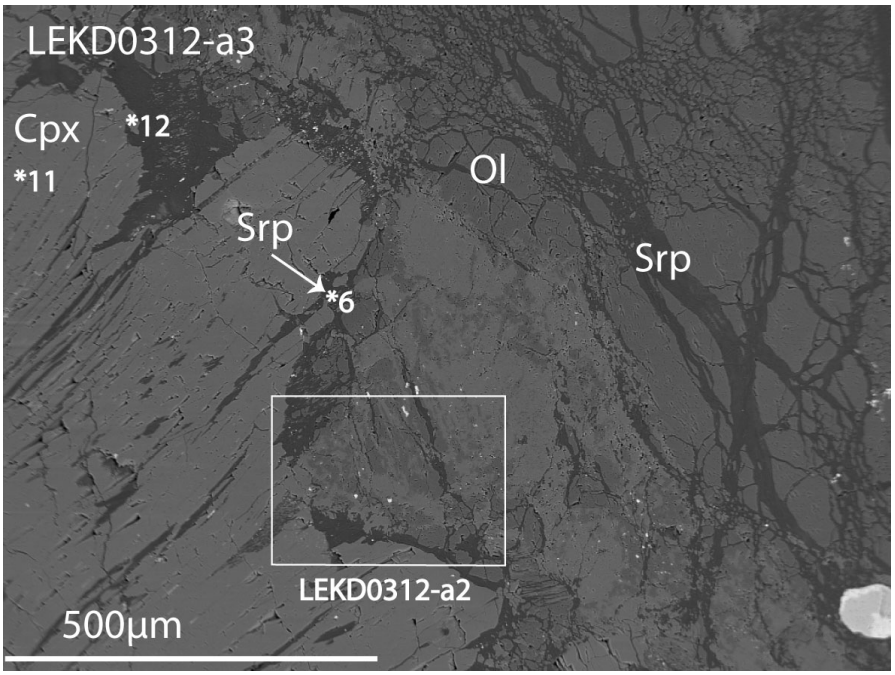

(a)

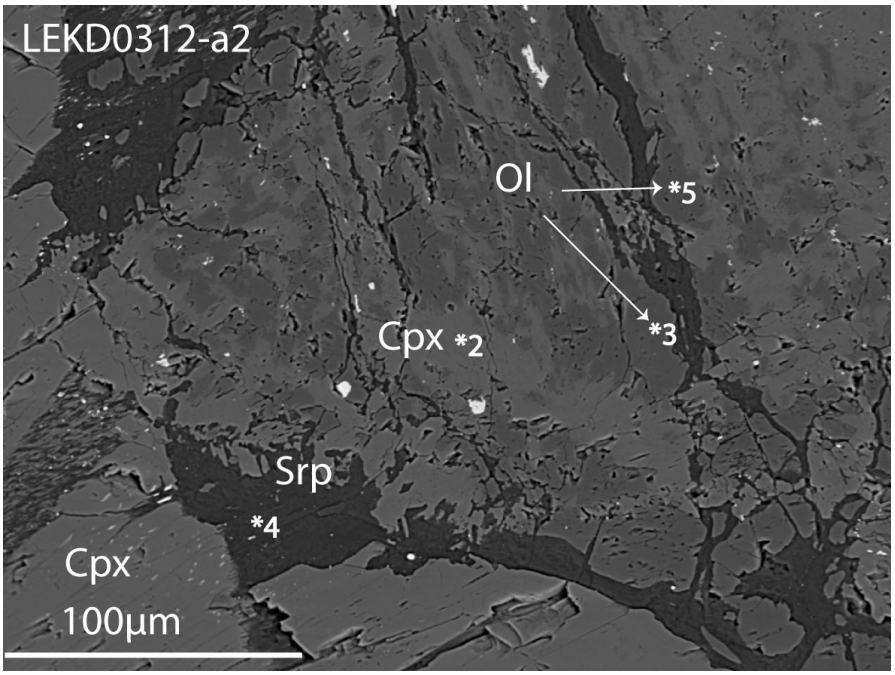

(b)

Figure 4.32: BSE images. Serpentinization of primary clinopyroxene. At the same time secondary clinopyroxene is formed. Secondary clinopyroxene may form of Ca of primary clinopyroxene. White numbers show point for EMP analyses listed in tables 4.14, 4.15 and 4.12. (a): The large clinopyroxene(cpx1) has indented grain boundaries. Between the clinopyroxene and the olivine in the upper right corner, is a zone of olivine-clinopyroxene intergrowth. (b): Detail of olivine-clinopyroxene intergrowth.

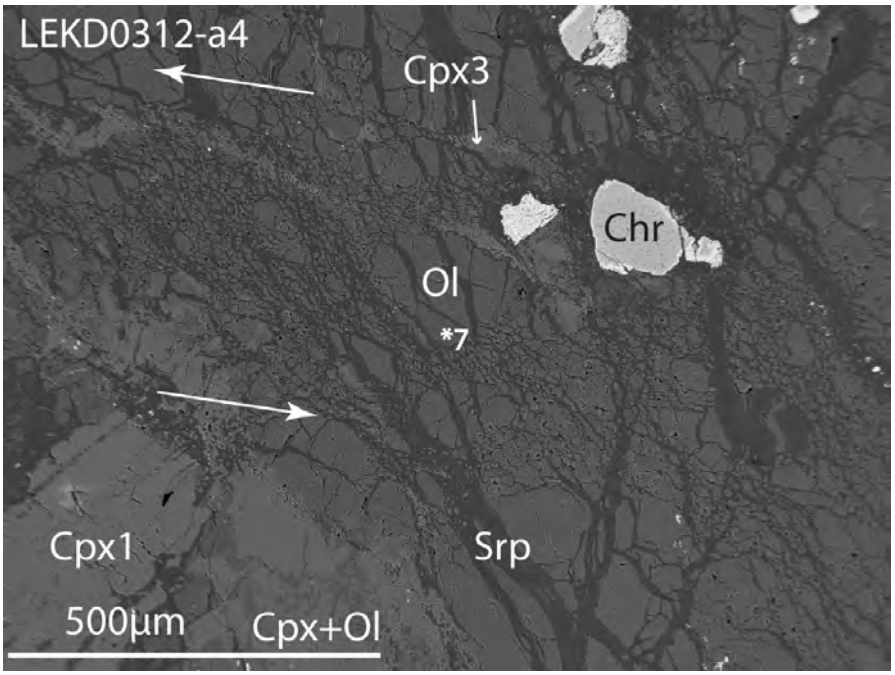

(c)

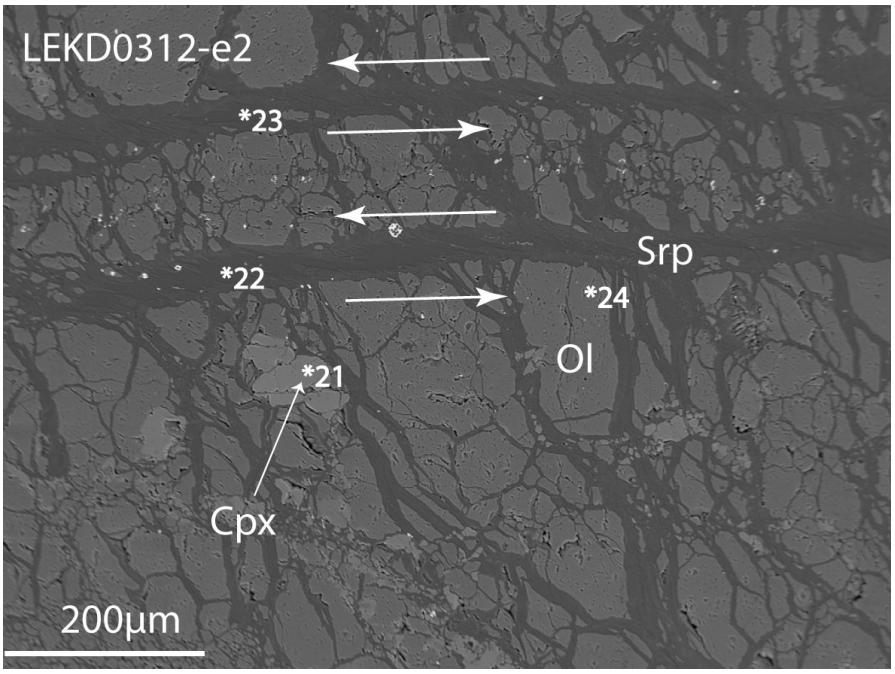

(d)

Figure 4.32: BSE images. White numbers show points for EMP analyses listed in tables 4.14, 4.15 and 4.16. (a): Bands of clinopyroxene(cpx3) along the margin of a zone of intense fragmentation. Oblique permeating veins and bands of clinopyroxene transect the sub-perpendicular pervasive veins indicating a temporal difference. (b): Sub-horizontal parallel serpentine veins offset subvertical serpentine veins. Bands of fine to ultra-fine clinopyroxene(cpx3) follow the sub-horizontal serpentine veins. Fe-oxides are dispersed in the middle of the parallel veins along strike.

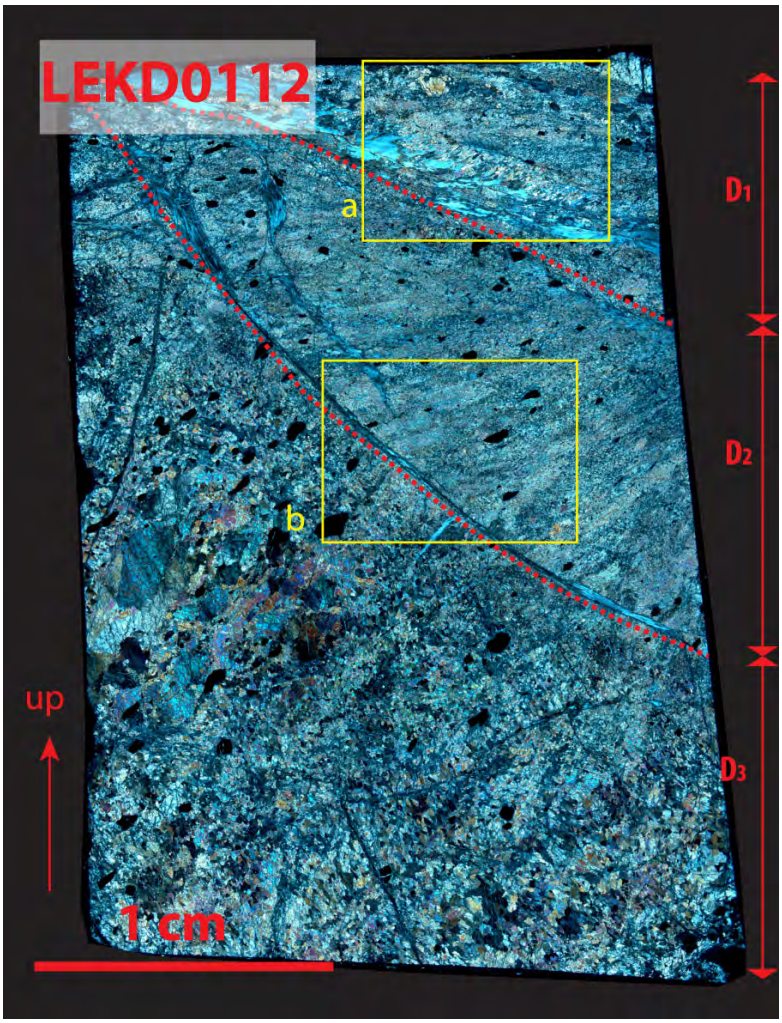

Figure 4.33: Photomerge of thinsection from the central part of the deformation/breccia zone at B1. Three domains that represent different strain are separated by brittle fractures. In the field such distinct domains may reflect blocks in a breccia.

The core of the zone
The sample, **LEKD0112**, which was drilled in the center of the deformation zone, can be divided into different domains displaying different strain. These domains are confined by faults (veins) filled with serpentine (Figure 4.33).

The modal estimates are: ∼50-60% olivine; <3% clinopyroxene; ∼34-44% serpentine; and <3% chromite.

Domain 1. This domain make up the triangle in the upper right part of Figure 4.33. The domain consists at least of two smaller brecciated blocks as judged from the difference in grain sizes and shapes, and the serpentine filled fracture dividing them (Figure 4.34a). In the upper shear zone (Figure 4.34a)olivine occur as ultra-fine/fine (<10-∼50μm) to intermediate (50μm-100mm) clasts.

The lower part of the domain contain an extensional vein filled with fiber grown olivine in a matrix of serpentine. The olivine fibers are bent, which may indicate syntectonic growth of olivine (Figure 4.34a, 4.34d and 4.34e).

Domain 2. A foliation defined by the parallel arrangement of flattened and fragmented olivine grains with similar crystallographic orientation is present within D2. The shape preferred orientation defined by the olivine as also seen by the chrome-spinel grains (Figure 4.33).

In the mylonitic domain (D2), bands of recrystallized olivine grains seem to have an oblique preferred orientation similar to the orientation of the chrome-spinels. A foliation defined by the parallel arrangement of flattened and fragmented olivine grains with similar optical continuity is present within D2 (Figure 4.35a.

Domain 3. This low strain domain has been least subjected to deformation. Large porphyroclasts (up to 0.5cm) show undulose extinction, typical olivine fracturing and lobate grain boundaries. They have inclusions of an unknown material and are covered by a soot-like material assumed to be magnetite. The porphyroclasts have a weak shaped preferred orientation. The domain has zones of small grains that do not seem to have an optical continuity mixed with zones that do.

LEKD0112

Olivine. Analyses of the fibrous olivine from the extensional vein show a slight zonation from Fo in core to Fo in the rim. This is similar to the olivine in the ultramafic rocks studied.

Clinopyroxenes are of two types: Larger (up to 0.5cm in diameter) clinopyroxene(cpx1) grains (Figure **??**), and smaller ($<10\mu$m) clinopyroxene(cpx3) grains that form bands at olivine grain boundaries. Larger clinopyroxene grains, described as cpx1 from outcrop A, occasionally display slightly bent exolution lamellae which is typical for low plasticity deformation. The large clinopyroxene grains are serpentinized (Figure 4.34). Serpentinization releases Ca according to the reaction cpx $\longrightarrow$ srp + CaO. At the same time Ca is consumed and secondary clinopyroxene is formed.

In composition all clinopyroxenes are diopsides with low Na_2O. The highest content of Al_2O_3 (0.59 wt%) and Cr_2O_3 (0.32 wt%) was measured in cpx1, analysis no.30 (Figure 4.34c) in a strained grain.

Chromites are usually subhedral, but is also found as disseminated grains in domain 1 and 2.

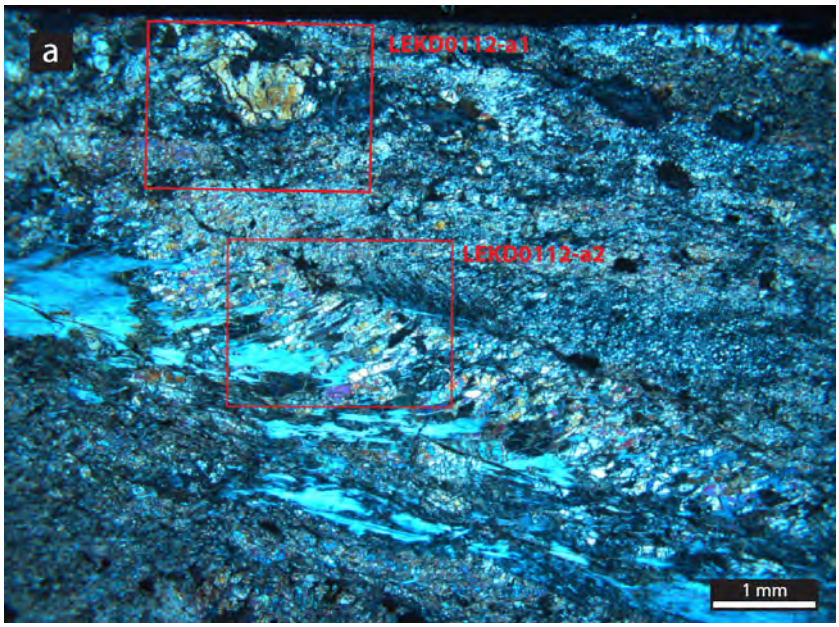

(a)

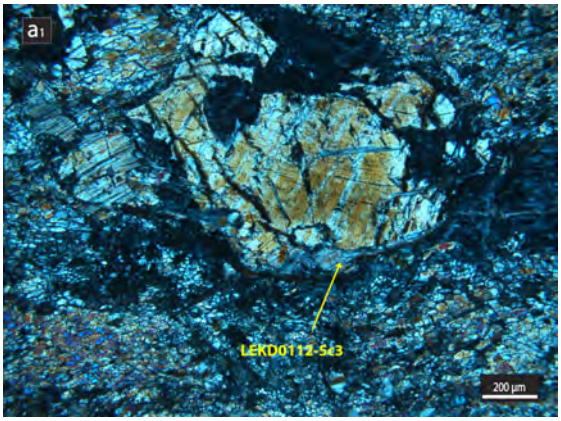

(b)

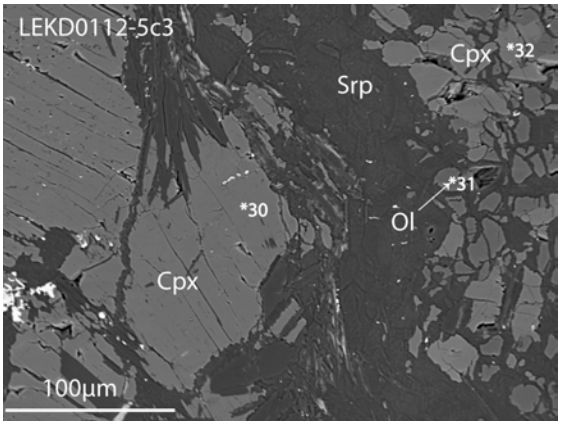

(c)

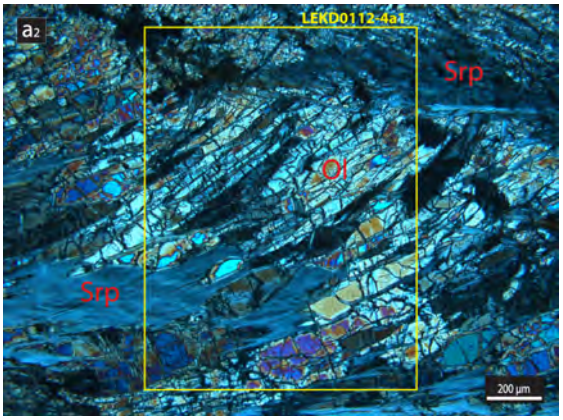

(d)

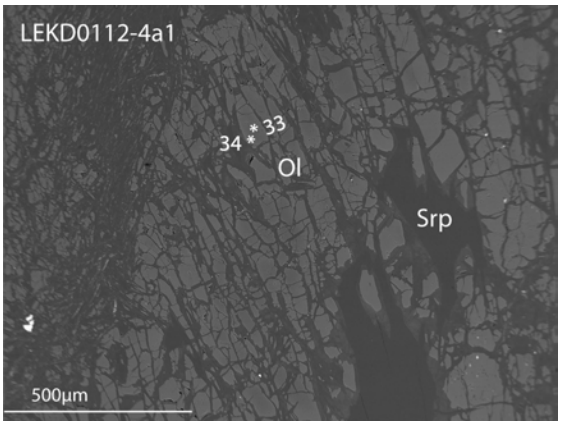

(e)

Figure 4.34: (a): Domain 1 showing an extensional vein. Note growth of fibrous olivine in serpentine. The bending of the fibers suggest syntectonic growth. (b): Clinopyroxene porpyroclast in a matrix of serpentine and very fine grained olivine. (c): BSE image of same motive. Note serpentinization of clinopyroxene. (d): Synkinematic growth of olivine. (e): Synkinematic growth of olivine. Optical microphotographs and BSE images. Note that BSE images are rotated 90 ° clockwise compared to thinsection LEKD0112. White numbers show points for EMP analyses listed in tables 4.14 and 4.15.

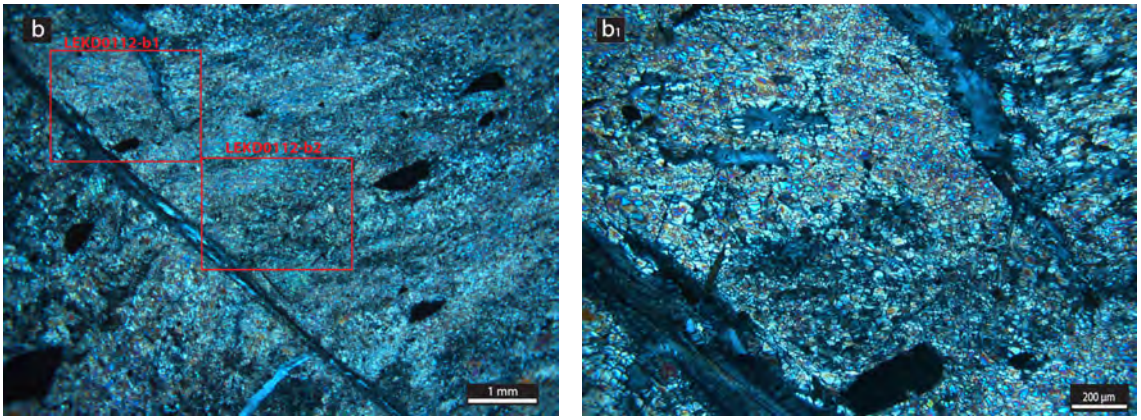

(a) **(b)**

Figure 4.35: (a): The fracture/shear zone transecting the photo define the boundary between domain 2 and 3. Note foliation developed in this high strain zone. Optical microphotograph. (b): The foliation in the high strain zone at the very contact (lower left) is at high angle with the fabric inside domain 2. Optical microphotograph.

The transect across the deformation zone as represented by the wall rock (LEKD0312) and the core (LEKD0112) displays different over all texture. In the wall rock the chromite layers are continuous while the texture of the central part is characterized by the described domains. These domains may have formed by a brecciation and subsequent ductile deformation as the serpentinization increased.

Serpentinized deformation/breccia zone, subsite B2

This deformation zone can be divided into an anastomosing part (LEKD0512) and a brecciated part (LEKD0612). Only LEKD0512 was investigated by EMP.

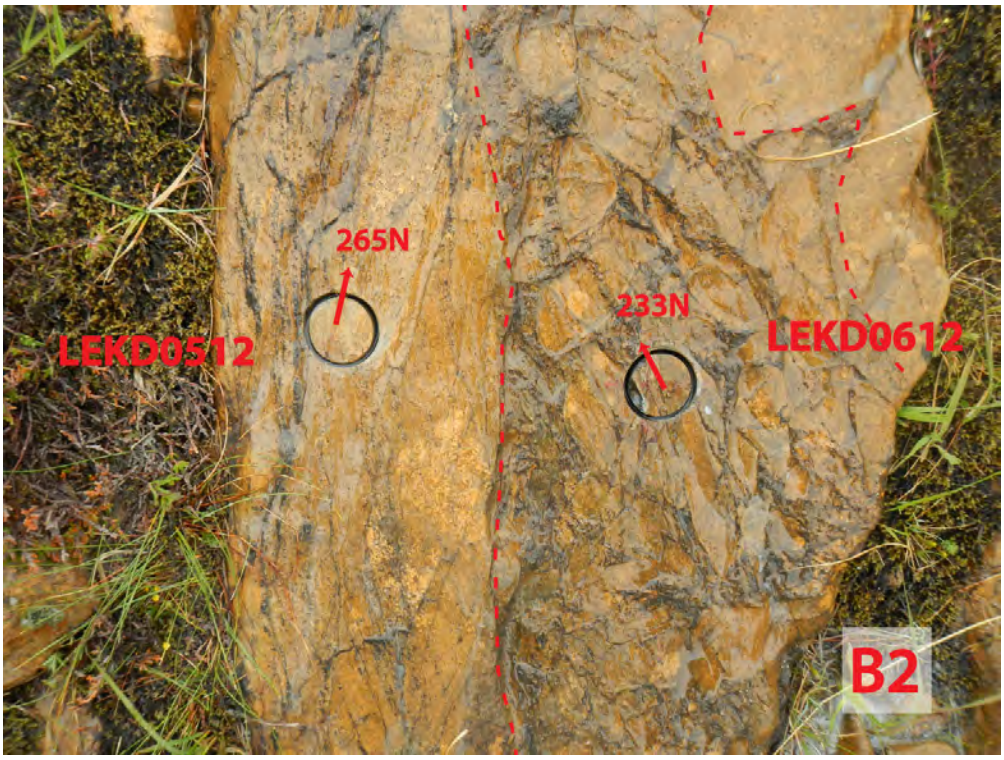

Figure 4.36: Field relation showing fault/deformation zone at subsite B2. The breccia with angular fragments to the right is developed into a shear zone at the left.

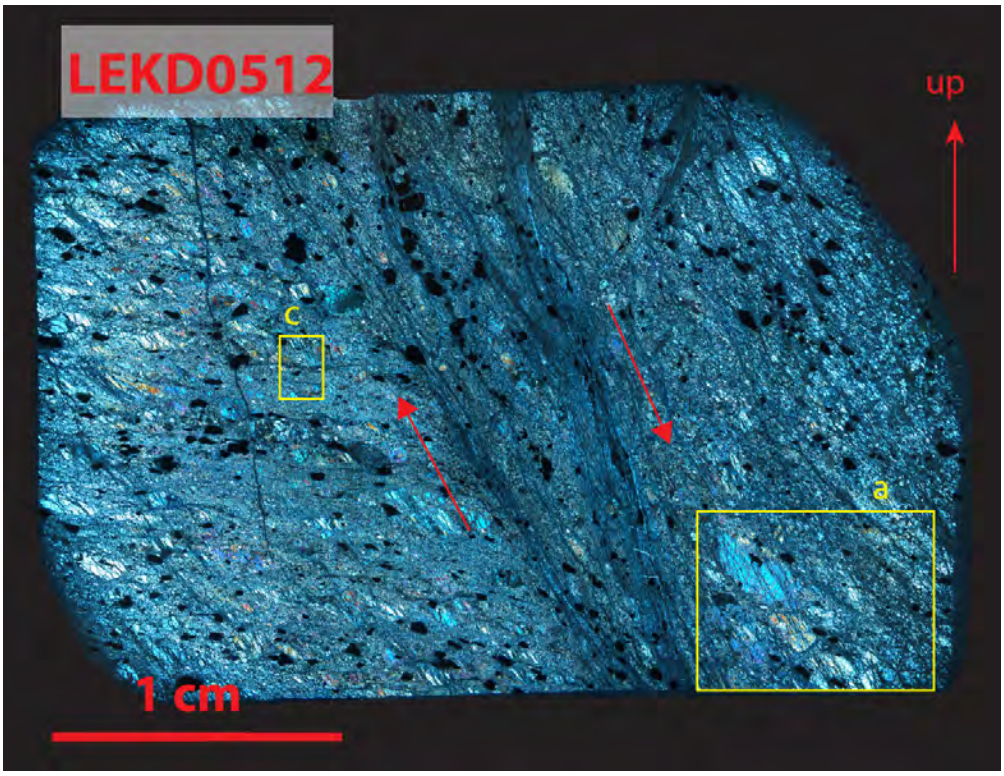

Figure 4.37: Photomerge of LEKD0512 .

Sample LEKD0512 was collected from a strongly sheared and serpentinized part of the deformation zone at the main fault at locality B (described in subsection 2.2.4). The central part of the sample is cut by a ductile shear zone. The olivine adjacent to the central shear zone (Figure 4.37) displays serpentine filled fractures parallel to the shear zone, suggesting that the olivine reacted by brittle failure while the strongly serpentinized core deformed in a ductile way.

In addition to the serpentine filled fractures running parallel to the shear zone seen in Figure 4.37, the wall rock is characterized by a banding/foliation at an high angle to the shear zones as seen in Figure 4.39a.

LEKD0512

The modal estimates are: ∼35-45% olivine; ∼45-55% serpentine; <4% clinopyroxene; and <4% chromite.

Olivine occurs as flattened grains cut by serpentine veins.

Serpentine probably contains small amounts of ferro brucite. Brucite is a very weak mineral and thus takes up most of the deformation. Although brucite can not be confirmed by EMP it can not be excluded either.

Clinopyroxenes observed are either primary clinopyroxene porphyroclasts or secondary clinopyroxenes(cpx3) forming bands along deformation zones (Figure 4.39b).

Chromite is euhedral to anhedral. They are dragged into the ductile deformation zone

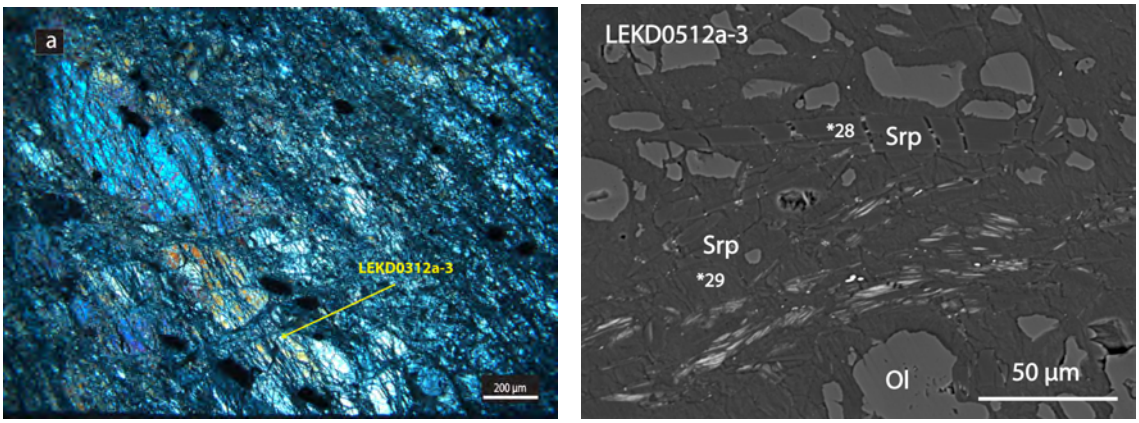

(a) **(b)**

Figure 4.38: Textural relationships from inset a. BSE images showing intense microshear zones. The amount of olivine is reduced relative to serpentine in these zones. The bright phase on the BSE image is similar to ferroan brucite in composition. White numbers show points for EMP analyses listed in table 4.16.

where their orientation align with the strong foliation. Locally chromites have tails of micrograins sub-perpendicular to the foliation (Figure reffig:LEKD0512XPLx2-5-a1.

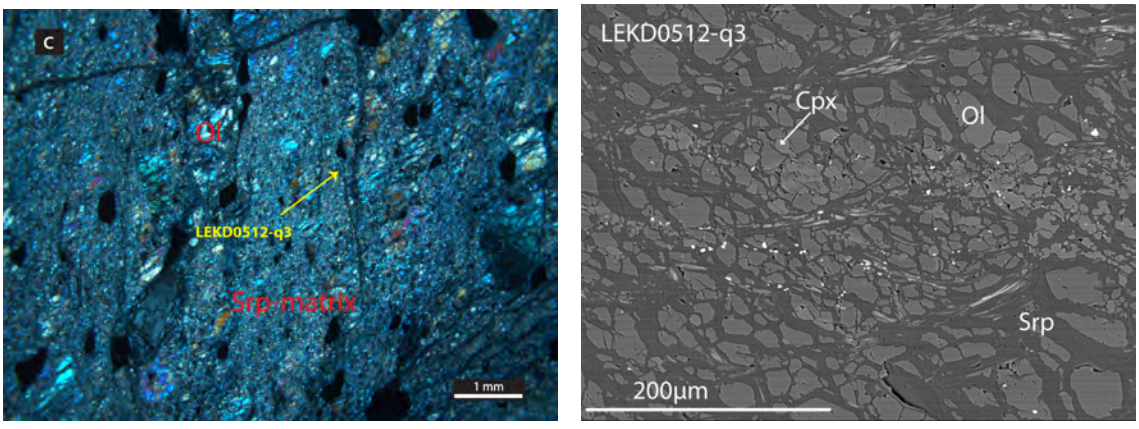

(a) **(b)**

Figure 4.39: (a): Serpentine veins open up between ultra mylonitic zones. (b): There is a tremendously focused deformation in this anastomosing shear zone, where the foliation is dragged into the shear zone at both sides . In the middle of this shear zone, bands of clinopyroxene(cpx3) are formed. An unknown material that looks like a layer silicate is developed in the microshear zone. Optical microphotograph and BSE image.

Sample: LEKD	0112	0112	0112	0112	0112	0112	0312	0312	0312	0312	0312	0312	0312	0312	0512	0512
Analysis #	31	33	34	36	38	41	3	5	7	8	13	14	16	24	25	27
Mineral	Ol	Ol	Ol	Ol	Ol	Ol	Ol/Cpx	Ol/Cpx	Ol	Ol	Ol	Ol	Ol	Ol	Ol	Ol
Comment	D1	D1 Fibers	D1 Fibers	D2 IG	D2 IG	D1	IG	IG			Med	Fine		PSV	Fine	Med
[wt.%]																
SiO_2	41,33	41,49	40,28	41,46	40,70	41,02	42,30	41,22	40,42	41,01	41,12	40,91	42,06	40,19	40,32	40,09
TiO_2	n.d.	n.d.	0,03	0,01	n.d.	n.d.	0,06	0,05	n.d.	0,01	n.d.	n.d.	n.d.	n.d.	0,01	n.d.
Al_2O_3	n.d.	0,01	0,05	0,03	n.d.	0,03	0,03	0,02	0,01	n.d.	0,01	0,01	0,03	0,01	0,02	n.d.
Cr_2O_3	0,02	n.d.	n.d.	n.d.	n.d.	0,01	0,07	0,06	0,01	0,01	0,01	0,01	0,02	n.d.	n.d.	n.d.
FeO(tot)	9,48	7,08	9,46	9,06	9,62	9,28	7,62	7,87	8,83	8,33	9,30	9,22	7,97	7,65	8,95	8,82
NiO	0,27	0,04	0,28	0,25	0,17	0,17	0,16	0,14	0,19	0,26	0,34	0,34	0,31	0,17	0,27	0,15
MgO	49,77	51,72	49,46	50,23	49,32	49,08	48,32	49,55	49,65	49,95	50,79	49,49	51,06	50,92	50,14	49,64
MnO	0,10	0,02	0,13	0,12	0,06	0,10	0,14	0,14	0,16	0,11	0,17	0,24	0,16	0,06	0,21	0,20
CaO	0,14	0,08	n.d.	0,15	0,14	n.d.	2,16	0,63	0,07	0,02	0,02	0,14	0,01	0,00	0,04	0,03
Na_2O	n.d.	n.d.	n.d.	0,01	n.d.	0,01	0,02	n.d.	n.d.	n.d.	0,01	n.d.	n.d.	n.d.	n.d.	n.d.
K_2O	n.d.	n.d.	0,02	n.d.	n.d.	n.d.	n.d.	n.d.	n.d.	n.d.	n.d.	0,01	n.d.	0,01	0,02	n.d.
Total	101,10	100,44	99,70	101,32	100,01	99,71	100,88	99,68	99,34	99,70	101,75	100,37	101,62	98,99	99,98	98,93
Si	1,000	0,999	0,990	1,000	0,997	1,005	1,020	1,005	0,994	1,002	0,990	0,998	1,005	0,987	0,987	0,991
Ti	n.d.	n.d.	n.c.	n.c.	n.d.	n.d.	0,001	0,001	n.d.	n.c.	n.d.	n.d.	n.d.	n.d.	n.c.	n.d.
Al	n.d.	n.c.	0,001	0,001	n.d.	0,001	0,001	n.c.	n.c.	n.d.	n.c.	n.c.	0,001	n.c.	0,001	n.d.
Cr	n.c.	n.d.	n.d.	n.d.	n.d.	n.c.	0,001	0,001	n.c.	n.c.	n.c.	n.c.	n.c.	n.d.	n.d.	n.d.
Fe	0,192	0,143	0,194	0,183	0,197	0,190	0,154	0,161	0,182	0,170	0,187	0,188	0,159	0,157	0,183	0,182
Ni	0,005	0,001	0,005	0,005	0,003	0,003	0,003	0,003	0,004	0,005	0,007	0,007	0,006	0,003	0,005	0,003
Mg	1,796	1,856	1,813	1,805	1,801	1,793	1,738	1,802	1,821	1,818	1,822	1,800	1,819	1,864	1,830	1,828
Mn	0,002	n.c.	0,003	0,002	0,001	0,002	0,003	0,003	0,003	0,002	0,003	0,005	0,003	0,001	0,004	0,004
Ca	0,004	0,002	n.d.	0,004	0,004	n.d.	0,056	0,017	0,002	0,001	n.c.	0,004	n.c.	n.c.	0,001	0,001
Na	n.d.	n.d.	n.d.	n.c.	n.d.	0,001	0,001	n.d.	n.d.	n.d.	n.c.	n.d.	n.d.	n.d.	n.d.	n.d.
K_2O	n.d.	n.d.	0,001	n.c.	n.d.	n.d.	n.d.	n.d.	n.d.	n.d.	n.d.	n.c.	n.d.	n.c.	0,001	n.d.
Total	2,999	3,001	3,009	3,000	3,003	2,995	2,978	2,993	3,006	2,998	3,010	3,002	2,994	3,013	3,013	3,009
Mg/(Mg+Fe)	0,90	0,93	0,90	0,91	0,90	0,90	0,92	0,92	0,91	0,91	0,91	0,91	0,92	0,92	0,91	0,91

Table 4.14: Analyses of olivine, part 6. Sorted by increasing sample numbers. D = domain, PSV = parallel serpentine vein, IG = zone of olivine and clinopyroxene intergrowth, Fine = fine grain size, Med = medium grain size, n.d. = not detected, n.c. = not calculated. Calculated on 4 oxygens.

Sample:LEKD		0112	0112	0112	0112	0112	0112	0312	0312	0312	0312	0312	0312	0312	0312
	Analysis #	30	32	35	37	39	40	1	2	9	10	11	17	21	25
	Mineral	Cpx1	Cpx1	Cpx1	Cpx1	Cpx1	Cpx1	Cpx1	Cpx2	Cpx2	Cpx2	Cpx1	Cpx1	Cpx3	Cpx1
	Comment	D1	D1	D3	D3	D3	D1	-	IG	IG	IG	-	-	PSV	-
SiO_2	54,59	54,17	54,50	55,05	54,98	55,24	54,12	54,74	54,94	54,32	55,78	54,11	54,13	55,23	55,17
TiO_2	0,06	0,02	0,06	0,02	0,01	0,07	0,08	0,04	0,04	0,02	0,04	0,09	0,08	0,01	0,09
Al_2O_3	0,59	0,42	0,45	0,32	0,34	0,47	1,45	0,27	0,29	0,36	0,26	1,01	1,14	0,00	0,55
Cr_2O_3	0,32	0,19	0,17	0,16	0,15	0,12	0,98	0,19	0,22	0,24	0,11	0,71	0,73	0,02	0,18
FeO(tot)	1,49	1,57	1,45	1,45	1,45	1,39	1,61	0,73	1,39	1,10	1,48	1,62	1,69	1,14	1,53
MnO	0,11	0,05	0,05	0,03	0,10	0,08	0,08	0,03	0,06	0,02	0,04	0,07	0,03	0,07	0,09
MgO	17,96	17,92	17,94	17,98	18,07	17,93	17,65	18,61	18,34	18,13	18,06	17,27	17,54	17,97	17,94
NiO	0,01	0,03	0,01	0,00	0,00	0,00	0,08	0,03	0,06	0,06	0,04	0,03	0,02	0,05	0,09
CaO	25,62	25,08	25,58	25,43	26,16	25,38	24,22	26,05	25,81	25,66	25,31	25,22	24,61	26,18	25,36
Na_2O	0,08	0,06	0,12	0,09	0,11	0,06	0,25	0,07	0,13	0,03	0,13	0,15	0,21	0,00	0,11
K_2O	0,00	0,00	0,00	0,00	0,00	0,00	0,00	0,00	0,00	0,00	0,00	0,01	0,01	0,00	0,00
SUM	100,83	99,51	100,34	100,52	101,39	100,74	100,51	100,75	101,30	101,24	100,29	92,62	100,17	100,67	101,10
mg#	95,5	95,3	95,7	95,7	95,7	95,8	95,1	97,8	95,9	96,7	95,6	95,0	94,9	96,6	95,4
Si	1,962	1,972	1,966	1,983	1,964	1,987	1,953	1,961	1,962	1,966	1,996	1,960	1,960	1,988	1,978
Al IV	0,025	0,018	0,019	0,013	0,014	0,013	0,047	0,011	0,012	0,015	0,004	0,040	0,040	0,000	0,022
Al VI	0,000	0,000	0,000	0,000	0,000	0,007	0,014	0,000	0,000	0,000	0,007	0,003	0,008	0,000	0,001
Ti	0,002	0,001	0,002	0,001	0,000	0,002	0,002	0,001	0,001	0,001	0,001	0,002	0,002	0,000	0,002
Cr	0,009	0,005	0,005	0,004	0,004	0,003	0,028	0,005	0,006	0,007	0,003	0,020	0,021	0,001	0,005
Fe3+	0,022	0,018	0,024	0,010	0,030	0,001	0,009	0,022	0,032	0,024	0,000	0,011	0,010	0,012	0,009
Fe2+	0,022	0,030	0,019	0,034	0,013	0,040	0,039	0,000	0,009	0,010	0,044	0,038	0,041	0,023	0,037
Mn	0,003	0,002	0,002	0,001	0,003	0,002	0,003	0,001	0,002	0,001	0,001	0,002	0,001	0,002	0,003
Mg	0,962	0,972	0,965	0,966	0,962	0,961	0,949	0,993	0,976	0,978	0,963	0,933	0,947	0,964	0,959
Ni	0,000	0,001	0,000	0,000	0,000	0,000	0,002	0,001	0,002	0,002	0,001	0,001	0,001	0,001	0,002
Ca	0,987	0,978	0,989	0,982	1,001	0,978	0,936	1,000	0,988	0,995	0,970	0,979	0,955	1,009	0,974
Na	0,006	0,004	0,009	0,006	0,008	0,004	0,017	0,005	0,009	0,002	0,009	0,011	0,014	0,000	0,007
ox	5,978	5,982	5,976	5,990	5,970	5,999	5,991	5,967	5,968	5,976	6,000	5,989	5,990	5,988	5,991
Al total	0,025	0,018	0,019	0,013	0,014	0,020	0,062	0,011	0,012	0,015	0,011	0,043	0,048	0,000	0,023
Fe tot	0,045	0,048	0,044	0,044	0,043	0,042	0,048	0,022	0,042	0,033	0,044	0,049	0,051	0,034	0,046
Fe3+	0,022	0,018	0,024	0,010	0,030	0,001	0,009	0,033	0,032	0,024	0,000	0,011	0,010	0,012	0,009
Di+Hd	0,960	0,959	0,970	0,968	0,984	0,964	0,888	0,988	0,975	0,980	0,966	0,939	0,916	1,007	0,952
En+Fs	0,012	0,022	0,007	0,016	-0,004	0,019	0,050	0,003	0,005	0,004	0,021	0,016	0,619	-0,010	0,022

Table 4.15: Analyses of clinopyroxene at outcrop B. Sorted by increasing sample numbers. D = domain, IG = zone of olivine and clinopyroxene intergrowth, PSV = adjacent parallel serpentine vein. Structural formula according to Neumann (1976)

Sample: LEKD	0112	0312	0312	0312	0312	0312	0512	0512	0512	0512	0512	0512	0512
Analysis #	42	4	6	22	23	27	26	28	29	30	31	32	33
Mineral	Srp	Srp	Srp	Srp	Srp	Srp	Srp	Srp	Srp	Srp	Srp	Srp	Srp
Comment	D1	IG	IG	PSV	PSV	-	Matrix	Tab	Matrix	Tab	Matrix	Matrix	Tab
[wt.%]													
SiO_2	38,40	38,14	35,74	38,43	38,48	37,56	38,87	43,07	36,28	43,74	39,14	40,18	42,32
TiO_2	0,02	0,01	0,02	n.d.	0,01	0,01	0,02	0,01	n.d.	n.d.	n.d.	n.d.	n.d.
Al_2O_3	5,03	3,04	0,08	3,83	4,37	7,81	0,04	0,80	0,05	0,37	0,04	0,07	1,71
Cr_2O_3	1,97	0,93	0,01	0,93	1,18	1,48	n.d.	0,04	0,03	0,14	0,02	n.d.	0,93
FeO(tot)	2,85	3,52	6,29	2,68	2,63	2,50	3,76	2,73	5,38	2,67	4,16	5,44	2,25
NiO	0,02	0,12	0,22	n.d.	n.d.	0,05	0,27	0,12	0,34	0,10	n.d.	n.d.	0,08
MgO	38,11	39,10	40,44	38,39	37,86	37,46	40,52	39,02	39,45	39,90	38,87	37,79	39,31
MnO	0,06	0,10	0,10	0,04	0,06	n.d.	0,07	n.d.	0,18	0,03	0,18	0,10	0,06
CaO	0,02	0,17	0,16	0,04	0,07	0,01	n.d.	0,04	0,08	0,01	n.d.	0,03	n.d.
Na_2O	0,03	n.d.	n.d.	n.d.	0,02	0,05	0,01	n.d.	n.d.	n.d.	n.d.	n.d.	n.d.
K_2O	n.d.	0,02	n.d.	0,01	0,01	0,01	n.d.	n.d.	n.d.	n.d.	0,02	n.d.	n.d.
Total	86,51	85,14	83,07	84,36	84,69	86,94	83,55	85,84	81,78	86,96	82,42	83,60	86,66
Si	1,824	1,849	1,817	1,864	1,859	1,768	1,920	2,034	1,861	2,039	1,958	1,988	1,983
Ti	0,001	n.c.	0,001	n.d.	n.c.	n.c.	0,001	n.c.	n.d.	n.d.	n.d.	n.d.	n.d.
Al	0,282	0,173	0,005	0,219	0,249	0,433	0,002	0,044	0,003	0,020	0,002	0,004	0,095
Cr	0,074	0,036	0,001	0,036	0,045	0,055	0,000	0,002	0,001	0,005	0,001	n.d.	0,034
Fe	0,113	0,143	0,268	0,109	0,106	0,098	0,155	0,108	0,231	0,104	0,174	0,225	0,088
Ni	0,001	0,005	0,009	n.d.	n.d.	0,002	0,011	0,005	0,014	0,004	n.d.	n.d.	0,003
Mg	2,698	2,826	3,066	2,776	2,726	2,628	2,985	2,748	3,016	2,773	2,898	2,787	2,747
Mn	0,002	0,004	0,004	0,002	0,002	n.d.	0,003	n.c.	0,008	0,001	0,008	0,004	0,003
Ca	0,001	0,009	0,009	0,002	0,004	0,001	n.d.	0,002	0,005	n.c.	n.d.	0,001	n.d.
Na	0,003	n.d.	n.d.	n.d.	0,002	0,004	0,001	n.d.	n.d.	n.d.	n.d.	n.d.	n.d.
K	n.d.	0,001	n.d.	0,001	0,001	0,001	n.d.	n.d.	n.d.	n.d.	0,001	n.d.	n.d.
Total	4,999	5,047	5,179	5,009	4,995	4,990	5,078	4,943	5,137	4,948	5,041	5,010	4,952
Mg/(Mg+Fe)	0,96	0,95	0,92	0,96	0,96	0,96	0,95	0,96	0,93	0,96	0,94	0,93	0,97

Table 4.16: Analyses of serpentine, part 3. D = domain, IG = intergrowth between olivine and clinopyroxene, PSV = adjacent parallel vein, Tab = tabular/angular grain shape. Sorted by increasing sample numbers. n.d. = not detected, n.c. = not calculated. Calculated on 7 oxygens.

4.4 Summary

Composition of clinopyroxene

The clinopyroxenes were plotted in a pyroxene classification diagram. See caption for comments.

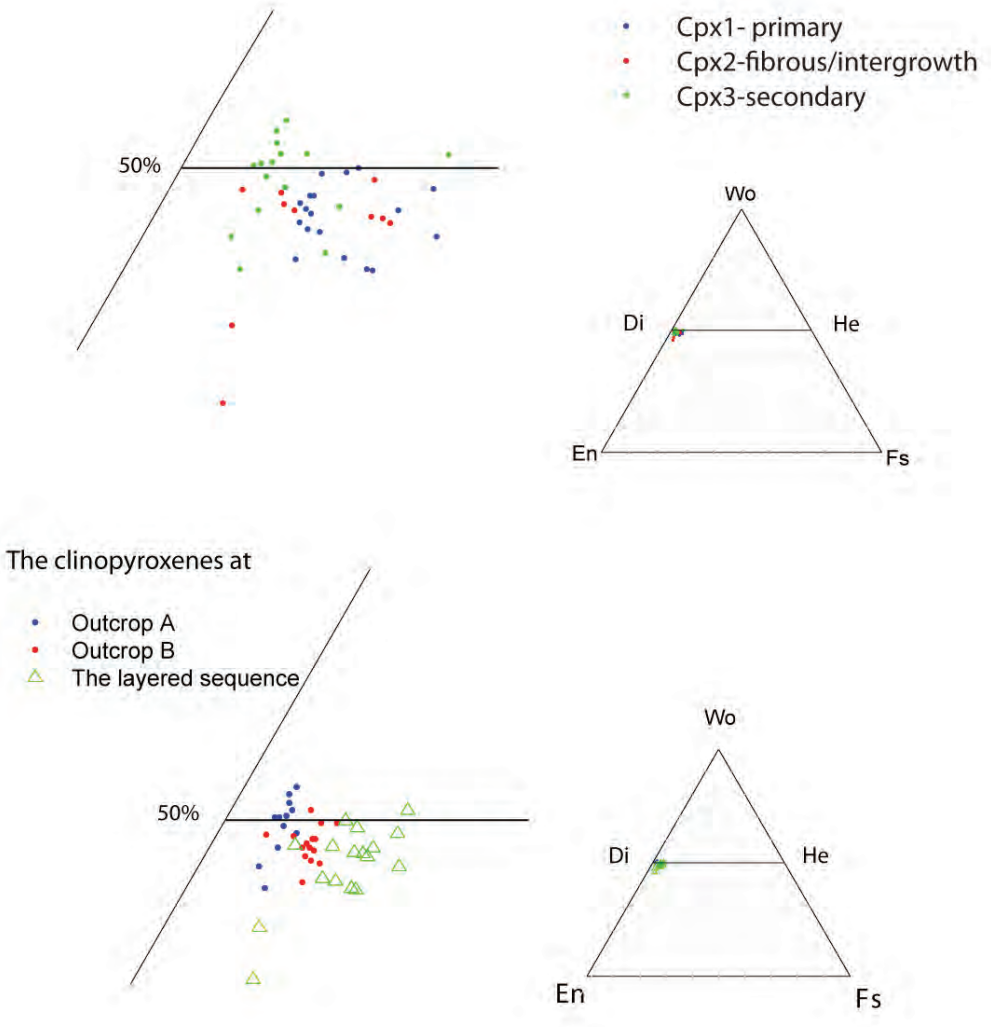

Figure 4.40: Details from the pyroxene classification diagram. All clinopyroxenes are diopsides. It has to be noted that the division into cpx1, 2 and 3 is based on textural observations. Upper: The plot shows that cpx 1 has slightly higher Hedenbergite component, while the Ca-content show no systematic difference. In general cpx2 vary more than cpx1 with respect to Hedenbergite component and Ca-content. The difference might reflect whether the clinopyroxene replaced olivine or orthopyroxene. Lower: The plot shows the distribution of the same clinopyroxenes as in the upper diagram across the locality. The distribution may reflect variations in the mineral chemistry of the different lithologies. The largest variation is found in the layered sequence which may be due to larger intersecting faults and fractures allowing transport of element loaded fluids between the different lithologies.

Petrography of deformation zones.

The petrography of the deformation zones at both outcrop A and fault zones at outcrop B reveals that the serpentinization increases and plays an important part in the evolution of the deformation zones. Simultaneously with the increase in serpentine, the amount of the primary phases and their grain sizes are reduced.

There is indication that the process started with brittle deformation as represented by breccia zones. The breccias are locally seen to develop into ductile shear zones where the fragments from the breccias are found strongly serpentinized in elongated domains.

The increase in serpentine suggests that the deformation zones are sites of fluid-transport. The bands of secondary clinopyroxene following the high strain zones suggest that Ca also was transported along the high strain zones.

It is further noticed that while the primary phases of olivine and clinopyroxene are consumed by serpentinization, they are also formed in the process of hydration and deformation. The reason for this is unclear and may be due to:

- that the strained old grains are unstable and replaced by new strain free grains
- the temperature changed during the process
- the fluid composition changed

Chapter 5

Summary and Discussion

5.1 Summary and Discussion

Metamorphic events are characterized by the growth of metamorphic minerals reflecting varying PT conditions, and they often coincide approximately with periods of deformation (Passchier and Trouw, 2005).

How to hydrate a dry rock?

The rocks of Leka are differently serpentinized. According to Iyer et al. (2008a) is ∼ 60% of the olivine in the dunites serpentinized.

A central issue associated with the hydration of rocks is by which mechanism(s) fluids get access to, what in principle is, an impermeable and dry rock (protolith) to allow a reaction between the fluid and the rock to take place. In the case of serpentinization two mechanisms have been suggested[1]:

- Reaction-induced fracturing (Iyer et al., 2008b; Jamtveit et al., 2009; Plümper et al., 2012b)
- Fracturing related to tectonism

Mid-ocean ridges are known as extensional tectonic environments, where the zone of active deformation may extend to 15 km from the ridge axis. Major earthquakes are uncommon along mid-ocean ridges, however, associated transform faults are often the site of large magnitude earthquakes (Fowler, 2008).

The hydrothermal circulation at mid-ocean ridges is vigorous (Fowler, 2008) and a third mechanism is therfore suggested:

- Thermal fracturing (cooling)

Observations at Leka

The studied rocks on Leka are ultramafic in composition and comprises: Dunite with bands of chromite, clinopyroxenite, chromite-rich clinopyroxenite and wehrlite. Field observations and detailed geological mapping reveal that the investigated rocks at Oksetmyrå, underwent intense deformation and hydration.

While the dunites and clinopyroxenites are moderately serpentinized (∼40-55%), the wehrlite contains less serpentine (∼15%) and the chromite-rich clinopyroxenite only minor amounts.

Serpentine occur as matrix mineral and as fault/vein networks forming small ridges at the surface and as cross-fiber serpentine in en échelon fractures. The latter might indicate rotation, while the fault/vein network may be a precurser for brecciated deformation zones. It is also observed that the serpentinization increases in relation to deformation zones, which suggest that such zones may provide pathways for element loaded fluids.

[1]The mechanisms are discussed later in this chapter.

Numerous smaller (mm-cm scale) faults and fault networks are present. Outcrop B is additionally cross-cut by two larger fault sets displacing cumulate layers. Both sets are at high angles to the cumulate layering.

The dunites also display discontinuous NE-SW to EW trending deformation zones. These may include thin semi-parallel mylonite zones, breccia and shear zones, and small scale fractures with alteration zones (micro shear zones). Some of the larger deformation zones are related to mylonites and their development may be attributed to continued shearing.

The studied rocks at Oksetmyrå form part of the layered crustal sequence of LOC. Compositionally they are not much different from rocks constituting the oceanic mantle. Research from the mantle section (harzburgite) show that the harzburgites display many of the same deformation structures as outlined above. For instance did Austrheim and Prestvik (2008) observe several 0.5 m thick E-W trending shear zones which could be followed for more than 100 meters. I therefore assume that my findings also apply to the mantle part.

My maps and observations document that the layered sequence at Oksetmyrå is highly deformed with development of penetrative serpentine foliation, a dense set of NE-SW to EW fault zones, some with displacements of several meters. Mylonite and breccia zones are located along these sets of faults. Complex damage zones as illustrated in Figure 2.26b may reflect the interaction between the damage zones and faults.

The textural observations imply that these zones are sites of fluid flow and element transport.

Development of Regional Foliation

The penetrative NE-SW trending foliation in dunite is subparallel to the layering. The very fine lines that constitutes the foliation are, on the microscale, sinuous serpentine veins alternating with elongated areas of fine-grained olivine in a serpentine matrix. The elongation is parallel with veins crosscutting larger olivine porphyroclast. The elongation might be due to the softer matrix material (serpentine) which has reacted ductily, while the porphyroclast reacted by brittle fracturing thus facilitating the formation of sinuous veins cutting the porphyroclast. A similar texture was described by Varne and Brown (1978) who observed strips of thin lenticular banding defined by contrasting olivine grain sizes in thinsections from the Adamsfield Ultramafic Complex, Tasmania.

The foliation may have developed through two interacting steps: Permeating fluids entered weaker parts of the rock which resulted in the formation of matrix serpentine. Volume increase following serpentinization fractured the still brittle parts of the rock (large porphyroclasts). The fractures were then subsequently or simultaneously in an iterative process filled with serpentine formed from matrix serpentine. This is the case of reaction-induced fracturing.

In the field the foliation disappears in deformation/breccia zones and are cross-cut by mylonite zones. At alteration zones around central fractures (microshear zones) the foliation seems to continue at the other side of the zone without displacement. These crosscutting relationships indicate that the rock was foliated when the deformation zones developed, which again indicates several hydration events.

Is the deformation tectonically or reaction induced?

Reaction induced fracturing
Replacement processes associated with a volume change between parent and product induce stresses which lead to fracturing of the mineral that is being replaced (Putnis, 2009). Reaction induced fracturing occur in different geological settings (Jamtveit et al., 2009) including the oceanic lithosphere. Iyer et al. (2008a) studied hierarchical fracturing of orthopyroxene dikes on Leka (see summary in Previous Work section 1.4.2 on page 14). The authors concluded that the changes in density and volume contributed to deformation and fracturing. Plümper et al. (2012b) investigated samples from the Feragen Ultramafic Body and combined the reaction induced fracturing mechanism with interface-coupled dissolution-precipitation(ICDP) mechanism as described by Putnis (2009). Stress was induced by the growth of a product phase generated by ICDP. Two of several important characteristics of ICDP are: 1. Intracrystalline porosity and permeability formed in the product phase facilitate a continuous contact between the fluid and the reaction front. 2. A large change in the solid molar volume, produces a fracture network ahead of the reaction front (Putnis, 2009). An example is shown in Figure 5.2.

Tectonically induced fracturing or the importance of faults
A transform fault is the active part of a strike-slip fault associated with mid-ocean ridges. These fault may have a smaller divergent component or they might be transpressional (Fowler, 2008). This is a setting were profound tectonic deformation occur facilitating fluid pathways.

Thermal fracturing by cooling
The oceanic crust is the most extensive geological formation on Earth with hydrological activity from mid-ocean ridges to beneath subduction-zone accretionary prisms. The flow in ridge flank settings is the volumetrically most important contributor to seawater in the crust and is driven by heat from the cooling lithosphere (Davis and Elderfield, 2004).

Intuitively, one sees that these are continuous processes that are associated with each other across dynamic space and time.

Where did it happen? Serpentinization of Leka Serpentinization is a pervasive process and large masses of water is needed to serpentinize. As mentioned earlier similar deformation zones have been observed in the mantle section at Lauvhatten. Austrheim and Prestvik (2008) reported rodingites on Leka and attributed the formation to fluid-rock interaction associated with ocean floor hydration. Nevertheless, deformation related to regional metamorphism during the Caledonian orogeny and subsequent collaps can not be ruled out.

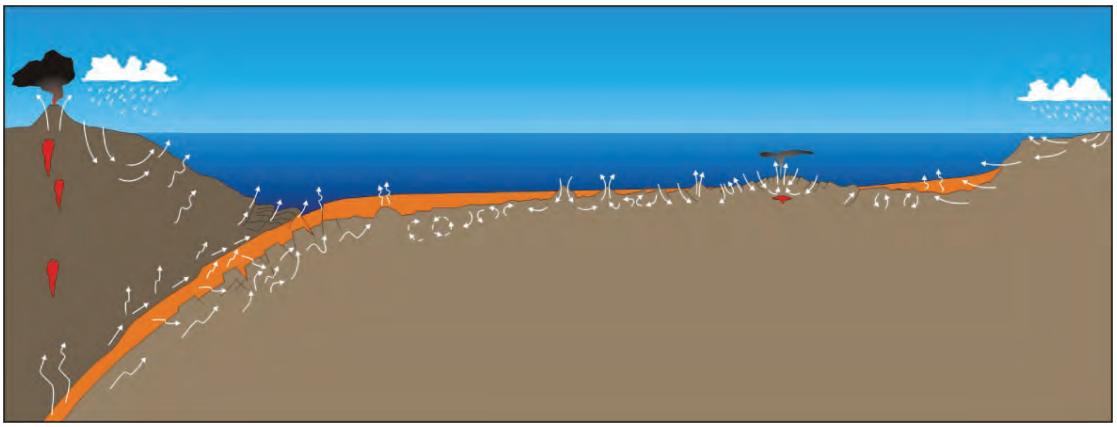

Figure 5.1: Schematic cross-section depicting various types of sub-seafloor fluid flow, ranging from topographically driven flow through continental margins and consolidation-driven flow at subduction zones to thermal buoyancy driven flow at mid-ocean ridge axes and in the oceanic crust beneath broad regions of the oceans. Text and figure from Davis and Elderfield (2004)

Mineral Reactions and Transport of Chemical Components

The rocks at Oksetmyrå are Ca-metasomatized. My studies show that several processes occur simultaneously. Primary minerals are broken down during serpentinization, while secondary phases are formed in equilibrium with serpentine.

One example is fibrous growth of secondary olivine along extensional veins. There are two suggestions as to how these were formed. They may have formed during a dehydration event. Needle-shaped serpentine believed to be the scattered remains of serpentine networks are observed. On the other hand, secondary olivine might have formed in equilibrium with serpentine. A slight increase in Fo content of secondary olivine (Fo93-94) compared to primary olivine (Fo92-93) supports the latter suggestion.

Based on textural relationships in examined samples, five reaction can be outlined where (R1) is Ca-releasing and (R3-R5) are Ca-consuming. Figure 5.2 shows an example of R5 (olivine-clinopyroxene intergrowth). The first three are hydration reactions which may lead to supersaturation of the fluid.

R1: cpx $\rightarrow$ srp

R2: chr $\rightarrow$ chl

R3: cpx1 $\rightarrow$ cpx3

R4: opx (?)$\rightarrow$ cpx + olivine

R5: ol $\rightarrow$ cpx

Why are the same mineral consumed and formed?
Three types of clinopyroxene were identified on a textural basis. Only secondary clinopyroxene(cpx3) was observed from outcrop A, while all phases, primary(cpx1), secondary(cpx2) and fibrous(cpx2), with a dominance of cpx1, were observed at outcrop B. Cpx3 is thought to be formed by the breakdown of cpx1 (R3). H_2O is a controlling factor during serpentinization, thus incomplete reactions may be due to inadequate water accessibility

(Peacock, 1987). As no primary phase was observed in A, it is assumed that the reaction (R3) ran to completion. Conversely, the observation of relict phases at outcrop B indicate that the reaction did not run to completion which might be due to less water available. Alternatively, Bach and Klein (2009), who modeled a titration reation path resembling the fluid-mineral phase at mafic - ultramafic boundary, concluded that large influxes of infiltrating Ca-bearing solutions would result in a depletion of Ca from the system. If the ultramafics at outcrop B experienced large fluxes of water it is still not known if this conclusion is applicable for the ultramafic layered section.

Peacock (1987) reported metamorphic diopside from the Trinity peridotite. The textural and chemical descriptions of this diopside as finer grained, anhedral and without exolution lamellae, and with lower contents of TiO_2, Al_2O_3, Cr_2O_3 and FeO, are in accordance with my observations of cpx3.

Cpx3 often forms in bands parallel to deformation zones and serpentine veins. This localization reflect that these are more hydrated areas compared to the host rock. It is thus reasonable to assume that the deformation zones serve as path ways for element-laden fluids as suggested by Austrheim and Prestvik (2008).

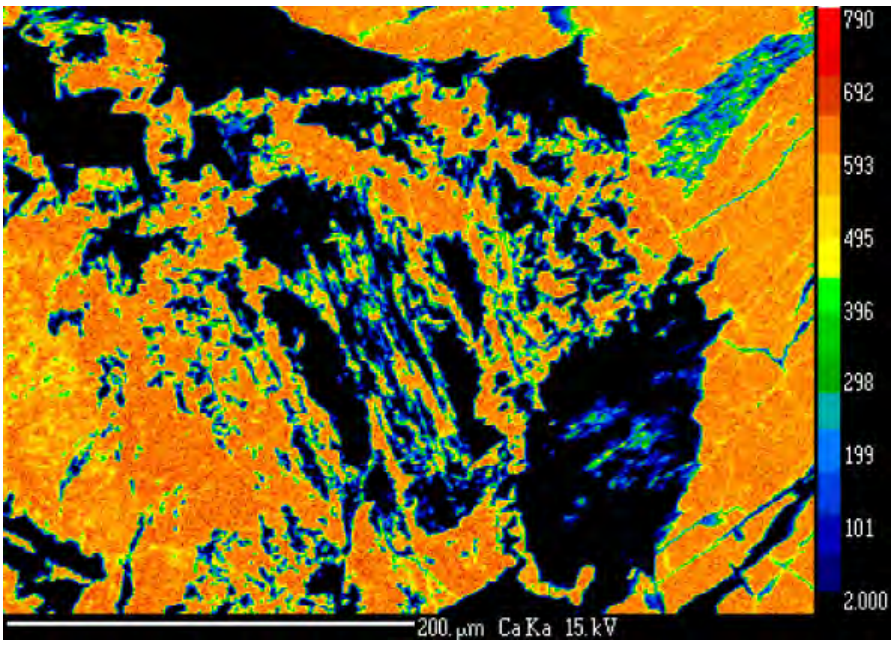

Figure 5.2: The element map for Ca show olivine-clinopyroxene intergrowth. The picture is from the same area as Figure 4.32b (but up side down).

Why is orthopyroxene not found?

No orthopyroxene has been found within the LOC(Austrheim and Prestvik, 2008; Iyer et al., 2008a), inspite of the abundance of ultramafic rocks. (Plümper et al., 2012a) reported cleaved olivine which was interpreted to have replaced orthopyroxene through an intermediate bastite stage. (Austrheim and Prestvik, 2008) reported fibrous clinopyroxene and interpreted this to be a replacement texture after orthopyroxene. Cleaved olivine has not been found in the studied samples from Oksetmyrå, but fibrous intergrowth of olivine and clinopyroxene is common (Figure 5.2) and may represent a former orthopyroxene. Whatever the origin of this aggregate was, the texture suggest severe

mineralogical changes and Ca metasomatism and that little of the primary mineral remains. The distance over which the Ca is transported is unknown. It may represent transport on the grain scale across the lithological boundaries or interaction between seawater and rock.

Brittle-ductile deformation - a function of serpentinization

Small scale fractures with alteration zone (microshear zones) (Figure 2.28 and 4.15) may be an intial stage in a progressive development of a breccia zone. Such a course would start with serpentinization along fractures, the serpentinization fronts would expand into a structure resembling mesh structures, where the serpentinization fronts would surround the clast and detach it from the host rock. This would be a complementary way to produce a breccia zone in addition to the aforementioned.

In the dunite at outcrop B the deformation zones occur predominantly as chaotic breccia and shear zones, often combined, as excellent displayed in Figure 2.26b, with elongated lenses representing ductily deformed fragments from the brecciation process. They appear as extensions of faults, thus their orientations vary accordingly. If these zones really are extensions of faults, then it suggests that the deformation mode changed character from brittle to ductile at the transition between dunite and the other lithologies.

The transition from brittle to ductile in these rocks is assumed to be associated with increased serpentinzation affecting the competence of the individual layers. Petrographical observation from samples of both deformation zones in dunite and the layered sequence, confirmed that the dunites are extensively serpentinized compared to wehrlite and chromite-rich clinopyroxenite. The role of serpentinization in relation to ductile deformation is also strengthened by clinopyroxenite appearing less fragmented compared to the other lithologies (section 2.2.1). The question that arises from this is whether the olivine already was serpentinized and the dunite accordingly reacted ductily, or if the olivine first was deformed as a cataclasite (brittle) which opened the rock for fluid access. As mentioned in the previous paragraph and seen in Figure 2.26b, we observe a cataclasite adjacent to a zone of sheared clasts. The cataclasite is interpreted to be a brittle precursor of ductily deformed clasts. Hence, at least in this case, brittle deformation seems to precede ductile deformation.

Chapter 6

Conclusions

6.1 Conclusions

The results of this study reflect the interaction between serpentinization and deformation in the rocks of the layered ultramafic section at Oksetmyrå, Leka, and can be listed as follows.

- The presented data shows two texturally and chemically different phases of clinopyroxene. The primary phase consists of porphyroclasts, while the secondary phase consists of bands of small grains that precipitated along serpentine veins and high strain zones. The formation of secondary clinopyroxene is a result of Ca-releasing breakdown of primary clinopyroxene during serpentinization.
- Deformation zones acted as conduits for fluids enriched in Ca and enabled the formation of secondary clinopyroxene in other rock volumes.
- The regional foliation is related to serpentinization. Whether the development of the foliation is related to a reaction-induced fracturing process or to a tectonic event can not be established with certainty.
- Serpentinization following hydration took likely place while the Leka Ophiolite Complex still was a part of the oceanic lithosphere.
- Possible serpentinization events during emplacement of the LOC onto Laurentia and/or during later thrusting upon Baltica cannot be ruled out.

Bibliography

H. Austrheim and T. Prestvik. Rodingitization and hydration of the oceanic lithosphere as developed in the leka ophiolite, north-central norway. *Lithos*, 104(104): 177 – 198, 2008. ISSN 0024-4937. doi: 10.1016/j.lithos.2007.12.006. URL `http://www.sciencedirect.com/science/article/pii/S0024493707002964`.

Wolfgang Bach and Gretchen Früh-Green. Alteration of the oceanic lithosphere and implications for seafloor processes. *Elements*, 6(June):173–178, 2010. doi: 10.2113/gselements.6.3.173. URL `http://www.elementsmagazine.org/archives/index.html`.

Wolfgang Bach and Frieder Klein. The petrology of seafloor rodingites: Insights from geochemical reaction path modeling. *Lithos*, 112(1-2):103 – 117, 2009. ISSN 0024-4937. doi: 10.1016/j.lithos.2008.10.022. URL `http://www.sciencedirect.com/science/article/pii/S0024493708002594`. <ce:title>Recent developments on seafloor petrology and tectonics</ce:title> <ce:subtitle>A volume in honour of Roger Hekinian for his life-long contributions to marine petrology and tectonics research</ce:subtitle>.

Wolfgang Bach, Holger Paulick, Carlos J. Garrido, Benoit Ildefonse, William P. Meurer, and Susan E. Humphris. Unraveling the sequence of serpentinization reactions: petrography, mineral chemistry, and petrophysics of serpentinites from mar 15°n (odp leg 209, site 1274). *Geophysical Research Letters*, 33(13), 2006. ISSN 1944-8007. doi: 10.1029/2006GL025681. URL `http://dx.doi.org/10.1029/2006GL025681`.

Calvin G. Barnes, Carol D. Frost, Aaron S. Yoshinobu, Kelsey McArthur, Melanie A. Barnes, Charlotte M. Allen, Øystein Nordgulen, and Tore Prestvik. Timing of sedimentation, metamorphism, and plutonism in the helgeland nappe complex, north-central norwegian caledonides. *Geosphere*, 3(6):683–703, 2007. doi: 10.1130/GES00138.1. URL `http://geosphere.gsapubs.org/content/3/6/683.abstract`.

Stephen J. Barnes. Chromite in komatiites, ii. modification during greenschist to mid-amphibolite facies metamorphism. *Journal of Petrology*, 41(3):387–409, 2000. URL `http://petrology.oxfordjournals.org/content/41/3/387.abstract`.

Charles R. M. Butt and Dominique Cluzel. Nickel laterite ore deposits: Weathered serpentinites. *Elements*, 9(2):123–128, 2013. doi: 10.2113/gselements.9.2.123. URL `http://elements.geoscienceworld.org/content/9/2/123.abstract`.

Earl Davis and Harry Elderfield, editors. *Hydrogeology of the Oceanic Lithosphere*. Cambridge University Press, Cambridge, 2004. URL `www.cambridge.org`.

Yildirim Dilek. Ophiolite concept and its evolution. *Geological Society of America Special*

Papers, 373:1–16, 2003. doi: 10.1130/0-8137-2373-6.1. URL http://specialpapers.gsapubs.org/content/373/1.abstract.

Yildirim Dilek and Harald Furnes. Structure and geochemistry of tethyan ophiolites and their petrogenesis in subduction rollback systems. *Lithos*, 113(1-2):1–20, 2009. ISSN 0024-4937. doi: 10.1016/j.lithos.2009.04.022. URL http://www.sciencedirect.com/science/article/pii/S0024493709001649.

Yildirim Dilek and Harald Furnes. Ophiolite genesis and global tectonics: Geochemical and tectonic fingerprinting of ancient oceanic lithosphere. *Geological Society of America Bulletin*, 123(3-4):387–411, 2011. doi: 10.1130/B30446.1. URL http://gsabulletin.gsapubs.org/content/123/3-4/387.abstract.

Michael A. Dungan. Metastability in serpentine-olivine equilibria. *American Mineralogist*, 62:1018–1029, 1977.

G.R. Dunning and R.B. Pedersen. U/pb ages of ophiolites and arc-related plutons of the norwegian caledonides: implications for the development of iapetus. *Contributions to Mineralogy and Petrology*, 98:13–23, 1988. ISSN 0010-7999. doi: 10.1007/BF00371904. URL http://dx.doi.org/10.1007/BF00371904.

Bernard W. Evans, Keiko Hattori, and Alain Baronnet. Serpentinite: What, why, where? *Elements*, 9(2):99–106, 2013. URL http://elements.geoscienceworld.org/content/9/2/99.abstract.

C.M.R Fowler. *The Solid Earth: An Introduction to Global Geophysics*. Cambridge University Press, Cambridge, UK, second edition, 2008. ISBN 9780521893077.

Gretchen Früh-Green. The lost city 2005 expedition, 2005. URL http://oceanexplorer.noaa.gov/explorations/05lostcity/background/serp/serpentinization.html. [Last updated 10 June 2013].

Gretchen L. Früh-Green, James A.D. Connolly, and Alessio Plas. Serpentinization of oceanic peridotites:implications for geochemical cycles and biological activity. *GEOPHYSICAL MONOGRAPH SERIES*, 144:119–136, 2004. doi: doi:10.1029/144GM08.

H. Furnes, R. B. Pedersen, and C. J. Stillman. The leka opholite complex, central norwegian caledonides: field characteristics and geotectonic significance. *Journal of the Geological Society*, 145(3):401–412, 1988. doi: 10.1144/gsjgs.145.3.0401.

Robin Gill. *Igneous Rocks and Processes: a practical guide*. Wiley-Blackwell, Chichester, West Sussex, UK, first edition, 2010. ISBN 9780632063772. URL http://eu.wiley.com/WileyCDA/WileyTitle/productCd-EHEP002306.html.

Stéphane Guillot and Keiko Hattori. Serpentinites: Essential roles in geodynamics, arc volcanism, sustainable development, and the origin of life. *Elements*, 9(2):95–98, 2013. doi: 10.2113/gselements.9.2.95. URL http://elements.geoscienceworld.org/content/9/2/95.abstract.

Greg Hirth and Stéphane Guillot. Rheology and tectonic significance of serpentinite. *Elements*, 9(2):107–113, 2013. doi: 10.2113/gselements.9.2.107. URL http://elements.geoscienceworld.org/content/9/2/107.abstract.

K. Iyer, H. Austrheim, T. John, and B. Jamtveit. Serpentinization of the oceanic lithosphere and some geochemical consequences: Constraints from the leka ophi-

olite complex, norway. *Chemical Geology*, 249(1-2):66–90, 2008a. ISSN 0009-2541. doi: 10.1016/j.chemgeo.2007.12.005. URL http://www.sciencedirect.com/science/article/pii/S0009254107004937.

K. Iyer, B. Jamtveit, J. Mathiesen, A. Malthe-Sørenssen, and J. Feder. Reaction-assisted hierarchical fracturing during serpentinization. *Earth and Planetary Science Letters*, 267(34):503–516, 2008b. ISSN 0012-821X. doi: 10.1016/j.epsl.2007.11.060. URL http://www.sciencedirect.com/science/article/pii/S0012821X07007996.

Bjørn Jamtveit, ChristineV. Putnis, and Anders Malthe-Sørenssen. Reaction induced fracturing during replacement processes. *Contributions to Mineralogy and Petrology*, 157(1):127–133, 2009. ISSN 0010-7999. doi: 10.1007/s00410-008-0324-y. URL http://dx.doi.org/10.1007/s00410-008-0324-y.

Thomas M. McCollom and Jeffrey S. Seewald. Serpentinites, hydrogen, and life. *Elements*, 9(2):129–134, 2013. doi: 10.2113/gselements.9.2.129. URL http://elements.geoscienceworld.org/content/9/2/129.abstract.

The mineral and locality database Mindat.org, 2013. URL http://www.mindat.org/photo-471844.html. [Last updated 27 February 2013].

E.R Neumann. Two refinements of calculating structural formula for pyroxenes and amphiboles. *Norsk Geol. Tidskrift*, 56:1–6, 1976.

David S. O'Hanley. Solution to the volume problem in serpentinization. *Geology*, 20 (8):705–708, 1992. doi: 10.1130/0091-7613(1992)020<0705:STTVPI>2.3.CO;2. URL http://geology.gsapubs.org/content/20/8/705.abstract.

Cees W. Passchier and Rudolph A. J. Trouw. *Micro-tectonics*. Springer-Verlag Berlin Heidelberg, 2005. ISBN 9783540640035. URL http://www.springer.com/earth+sciences+and+geography/geology/book/978-3-540-64003-5.

SimonM. Peacock. Serpentinization and infiltration metasomatism in the trinity peridotite, klamath province, northern california: implications for subduction zones. *Contributions to Mineralogy and Petrology*, 95(1):55–70, 1987. ISSN 0010-7999. doi: 10.1007/BF00518030. URL http://dx.doi.org/10.1007/BF00518030.

Oliver Plümper, Sandra Piazolo, and Håkon Austrheim. Olivine pseudomorphs after serpentinized orthopyroxene record transient oceanic lithospheric mantle dehydration (leka ophiolite complex, norway). *Journal of Petrology*, 53(9):1943–1968, 2012a. doi: 10.1093/petrology/egs039. URL http://petrology.oxfordjournals.org/content/53/9/1943.abstract.

Oliver Plümper, Anja Røyne, Anna Magrasó, and Bjørn Jamtveit. The interface-scale mechanism of reaction-induced fracturing during serpentinization. *Geology*, 40(12): 1103–1106, 2012b. doi: 10.1130/G33390.1. URL http://geology.gsapubs.org/content/40/12/1103.abstract.

Ian M. Power, Siobhan A. Wilson, and Gregory M. Dipple. Serpentinite carbonation for co2 sequestration. *Elements*, 9(2):115–121, 2013. doi: 10.2113/gselements.9.2.115. URL http://elements.geoscienceworld.org/content/9/2/115.abstract.

Andrew Putnis. Mineral replacement reactions. *Reviews in Mineralogy and Geo-*

chemistry, 70(1):87–124, 2009. doi: 10.2138/rmg.2009.70.3. URL http://rimg.geoscienceworld.org/content/70/1/87.short.

David Roberts. The scandinavian caledonides: event chronology, palaeogeographic settings and likely modern analogues. *Tectonophysics*, 365:283–299, 2003. ISSN 0040-1951. doi: 10.1016/S0040-1951(03)00026-X. URL http://www.sciencedirect.com/science/article/pii/S004019510300026X.

David Roberts and David G. Gee. *An introduction to the structure of the Scandinavian Caledonides*. In Gee, D.G. and Sturt, B.A. (eds) The Caledonide Orogen - Scandinavia and Related Areas. John Wiley and Sons, Chichester, West Sussex, UK, 1985. ISBN 0 471 90821 5.

David Roberts, Øystein Nordgulen, and Victor Melezhik. The uppermost allochthon in the scandinavian caledonides: From a laurentian ancestry through taconian orogeny to scandian crustal growth on baltica. *Geological Society of America Memoirs*, 200: 357–377, 2007. doi: 10.1130/2007.1200(18). URL http://memoirs.gsapubs.org/content/200/357.abstract.

Anja Røyne, Bjørn Jamtveit, Joachim Mathiesen, and Anders Malthe-Sørenssen. Controls on rock weathering rates by reaction-induced hierarchical fracturing. *Earth and Planetary Science Letters*, 275(3-4):364 – 369, 2008. ISSN 0012-821X. doi: 10.1016/j.epsl.2008.08.035. URL http://www.sciencedirect.com/science/article/pii/S0012821X08005797.

M.B. Stephens, M. Gustavson, I.B. Ramberg, and E. Zachrisson. *The Caledonides of central-north Scandinavia - a tectonostratigraphic overview*. In Gee, D.G. and Sturt, B.A. (eds) The Caledonide Orogen - Scandinavia and Related Areas. John Wiley and Sons, Chichester, West Sussex, UK, 1985. ISBN 0 471 90821 5.

B.A. Sturt, A. Thon, and H. Furnes. The karmøy ophiolite, southwest norway. *Geology*, pages 316 – 320, 1979. doi: 10.1130/0091-7613(1979)7. URL http://geology.gsapubs.org/content/7/6/316.full.pdf.

B.A. Sturt, T.B. Andersen, and H. Furnes. *The Skei Group, Leka: an unconformable clastic sequence overlying the Leka Ophiolite*. In Gee, D.G. and Sturt, B.A. (eds) The Caledonide Orogen - Scandinavia and Related Areas. John Wiley and Sons, Chichester, West Sussex, UK, 1985. ISBN 0 471 90821 5.

Kilden til arealinformasjon, 2012. URL http://kilden.skogoglandskap.no/map/kilden/index.jsp?theme=http://kilden.skogoglandskap.no. [Last updated 02 May 2013].

S.J Titus, H Fossen, R.B Pedersen, J.L Vigneresse, and B Tikoff. Pull-apart formation and strike-slip partitioning in an obliquely divergent setting, leka ophiolite, norway. *Tectonophysics*, 354(1-2):101–119, 2002. ISSN 0040-1951. doi: 10.1016/S0040-1951(02)00293-7. URL http://www.sciencedirect.com/science/article/pii/S0040195102002937.

R. Varne and A.V. Brown. The geology and petrology of the adamsfield ultramafic complex, tasmania. *Contributions to Mineralogy and Petrology*, 67(2):195–207, 1978. ISSN 0010-7999. doi: 10.1007/BF01046576. URL http://dx.doi.org/10.1007/BF01046576.

J. D. Winter. *Principles of igneous and metamorphic petrology*. Pearson Education, Limited, 2009. ISBN 9780321681324. URL http://books.google.com/books?id=7y9mQAAACAAJ.

Aaron S. Yoshinobu, Calvin G. Barnes, Øystein Nordgulen, Tore Prestvik, Mark Fanning, and R.B. Pedersen. Ordovician magmatism, deformation, and exhumation in the caledonides of central norway: An orphan of the taconic orogeny? *Geology*, 30(10): 883–886, 2002. doi: 10.1130/0091-7613(2002)030<0883:OMDAEI>2.0.CO;2. URL http://geology.gsapubs.org/content/30/10/883.abstract.